

PRESSURE-INDUCED PHASE TRANSITIONS IN  
SELECT MOLYBDATES AND TUNGSTATES

A THESIS IN  
Physics  
and  
Chemistry

Presented to the Faculty of the University of  
Missouri-Kansas City in partial fulfillment of the  
requirements for the degree

DOCTOR OF PHILOSOPHY

by  
PAUL ROBERT SCOTT JR.

B.S., University of Missouri-Rolla, 2001  
M.S., University of Missouri-Kansas City, 2007

Kansas City, Missouri  
2013

© 2013

PAUL ROBERT SCOTT JR.

ALL RIGHTS RESERVED

PRESSURE-INDUCED PHASE TRANSITIONS IN  
SELECT MOLYBDATES AND TUNGSTATES

Paul Robert Scott Jr., Candidate for the Doctor of Philosophy Degree

University of Missouri-Kansas City, 2013

ABSTRACT

Mao-Bell and symmetric diamond anvil cells were used to study the effect of high-pressure on a series of tungstate and molybdate compounds. The experimental techniques of powder x-ray diffraction and Raman spectroscopy were employed to gain an understanding of the observed phase transitions.

$\text{Bi}_2\text{MoO}_6$  exhibited a phase transition at  $\sim 6.8$  GPa that was observed by a stiffening of its bulk modulus from 51 GPa, for the low-pressure phase, to 141.5 GPa for the high-pressure phase.

$\text{Bi}_2\text{W}_2\text{O}_9$  exhibited a phase transition at  $\sim 11$  GPa that was observed by a change in the x-ray diffraction pattern.

$\text{Bi}_2\text{WO}_6$  exhibited a phase transition between  $\sim 4.8$  GPa and 8.3 GPa that was observed by a stiffening of its bulk modulus from 52.2 GPa, for the low-pressure phase, to 121.8 GPa for the high-pressure phase.

$\text{La}_2\text{Mo}_4\text{O}_{15}$  exhibited two phase transitions one at 2 GPa and another at 17 GPa. The transition at 2 GPa was observed as a change in the x-ray diffraction pattern and has yet to be identified. The transition at 17 GPa was to a glassy, pressure-induced amorphization, state.

$\text{Sm}_2\text{Mo}_4\text{O}_{15}$  exhibited a phase transition at 5.4 GPa. This transition was observed as a change in the x-ray diffraction pattern and has yet to be identified.

$\text{MgNb}_2\text{O}_6$  exhibited a phase transition at 10.3 GPa. This transition was observed in both x-ray diffraction and Raman spectroscopy.

$\text{KNbW}_2\text{O}_9$  exhibited no signs of a phase change up to a pressure of 35 GPa.

The faculty listed below, appointed by the Dean of the College of Arts and Sciences have examined a dissertation titled “Pressure-induced Phase Transitions in Select Molybdates and Tungstates” presented by Paul R. Scott Jr., candidate for the candidate for the Doctor of Philosophy degree, and certify that in their opinion it is worthy of acceptance.

Supervisory Committee

Michael B. Kruger, Ph.D., Committee Chair  
Department of Physics and Astronomy

Jerzy M. Wrobel, Ph.D.  
Department of Physics and Astronomy

David M. Wieliczka, Ph.D.  
Department of Physics and Astronomy

Kathleen V. Kilway, Ph.D.  
Department of Chemistry

James R. Durig, Ph.D.  
Department of Chemistry

## CONTENTS

ABSTRACT .....	ii
LIST OF ILLUSTRATIONS .....	ix
LIST OF TABLES .....	xii
Chapter	
1. INTRODUCTION .....	1
1.1 Overview .....	1
1.2 Motivation and Objectives .....	3
2. HISTORY AND EXPERIMENTAL TECHNIQUES .....	7
2.1 High-Pressure Experiments .....	7
2.1.1 History of High-Pressure Experiments .....	7
2.1.2 The Diamond Anvil Cell .....	7
2.1.3 The Mao-Bell Type Diamond Anvil Cell .....	18
2.1.4 The Symmetric Type Diamond Anvil Cell .....	19
2.2 X-ray Diffraction .....	21
2.2.1 X-ray Diffraction .....	21
2.2.2 Synchrotron X-ray Source .....	26
2.2.3 X-ray Diffraction in the Diamond Anvil Cell.....	28
2.2.4 Rietveld Refinement Analysis of X-ray Diffraction Data .....	31
2.3 Raman Spectroscopy .....	34
2.3.1 Raman Spectroscopy .....	34
2.3.2 Raman Spectroscopy in the Diamond Anvil Cell .....	36

3. DATA AND ANALYSIS .....	38
3.1 Bi <sub>2</sub> MoO <sub>6</sub> .....	38
3.1.1 Abstract .....	38
3.1.2 Introduction .....	38
3.1.3 Material and Methods .....	41
3.1.4 Results and Discussion .....	42
3.1.5 Conclusions .....	54
3.2 Bi <sub>2</sub> W <sub>2</sub> O <sub>9</sub> .....	55
3.2.1 Abstract .....	55
3.2.2 Introduction .....	55
3.2.3 Material and Methods .....	57
3.2.4 Results and Discussion .....	58
3.2.5 Conclusions .....	62
3.3 Bi <sub>2</sub> WO <sub>6</sub> .....	63
3.3.1 Abstract .....	63
3.3.2 Introduction .....	63
3.3.3 Material and Methods .....	65
3.3.4 Results and Discussion .....	66
3.3.5 Conclusions .....	72
3.4 La <sub>2</sub> Mo <sub>4</sub> O <sub>15</sub> .....	73
3.4.1 Abstract .....	73
3.4.2 Introduction .....	73

3.4.3 Material and Methods .....	75
3.4.4 Results and Discussion .....	76
3.4.5 Conclusions .....	81
3.5 Sm <sub>2</sub> Mo <sub>4</sub> O <sub>15</sub> .....	82
3.5.1 Abstract .....	82
3.5.2 Introduction .....	82
3.5.3 Material and Methods .....	84
3.5.4 Results and Discussion .....	86
3.5.5 Conclusions .....	90
3.6 MgNb <sub>2</sub> O <sub>6</sub> .....	91
3.6.1 Abstract .....	91
3.6.2 Introduction .....	91
3.6.3 Material and Methods .....	93
3.6.4 Results and Discussion .....	94
3.6.5 Conclusions .....	102
3.7 KNbW <sub>2</sub> O <sub>9</sub> .....	103
3.7.1 Abstract .....	103
3.7.2 Introduction .....	103
3.7.3 Material and Methods .....	105
3.7.4 Results and Discussion .....	106
3.7.5 Conclusions .....	111

4. CONCLUSION	112
4.1 Conclusion	112
4.2 Future Work	119
APPENDIX	121
REFERENCES	128
VITA	137

## LIST OF ILLUSTRATIONS

Figure	Page
1. Drukker and brilliant cut diamonds .....	10
2. Diamond Anvils .....	12
3. Diamonds in Contact .....	13
4. Jablonski diagram of luminescence .....	15
5. Ruby fluorescence .....	16
6. Mao-Bell diamond anvil cell .....	18
7. Piston Detail .....	19
8. Symmetric DAC .....	20
9. Mao-Bell and symmetric DAC .....	21
10. Diffraction of x-rays in a crystal .....	23
11. Advanced Light Source .....	27
12. X-ray diffraction from a powdered sample .....	29
13. Powdered XRD image .....	30
14. Synchrotron XRD experiment .....	31
15. Raman spectroscopy system .....	37
16. 3D model of $\text{Bi}_2\text{MoO}_6$ .....	40
17. $\text{Bi}_2\text{MoO}_6$ XRD .....	43
18. $\text{Bi}_2\text{MoO}_6$ V vs P .....	49
19. $\text{Bi}_2\text{MoO}_6$ normalized unit cell parameters .....	51
20. $\text{Bi}_2\text{MoO}_6$ microstrain vs pressure .....	53

21. 3D model of $\text{Bi}_2\text{W}_2\text{O}_9$	57
22. $\text{Bi}_2\text{W}_2\text{O}_9$ XRD	59
23. $\text{Bi}_2\text{W}_2\text{O}_9$ V vs P	61
24. 3D model of $\text{Bi}_2\text{WO}_6$	65
25. $\text{Bi}_2\text{WO}_6$ XRD	67
26. $\text{Bi}_2\text{WO}_6$ V vs P	69
27. $\text{Bi}_2\text{WO}_6$ normalized unit cell parameters	71
28. 3D model of $\text{La}_2\text{Mo}_4\text{O}_{15}$	74
29. $\text{La}_2\text{Mo}_4\text{O}_{15}$ XRD	78
30. $\text{La}_2\text{Mo}_4\text{O}_{15}$ V vs P	80
31. 3D model of $\text{Sm}_2\text{Mo}_4\text{O}_{15}$	84
32. $\text{Sm}_2\text{Mo}_4\text{O}_{15}$ XRD	87
33. $\text{Sm}_2\text{Mo}_4\text{O}_{15}$ V vs P	89
34. 3D model of $\text{MgNb}_2\text{O}_6$	92
35. $\text{MgNb}_2\text{O}_6$ bench top XRD	95
36. $\text{MgNb}_2\text{O}_6$ XRD	97
37. $\text{MgNb}_2\text{O}_6$ V vs P	99
38. Raman shift of $\text{MgNb}_2\text{O}_6$	101
39. 3D model of $\text{KNbW}_2\text{O}_9$	104
40. $\text{KNbW}_2\text{O}_9$ XRD	107
41. 2D plot of calculated and experimental data for $\text{KNbW}_2\text{O}_9$	108
42. $\text{KNbW}_2\text{O}_9$ V vs P	110

43. Material versus atmospheric unit cell volume	.....	116
44. Material versus bulk modulus	.....	117
45. Material versus phase change pressure	.....	118

## LIST OF TABLES

Table	Page
1. Atomic coordinates and temperature factors for $\text{Bi}_2\text{MoO}_6$ .....	42
2. Atomic coordinates and temperature factors for $\text{Bi}_2\text{W}_2\text{O}_9$ .....	58
3. Atomic coordinates and temperature factors for $\text{Bi}_2\text{WO}_6$ .....	66
4. Atomic coordinates and temperature factors for $\text{La}_2\text{Mo}_4\text{O}_{15}$ .....	76
5. Atomic coordinates and temperature factors for $\text{Sm}_2\text{Mo}_4\text{O}_{15}$ .....	85
6. Atomic coordinates and temperature factors for $\text{MgNb}_2\text{O}_6$ .....	94
7. Atomic coordinates and temperature factors for $\text{KNbW}_2\text{O}_9$ .....	105
8. Summary of the data analysis .....	119

## CHAPTER 1

### INTRODUCTION

#### 1.1 Overview

High-pressure experimental physics grants scientists a powerful method for observing the effects of extreme conditions upon materials. The application of pressure can have profound consequences on the structure and properties of materials and, as such, produce a myriad of interesting areas to study. In particular the following are often considered the highest priority:

- A) Physical phase transitions: These are the phase transitions that are readily observed in everyday life. They cover the transitions from plasma to gas to liquid to solid. The application of pressure is often used to find precise physical phase transition points. The equation of state of water is a great example of this.
- B) Structural phase transitions: Structural phase transitions are a bit more complicated than physical ones and are the focus of the proceeding work. These changes cover the area of transforming the crystal structure of materials. Often, the materials convert to structures of lower symmetry such as transitioning from cubic to monoclinic.
- C) Electronic phase transitions: Pressure can even induce electronic phase transitions. Such changes are readily observed in some materials by simply observing their color.

- D) Mechanical and thermal properties: Mechanical properties encompass a large amount of macro- and microscopic characteristics. Macroscopic properties include bulk modulus, shear modulus, Young's modulus, and yield strength. An example of a microscopic property would be unit cell volume. Some of the thermal properties are heat capacity, thermal expansion, and melting point.
- E) Materials synthesis: Pressure can be used to create novel materials that remain stable in an atmospheric environment. The creation of diamond using high-pressure and high-temperature is just one example of this. Cubic boron nitride is another example of a very useful material generated from the field of high-pressure physics.

Static high-pressure experimental physics is most often performed using a simple, yet effective, apparatus known as a diamond anvil cell (DAC). This system combined with various spectroscopic techniques allow for easy access to further understanding the nature of materials in our universe. Knowing the effects of pressure and having the tools to observe them scientists can implement high-pressure research in many fields. Such as:

- A) Geosciences
- B) Materials synthesis
- C) Fundamental research

## 1.2 Motivation and Objectives

The purpose of this study is to observe the behavior of a series of molybdates and tungstates under the application of high-pressure. Mao-Bell and symmetric type diamond anvil cells combined with x-ray diffraction and Raman spectroscopy were used to probe the samples.

Molybdates and tungstates are an interesting class of materials that exhibit an array of functional properties. Often these properties can be advantageously changed, or engineered, under varying conditions. The use of high-pressure experimental techniques allows for an in-depth look into the subtle lattice changes that contribute to these changes in properties. Observations of the lattice instabilities could help develop a better physical understanding of the fundamental physics behind several important material properties such as ferroelectricity, piezoelectricity, negative thermal expansion, pressure-induced amorphization.

The work presented here focuses on using high-pressure to induce changes within the structure of a select few of these materials as well as a niobate compound. Under study are  $\text{Bi}_2\text{MoO}_6$ ,  $\text{Bi}_2\text{W}_2\text{O}_9$ ,  $\text{Bi}_2\text{WO}_6$ ,  $\text{La}_2\text{Mo}_4\text{O}_{15}$ ,  $\text{Sm}_2\text{Mo}_4\text{O}_{15}$ ,  $\text{MgNb}_2\text{O}_6$ , and  $\text{KNbW}_2\text{O}_9$ .

$\text{Bi}_2\text{WO}_6$ ,  $\text{Bi}_2\text{MoO}_6$  and  $\text{Bi}_2\text{W}_2\text{O}_9$  belong to a large group of ferroelectric bismuth-layered compounds, known as the Aurivillius family, which have properties for potential device applications.  $\text{Bi}_2\text{W}_2\text{O}_9$  has been observed to be a photocatalytic material for  $\text{H}_2$  and  $\text{O}_2$  as well as being useful in the photodegradation of organic compounds<sup>1-3</sup>. It has also found to be a promising material for microwave applications<sup>4</sup>.  $\text{Bi}_2\text{WO}_6$  is a well-

known ferroelectric and piezoelectric material with a high Curie temperature and the largest spontaneous polarization among bismuth layered ferroelectrics <sup>5, 6</sup>. Among other applications,  $\text{Bi}_2\text{WO}_6$  has been used for fabrication of hetero-structures and thin films with excellent photocatalytic performance <sup>7, 8</sup>, positive electrodes in rechargeable lithium batteries <sup>9</sup>, and humidity sensors <sup>10</sup>.  $\text{Bi}_2\text{MoO}_6$  thin films are used as humidity sensors <sup>10</sup> and they also exhibit photoelectrochemical properties <sup>11</sup>.

Polar hexagonal tungsten-bronze type oxides such as  $\text{KNbW}_2\text{O}_9$ ,  $\text{RbNbW}_2\text{O}_9$  and  $\text{KTaW}_2\text{O}_9$  are of interest due to their second-harmonic generation, piezoelectric, pyroelectric, and ferroelectric properties <sup>12</sup>.

Negative thermal expansion properties have been reported for  $\text{Dy}_2\text{Mo}_4\text{O}_{15}$  and  $\text{Y}_2\text{Mo}_4\text{O}_{15}$  molybdates <sup>13</sup>. Negative thermal expansion is interesting for commercial applications since it has promise for use in tailoring thermal expansion characteristics. In particular, materials with zero thermal expansion are highly desired for optical devices <sup>14</sup>.

Other materials in these groups, but not studied in this work, are:

A)  $\text{AB}(\text{XO}_4)_2$  molybdates and tungstates are interesting because they can be used in applications such as Cherenkov radiation for electromagnetic calorimeters, scintillators, Raman shifters and materials for tunable and short-pulse laser operation <sup>15-20</sup>.  $\text{KFe}(\text{MoO}_4)_2$  exhibits very interesting magnetic properties <sup>21</sup> whereas  $\text{RbFe}(\text{MoO}_4)_2$  has recently been found to be a unique and rare multiferroic material, in which the ferroelectric order is induced by chiral magnetic ordering <sup>22</sup>.

B)  $B_2(XO_4)_3$  molybdates and tungstates have been investigated due to their optical, ferroelastic, ferroelectric and negative thermal expansion properties<sup>23-</sup>

28.

C) Recently, it has also been shown that  $Al_2(WO_4)_3$  can be used for fabrication of an ion-selective electrode for Fe(III) determination in rocks, pharmaceuticals and water<sup>29</sup>.

High-pressure experiments are well known to be a precise probe for investigating subtle changes in a material. This is partially due to the fact that, unlike temperature experiments, high-pressure only acts upon interatomic distances. Temperature experiments also act upon phonon interactions. Therefore, studying molybdates and tungstates that exhibit subtle changes in the lattice structure is of great interest to high-pressure physics. Observation of lattice instabilities can help with developing a better understanding of ferroelectric order and ferroelectric-magnetic instabilities.

Raman studies under high-pressure conditions are also useful for understanding the origin of negative thermal properties since these properties are often attributed to low energy rigid unit modes or transverse anharmonic vibrations of the twofold coordinated oxygen atoms<sup>30</sup>. However, the work presented here focuses on the use of x-ray diffraction and then compares and contrasts to previous Raman studies<sup>31-35</sup>.

The particular molybdates and tungstates in this work have been selected for review because they are technologically important materials with respect to their optical, ferroelectric and negative thermal expansion properties. It is therefore of great importance to study the fundamental physical properties of these materials when

subjected to high-pressure conditions. Particularly, high-pressure experimentation allows for an in-depth review of subtle lattice instabilities that could lead to a better understating of the fundamental nature of pressure-induced phenomena.

## CHAPTER 2

### HISTORY AND EXPERIMENTAL TECHNIQUES

#### 2.1 High-Pressure Experiments

##### 2.1.1 History of High-Pressure Experiments

In the early twentieth century Percy Bridgman developed an apparatus that allowed the generation of pressure in excess of 10 GPa. This is to be considered the birth of modern high-pressure experimental physics and, as such, he was awarded the Nobel Prize in 1946. Much work has been performed since to improve upon his original work but most significant was in the late 1950's. This is when the advent of the gasketed diamond anvil cell occurred. It was created by Weir, Velkenburg, Lippincott and Bunting at NBS Laboratories <sup>36</sup>. The diamond anvil cell eventually led the way for high-pressure studies in almost any laboratory setting but it was not until 1972 that it became widely accepted in the scientific community. This acceptance was due to the development of a convenient and precise method for measuring pressure, ruby fluorescence <sup>37</sup>.

##### 2.1.2 The Diamond Anvil Cell

The diamond anvil cell is a device used in experiments that allows for the creation of static high-pressures (~300 GPa has been achieved). In its simplest form a diamond anvil cell consists of two opposing diamonds with a sample placed between the culets combined with some method to apply force to the diamonds. There many methods for

applying force in order to generate pressure and two of the most common methods will be discussed in this section.

Diamond, being the hardest substance known, is the key ingredient to the generation of ultra-high pressures. It is relatively transparent to electromagnetic radiation over a very wide range (roughly infrared to hard x-rays with the exception of a few regions in the ultra-violet)<sup>38</sup>. This transparency proves highly useful in a broad range of spectroscopic techniques since the diamonds themselves do not interfere with the incoming radiation that is being used to study the materials subjected to high-pressure.

Generally, diamonds are classified into two main categories, Type I and Type II<sup>39, 40</sup>. The level of impurities in the diamond lattice determines the type. Those with significant nitrogen impurity are classified as Type I and are, in general, a bit less useful in high-pressure experiments due to their ability to absorb more electromagnetic radiation. Type I diamonds can also be separated into two groups, Group A and Group B. The group classification depends on how the nitrogen impurities are aggregated. Group A has nitrogen atoms in pairs and Group B has nitrogen in large evenly spaced aggregates. Group A has sharp absorption bands in a few regions whereas Group B has broad absorption bands in the blue and green regions. A diamond with platelet nitrogen impurities can actually be more useful in the laboratory due to its resistance to plastic deformation thus causing it to be able to withstand higher pressures. Type II diamonds do not contain a high level of nitrogen impurities and therefore remain mostly transparent in the ultraviolet and infrared regions, which are often used in laboratory spectroscopic

methods. The main downside to Type II diamonds is that they are more expensive than Type I.

Beyond the type of diamond and its impurities the shape and cut of the diamond is very important. Due to their ready availability the brilliant cut diamond from the jewelry industry is often the most common cut used. The brilliant cut is modified to have a flat surface at the tip, the culet, which is highly polished and parallel to the top, or table, surface. While this is an excellent cut for jewelry since it maximizes internal reflections giving a diamond more brilliance it is not the highest strength setup for achieving ultra-high pressure. The fairly newly developed Drukker cut diamond is preferred for maximizing the safety of attainment of high-pressure (safety being for that of the diamonds themselves)<sup>39</sup>. The Drukker cut has an enlarged table, compared to the brilliant cut, and also increases the angle to the culet. A comparison of the Drukker and brilliant cut can be seen in Figure 1. Also in the brilliant cut there is a thin shoulder that develops high stresses. This has been removed in the Drukker cut to decrease the chance of chipping or complete diamond destruction. A further modification to any cut of diamond is the addition of a beveled edge at the culet. This change reduces the stresses at the edge of culet thus lowering the chance of the diamonds pressing through the gasket material and causing catastrophic failure.

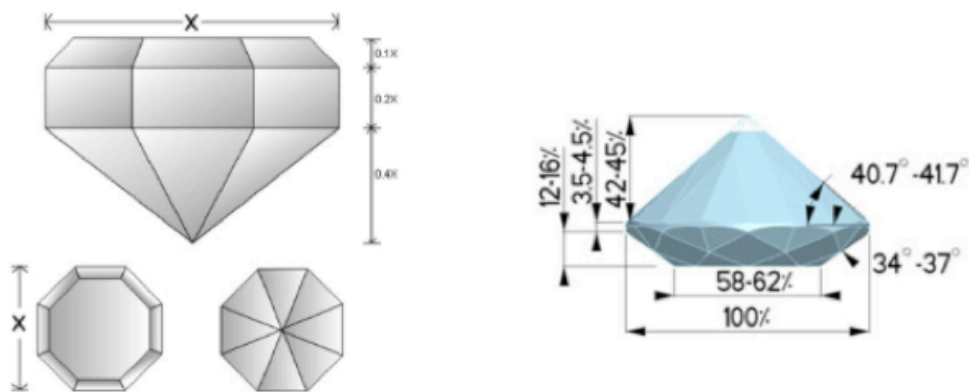


Figure 1. Drukker and brilliant cut diamonds. (Left) Schematic of a Drukker cut diamond (Right) Schematic of a brilliant cut diamond [images courtesy of diamondanvils.com]

The diamond mounting surfaces, or seats, need to be flat with holes at the center for spectroscopic access. The material that the seats are made from is of high importance as its strength is a determining factor of how high of a pressure the experiment can achieve. The access holes behind the diamonds should generally not have a diameter greater than about one third that of the table and should be cut at an angle wide enough to allow for scattered light not to be absorbed. The mounting surfaces should be machined flat and then polished and before the diamond is mounted a layer of thin zirconium foil should be placed between the diamond and the mounting surface. The diamonds need to be secured to the seats such that the diamonds do not move laterally especially during alignment, loading, or cleaning. The lateral stresses are low so an epoxy resin such as J. B. Weld is usually sufficient.

Maintaining the alignment of the diamond anvils with one another is crucial to both diamond safety and maximum achievable pressure. Alignment is verified through an optical microscope, typically a stereomicroscope. The diamonds are gently pushed to near contact positions and then the rough lateral alignment and parallelism are checked. Depending on the type of DAC the available axis of alignment will vary. Once the rough alignment is completed the diamonds are very carefully pushed into contact. The removal of particles or liquids from culet is absolutely necessary before doing this. Fine adjustment of the X-Y translation is made by observing the diamonds from the side, see Figure 2. For parallelism and angular alignment, the alignment is viewed through the diamonds. Although not completely necessary, it is good practice to have the rotation of the, typically octagonal, culets match. Parallelism is much more important with regards to the maximum pressure the experiment may reach. Verification of parallelism is made by observing the interference fringes made when the culets are in contact, see Figure 3. The higher the number of fringes the worse the parallelism is. When proper parallelism is reached,  $\sim 0.1^\circ$ , only two fringes should remain. Further refinement of the parallelism will lead to the fringes becoming absent and only a homogenous grey color will be present.

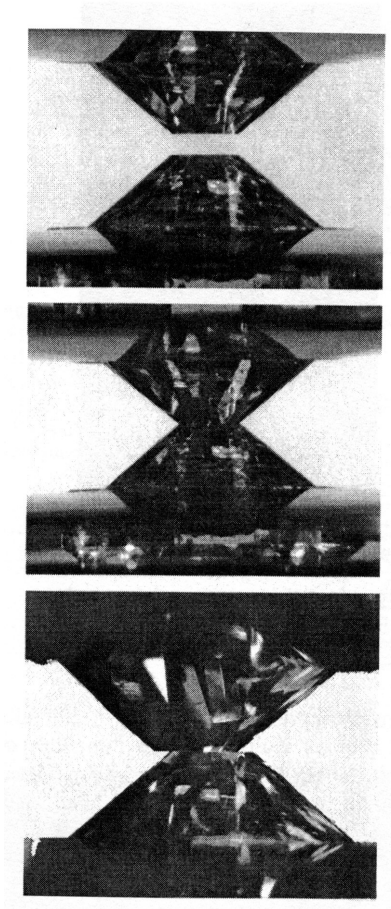


Figure 2. Diamond Anvils. (Top) A side view of the diamond anvils before they are pushed together (Middle) Diamond anvils in contact with decent alignment (Bottom) Diamond anvils in contact with poor lateral alignment <sup>41</sup>.

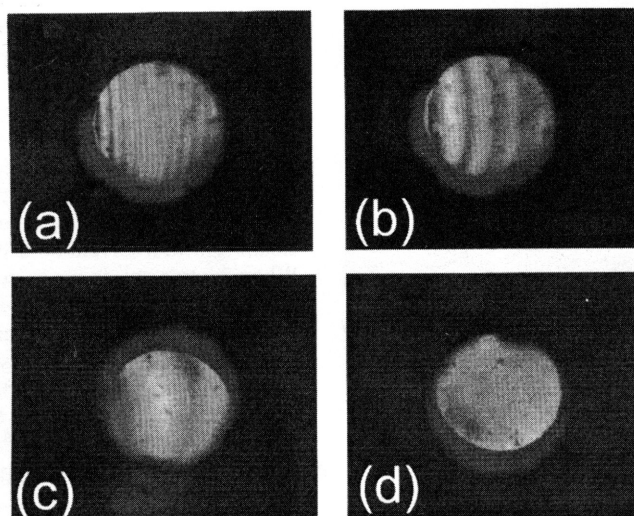


Figure 3. Diamonds in Contact. (a) Diamond anvils in contact with a large number of interference fringes (b) less fringes (c) only two fringes remain (d) anvils in very good alignment with no fringes, only a homogenous grey remains

The ability to contain a sample between the opposing diamonds is an absolute necessity to achieving a high-pressure experiment. The easiest and most common way to do this is with a metal gasket. The gasket provides support to the culet edges while providing the opportunity to create a pressure chamber near the center of the culets. The thickness and type of material the gasket is made from is important in creating the pressure distribution on the anvil and therefore within the volume of the sample chamber and upon the sample itself. Most often a gasket made of spring steel is used. The gasket is placed between the two anvils with a starting thickness of  $\sim 250 \mu\text{m}$  is pre-indented to a thickness of  $\sim 50 \mu\text{m}$ . The initial thickness of the pre-indentation is chosen to be approximately twice that of the final thickness at the highest pressure that the experiment

will reach. This is done in order to provide the maximum hydrostatic pressure to the sample while maintaining a stable gasket hole. After the gasket is pre-indented either electro discharge machining or laser drilling is used to drill a hole in the center of the pre-indented area. The proper hole diameter is approximately  $1/3^{\text{rd}}$  the diameter of the diamond culets. This ratio gives the best compromise between maximizing the sample chamber volume and gasket stability at high-pressure. The amount of sample loaded into the chamber needs to be as small as possible since the sample must not bridge the gap between the two diamond anvils during the experiment. Typically  $1/20^{\text{th}}$  to  $1/10^{\text{th}}$  of the total chamber volume can be filled with the sample under study.

In order to provide hydrostatic conditions inside the sample chamber a pressure-transmitting medium must be inserted into the chamber along with the sample. The most commonly used media is a 4:1 mixture of methanol and ethanol. This mixture is believed to be quasi-hydrostatic until it turns into a glass at  $\sim 10.4$  GPa<sup>42</sup>. More recently a mixture of methanol, ethanol, and water at the ratio of 16:3:1 has been used since it maintains hydrostaticity until  $\sim 14.5$  GPa<sup>43</sup>. Other materials such as rare gases can be used to achieve hydrostatic conditions at higher pressures but they are difficult to load at a reasonable density<sup>44-46</sup>.

Finally, some type of calibration standard must be used in order to know the pressure within the diamond anvil cell. The most common technique is that of ruby fluorescence<sup>47-49</sup>. A small amount of ruby is loaded within the sample chamber and illuminated with a laser. The resulting fluorescence is measured with a spectrometer. Fluorescence, being a form of luminescence, is the emission of photons from excited

electrons. Fluorescence is the emission that results from an electron returning to a lower orbital from an excited state. A diagram of this can be seen in Figure 4.

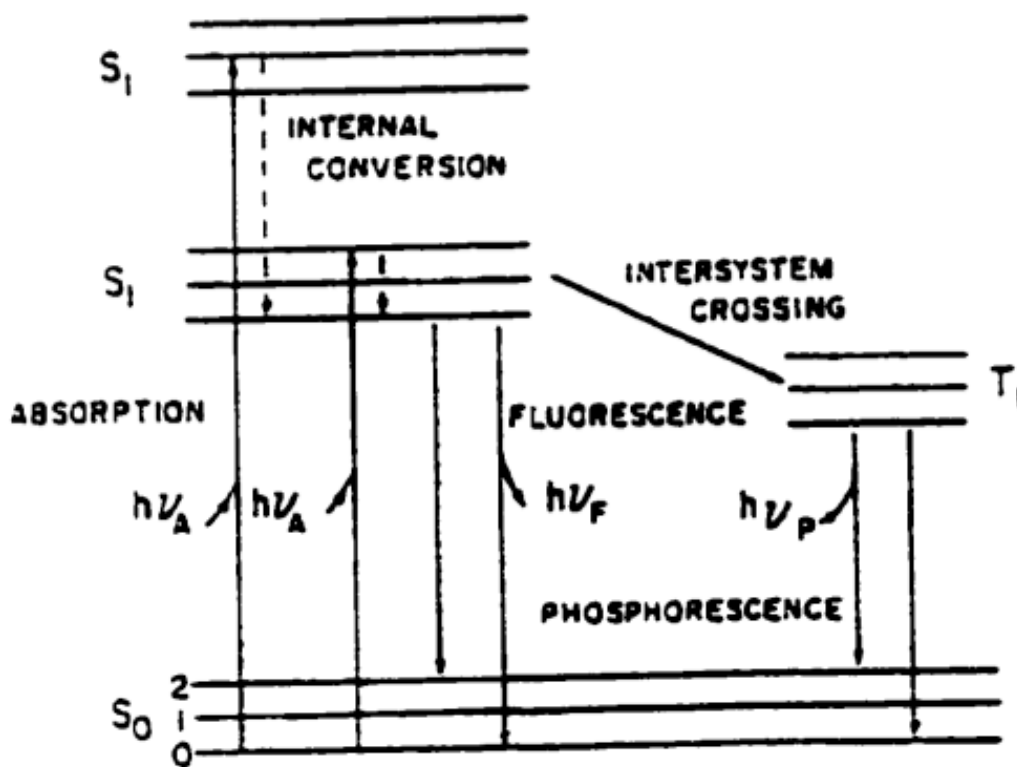


Figure 4. Jablonski diagram of luminescence<sup>50</sup>.

The wavelength of ruby fluorescence is a function of pressure and has been previously calibrated<sup>37, 51-55</sup>. The shift in frequency of the sharp “R” fluorescence line, generally the “R1” line is the only one necessary, is measured and the empirical formula is:

$$P = 380.8 * ((\lambda_p / \lambda_0)^5 - 1) \quad (2.1.2.1)$$

where  $\lambda_p$  and  $\lambda_0$  are the wavelength of the R1 line at pressure and at 1 bar respectively. A plot of ruby fluorescence can be seen in Figure 5. The main disadvantages to this technique are (1) poor performance in non-hydrostatic conditions and (2) the need of an external laser source during an x-ray diffraction experiment that causes the need for the removal of the diamond anvil cell from the x-ray experiment.

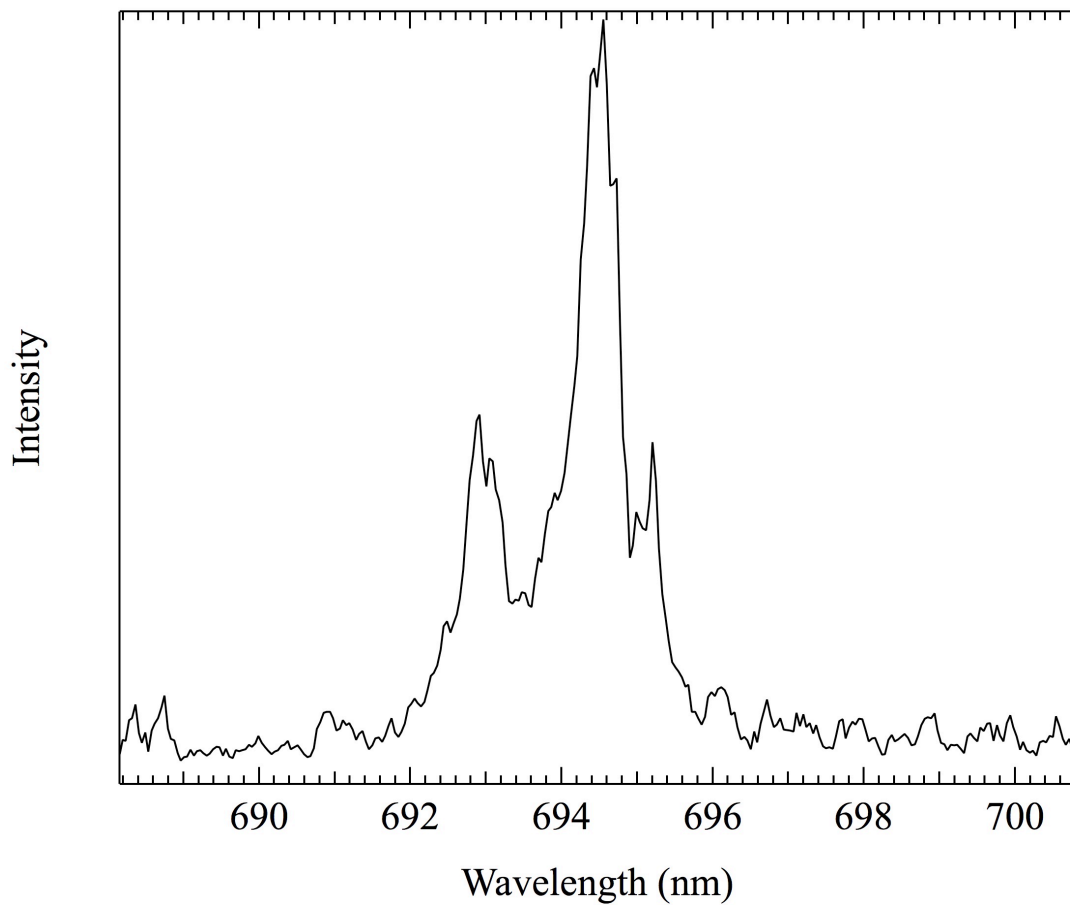


Figure 5. Ruby fluorescence.

Another pressure calibrant that can be used during x-ray diffraction experiments is gold. Gold has a very simple cubic structure and its unit cell volume has been studied under high pressure <sup>56, 57</sup>. Therefore the unit cell volume of gold, which can easily be measured during a diffraction experiment, can be used as a pressure calibrant. The following equations are used to calculate pressure due to a gold marker:

$$P = \frac{3}{2}K * X(1 + \frac{3}{4}(4 - K')X) * (1 + X)^{5/2} \quad (2.1.2.2)$$

Where K is the bulk modulus of gold, 166.65 GPa, K' is the pressure derivative of the bulk modulus of gold, 5.4833, and X is defined as:

$$(a^3 / V_0)^{2/3} - 1 \quad (2.1.2.3)$$

Where 'a' is the experimental value of the unit cell parameter of gold and V<sub>0</sub> is the ambient unit cell volume of gold, 67.832 Å<sup>3</sup> <sup>57</sup>. The main disadvantage of using gold is that it relies on the experimental setup itself and any error in that setup can propagate directly into data analysis of the sample. Whereas the ruby fluorescence method relies on a completely different set of physics and a different experimental technique than x-ray diffraction so the chance for error is much lower.

### 2.1.3 The Mao-Bell Type Diamond Anvil Cell

The Mao-Bell diamond anvil cell, Figure 6, is modeled after the design of Piermarini and Block<sup>51</sup>. The main body of the DAC is a rectangular plate of strong steel, usually either 4340 Vascomax or 300 steel. The plate has an opening to support the piston-cylinder. Force is applied with a bolt and Bellville washers through a lever arm in contact with the piston. Within the piston-cylinder arrangement are half-cylinders that the diamonds are mounted upon. A detail of this arrangement can be seen in Figure 7. The half-cylinders allow for precise alignment of the anvils by both tilt and translation. The half-cylinder seats, as well as the piston-cylinder itself, have access holes such that the incident radiation used for spectroscopy can illuminate the sample.

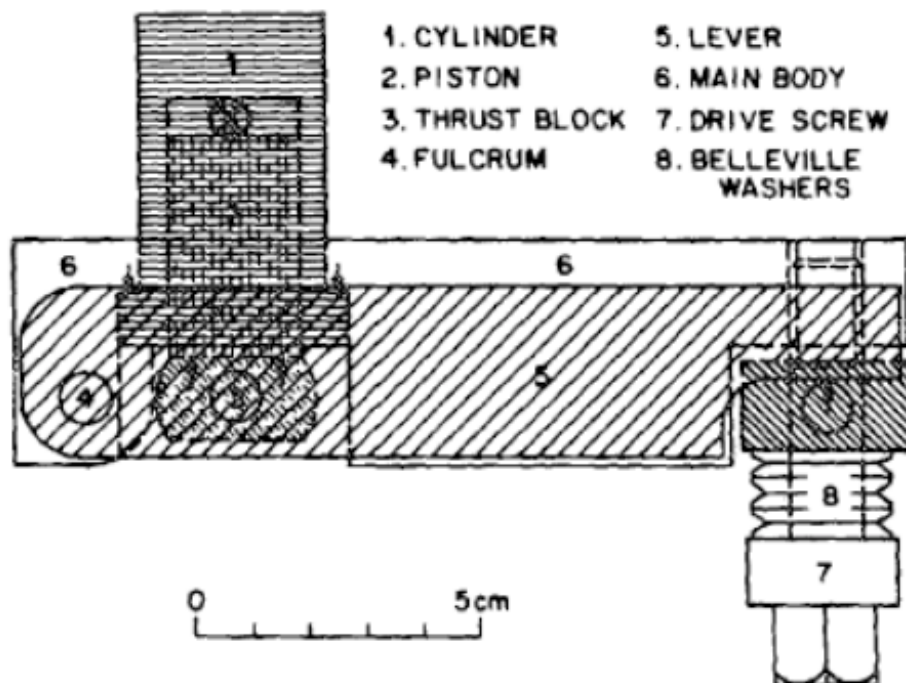


Figure 6. Mao-Bell diamond anvil cell<sup>58</sup>.

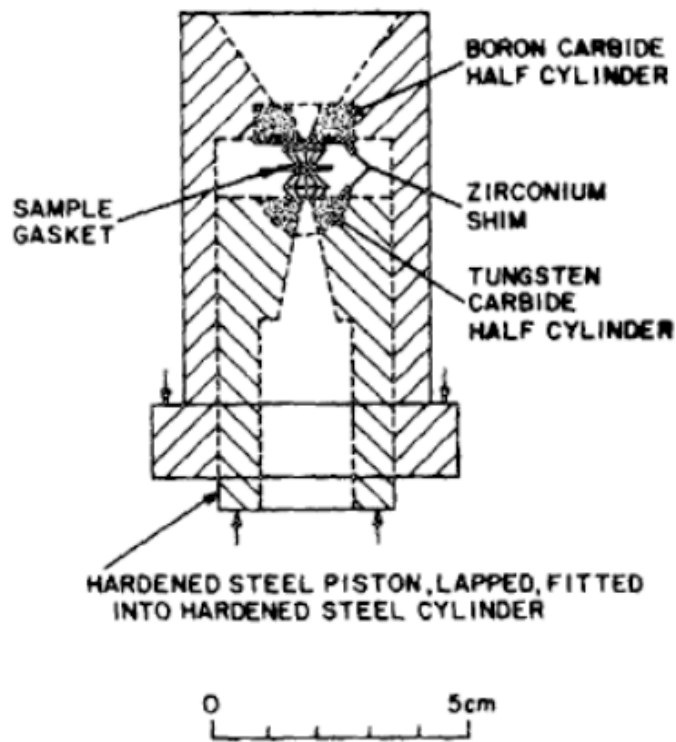


Figure 7. Piston detail. Detail of the piston-cylinder within the Mao-Bell diamond anvil cell<sup>58</sup>.

#### 2.1.4 The Symmetric Type Diamond Anvil Cell

In an attempt to reduce the overall size and weight of a diamond anvil cell the symmetric type cell was created, Figure 8. The cells are typically ~2" in diameter and ~1.5" tall. The most readily used version of this is the Mao-type symmetric cell that relies on a piston-cylinder arrangement with four bolts providing the applied force. The use of oppositely threaded bolts allows for ease of use and, more importantly, it eliminates torque upon the cell, therefore increasing stability. The symmetric cell can provide 20 – 30 GPa of pressure when diamond alignment is precise. One downside to this compact

arrangement is that the number of axis available for diamond alignment is reduced by one, the axis of parallelism. As with the standard Mao-Bell DAC the openings at either end are cut at an angle in order to maximize the amount diffracted light emanating from the sample. A side-by-side photo of a Mao-Bell and a symmetric diamond anvil cell can be seen in Figure 9.

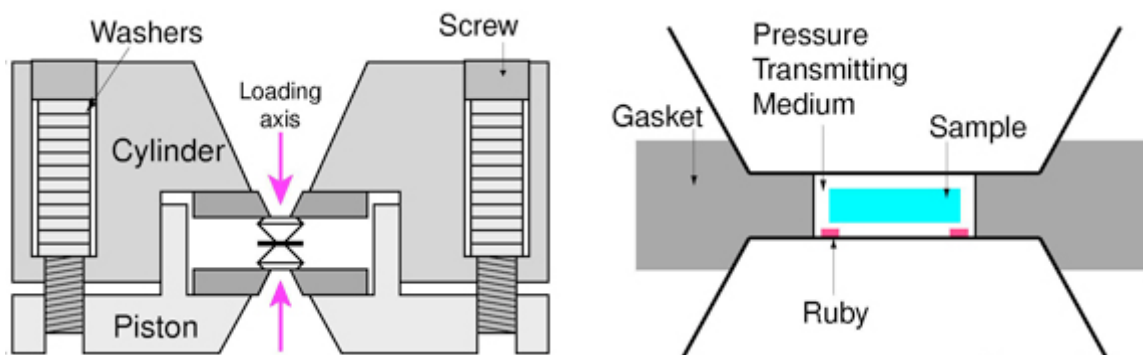


Figure 8. Symmetric DAC (Left) Side view of the entire cell (Right) Close up of the diamond to gasket interface and the sample chamber<sup>59</sup>.

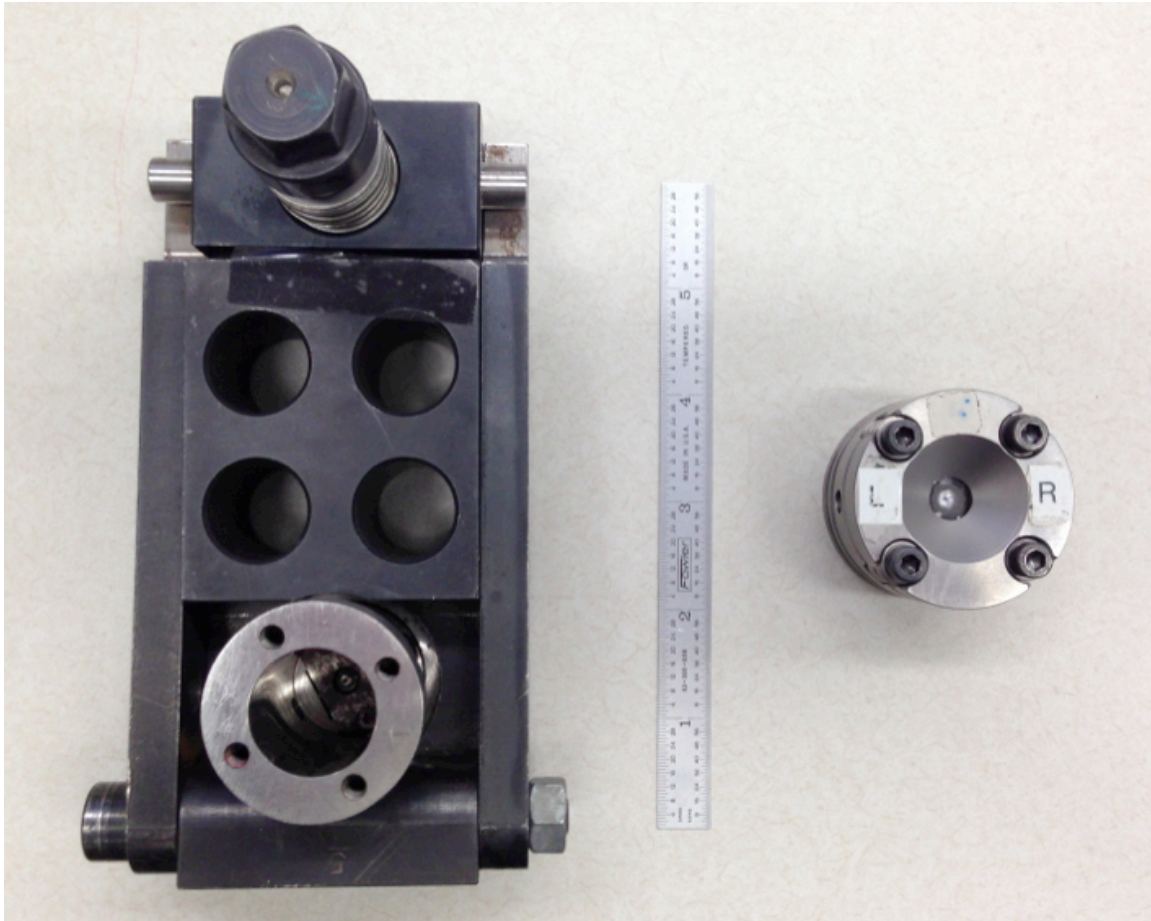


Figure 9. Mao-Bell and symmetric DAC (Left) Mao-Bell DAC (Right) Symmetric DAC.

## 2.2 X-ray Diffraction

### 2.2.1 X-ray Diffraction

The diffraction of x-rays begins with the physical property of scattering. One of the better references for x-ray diffraction and its many uses is that of B. D. Cullity<sup>60</sup>. When an x-ray beam interacts with an atom in a material it is scattered in all directions. In crystalline materials atoms are arranged periodically. This periodic nature leads to both

constructive and destructive interference of the scattered beams. Thus, particular arrangements, separations etc. will lead to strong constructive interference in very particular directions. These diffracted beams are of high intensity relative to the background but only on the order of a fraction of a percent of the intensity of the incident beam. Even so, they can be easily detected by equipment given that the incident beam is of sufficient intensity.

One of the keys to performing an angular dispersive x-ray diffraction experiment is the use of a monochromatic x-ray source. The use of a single energy of light allows for a single set of diffracted beams and therefore analysis of the properties of the atomic lattice can easily be calculated. Figure 10 is the representation of a periodic, crystalline, array of atoms. A monochromatic incident x-ray is shown as the numbers 1, 2, 3, and 4. This beam is incident upon the material plane at an angle  $\theta$  and, when it interacts with an atom, is scattered. The nature of constructive interference can be observed by looking at the path lengths and interactions between rays 1 and 3 with atoms A and C. These path lengths of 1 to 1' and 3 to 3' are not equal and their difference is equal to  $2d \sin(\theta)$ . This is also the same difference as the overlapping rays 1' and 4' from incident rays 1 and 4. When this path length difference is precisely an integer multiple of the wavelength of incident light, such that the peaks and valleys of the scattered electromagnetic waves are in phase, then the rays are completely constructive. Thus we obtain Bragg's formula:

$$n\lambda = 2d \sin(\theta) \quad (2.2.1.1)$$

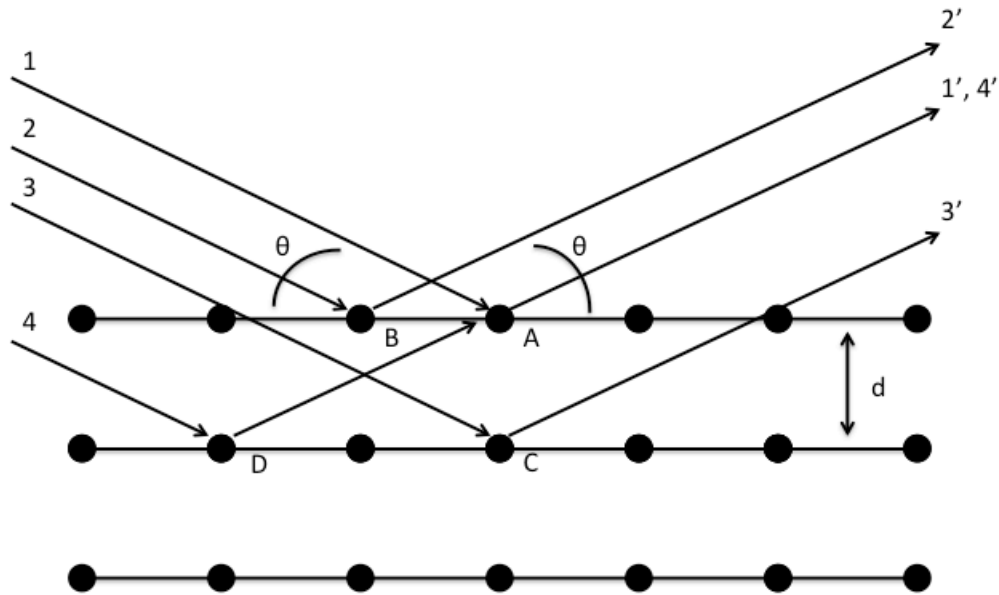


Figure 10. Diffraction of x-rays in a crystal.

From equation 2.2.1.1 we can see that when an experiment is set up such that the wavelength of the x-ray is known and the scattering angle,  $\theta$ , is measured then the distance between atomic planes,  $d$ , can be calculated.

Several factors can influence the intensity and position of the diffracted beams. Of them the following are of most importance: microstrain, electron scattering, structure factor, multiplicity factor, Lorentz factor, absorption factor, and temperature factor.

Microstrain occurs in two forms such that it causes the observed diffracted peaks to either shift in location or to be broadened. A shift in the peaks is due to uniform strain in a material. Uniform strain causes a change in the plane spacings but since it is uniform over the entire sample they all move. For example all of the 100,  $hkl$ , planes in all of the crystals in a sample are changed equally. A non-uniform strain, such as a plastic deformation, causes each of the planes in a polycrystalline material to be slightly different than one another. Like a uniform strain this causes a shift in the peaks but since it is a summation of many shifts this will be observed as line broadening. In a realistic sample both uniform and non-uniform strain will be present.

Electron scattering can cause a decrease in the intensity of a diffracted beam. An electron can be set into oscillation by an x-ray beam the generated electromagnetic wave then interacts with the incident and scattered x-rays.

When regarding a periodic arrangement of atoms in a crystal one can develop a picture of the scattering caused by each atom within a unit cell. As unit cells become more complex, large numbers of atoms in low symmetry arrangements, many interference effects will occur. The vector sum of all of the scattering from all of the atoms in the unit cell is known as the structure factor. Thus, the structure factor is obtained by adding together all of the waves that are scattered by each atom. Using Miller indices,  $hkl$ , to represent the reflecting planes of the material, the equation for the structure factor,  $F$ , is:

$$F_{hkl} = \sum_1^N f_n e^{2\pi i(hu_n + kv_n + lw_n)} \quad (2.2.1.2)$$

Where  $f_n$  is the atomic scattering factor of atom  $n$ ,  $u_n$  is the fractional coordinate in the  $x$  direction,  $v_n$  is the fractional coordinate in the  $y$  direction, and  $w_n$  is the fractional coordinate in the  $z$  direction.

A multiplicity factor comes into play when multiple planes in the crystal have the same spacing. For instance, in a powdered specimen of a cubic lattice some of the crystals will be oriented such that the reflections occur from the 100 plane while others may be in the 010 or 001 planes. By definition all of these planes are equally spaced and therefore all of the diffracted beams coming from them will be multiplicative. So, the relative proportion of planes contributing to the same reflection will come into play for intensity.

An absorption factor occurs when the specimen itself absorbs the diffracted and/or incident x-rays. The calculation of the absorption factor also depends on the geometry of the specific diffraction method in use.

Finally, also of consequence in intensity is the thermal vibration of the atoms. Thermal vibration causes the atoms to be displaced from their ideal positions. When this happens the unit cell expands and causes changes in the plane spacing and therefore also the observed position of the diffraction lines. Interestingly this can be used to calculate the thermal expansion coefficients of material. Furthermore, the intensities of the diffraction lines will decrease while the intensity of the background increase.

### 2.2.2 Synchrotron X-ray Source

In order to rapidly perform a diffraction experiment within the diamond anvil cell a very high intensity x-ray source is needed. The best source of this light, at the time of this writing, is from a synchrotron, which is a special type of cyclotron or particle accelerator. In 1945 Edwin McMillan constructed the first synchrotron at Berkeley Radiation Laboratory where it was used to create many elements beyond the 92 that were known at the time.

Synchrotron radiation is emitted when charged particles, such as electrons, are deflected by a magnetic field. The particles are accelerated in a linear accelerator and/or booster synchrotron before being injected into the storage ring. Once in the storage ring the particles travel with a fixed kinetic energy and the particles are bent such that they travel in a circular path. As the particles are deflected they are accelerated radially and as a result of this acceleration they emit photons. The photon emission causes a loss in energy that must be replenished with a radio-frequency accelerator. Modern synchrotrons do not require a true circular path and generally travel in a straight line until being bent rapidly around a “corner” of a somewhat square geometry, see Figure 11.

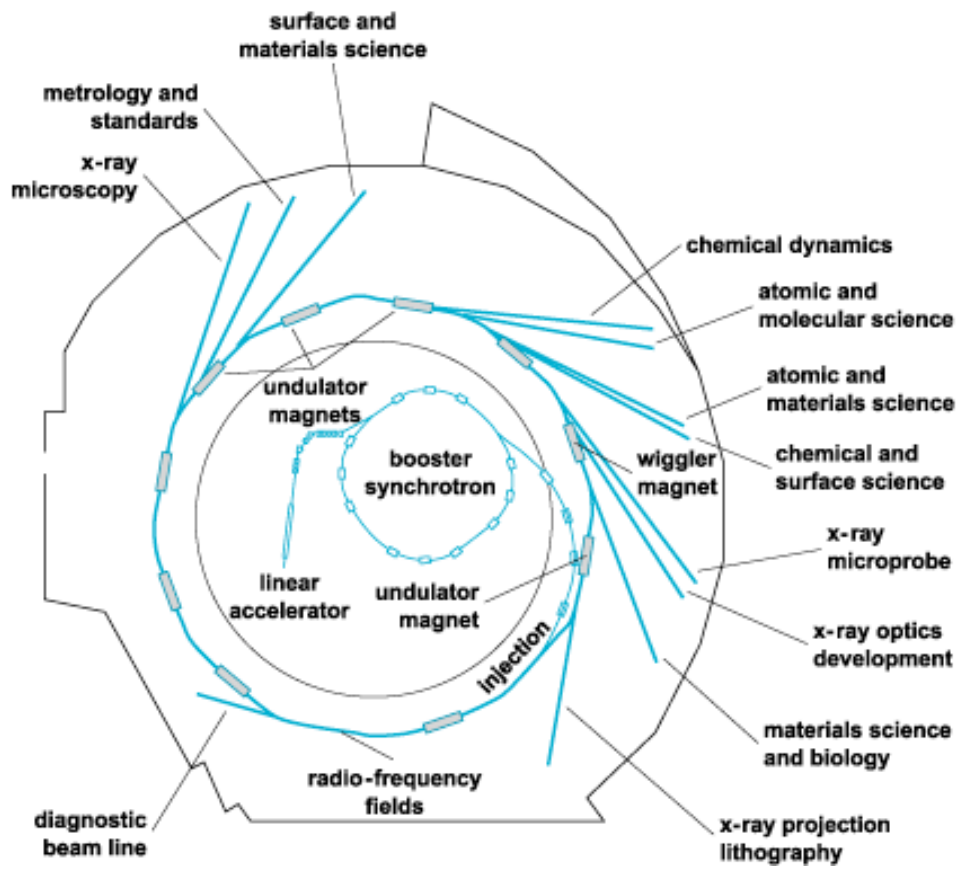


Figure 11. Advanced Light Source. Schematic of the Advanced Light Source synchrotron located in Berkeley, California. Notice that the booster synchrotron is not truly circular [image courtesy of the Advanced Light Source].

### 2.2.3 X-ray Diffraction in the Diamond Anvil Cell

Although there are various methods used to employ x-ray diffraction for experiments in the diamond anvil cell the most convenient method is that of powdered x-ray diffraction while single crystal x-ray diffraction is more difficult. Single crystal diffraction relies on a perfect (the word 'perfect' here not being subjected to the true scientific meaning of perfection) single crystal to be mounted in a precise way such that the incident angle to the plane of atoms is known. In other words it is desired to mount the very small crystal in a very precise way and to make sure that this mounting can survive the extremes of a high-pressure experiment. To combat all of this preciseness in experimental setup one can arrange the sample such that all possible orientations of the crystal are reasonably represented. This method is known as the powder method.

In the powder method, the crystal is reduced to a very fine powder and each small particle of the powder is a crystal. A large number of these small crystals arrange in a random order such that when the incident x-ray beam interacts with the atoms rather than a single diffracted beam per d-spacing occurring a cone of radiation, as shown in Figure 12, is produced. When this cone is incident upon a flat plate detector, data is produced as shown in Figure 13. Each ring in Figure 13 represents a different d-spacing of the cubic crystalline material  $\text{LaB}_6$ . Unfortunately there is another variable in x-ray diffraction experiments that is not avoidable. This variable is the distance from the sample to the detection device. This distance must be known so that the angles of the different radiation cones can be calculated. Much like x-ray diffraction can be used to determine a wavelength of light it can also be used to determine the distance to the sample under

study. To do this it is common to use a calibration material with very well known d-spacings, such as  $\text{LaB}_6$ .

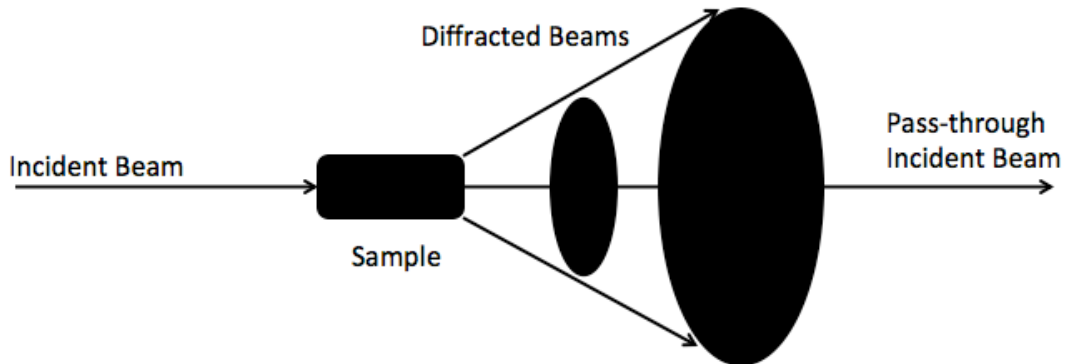


Figure 12. X-ray diffraction from a powdered sample.

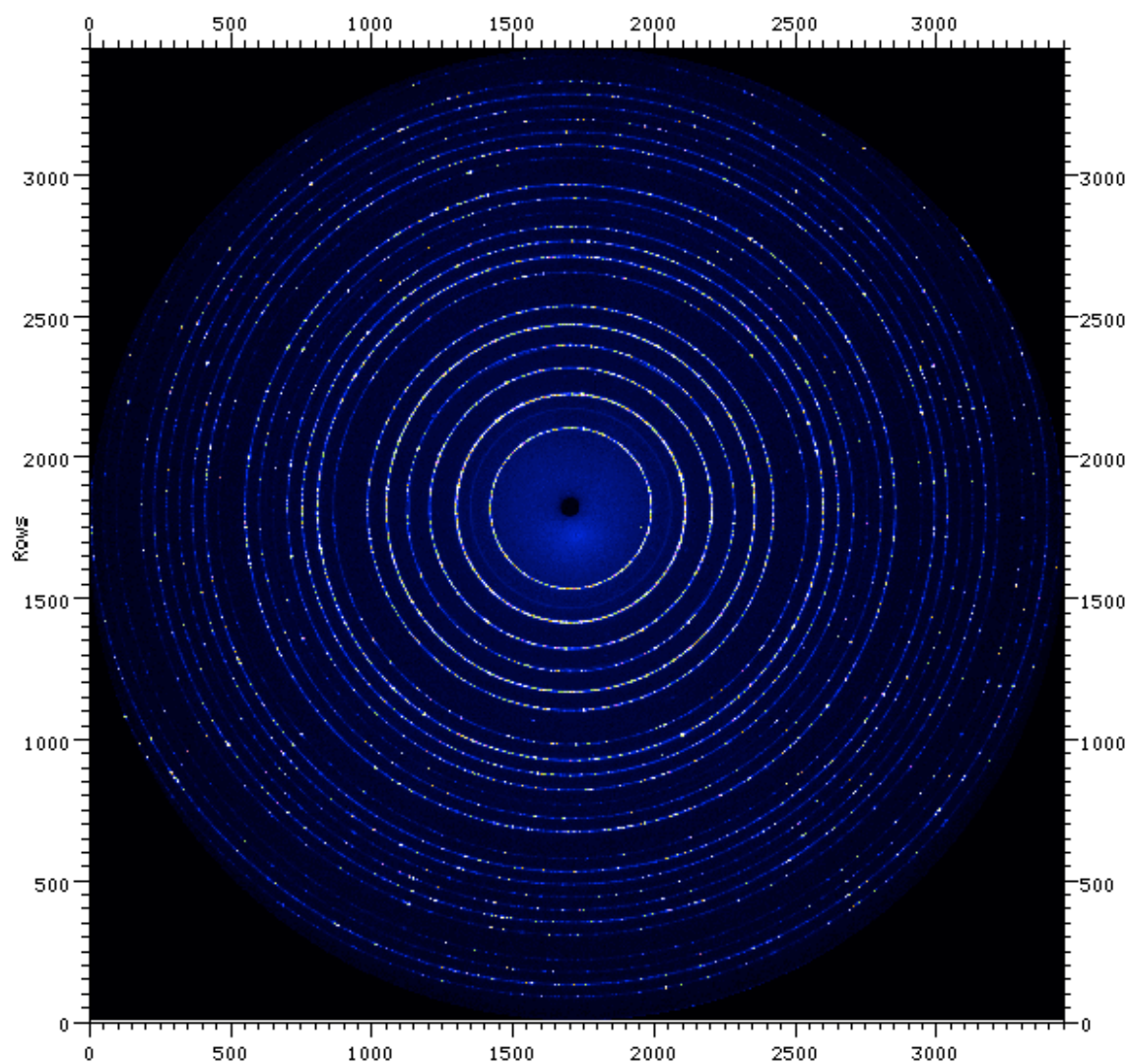


Figure 13. Powered XRD image. Image obtained from synchrotron based powdered x-ray diffraction of  $\text{LaB}_6$ .

In a diamond anvil cell based powdered x-ray diffraction experiment, the diamond anvil cell is placed at a fixed distance from the detector plate. To start the experiment, the cell is loaded with a known sample such as  $\text{LaB}_6$  and a set of data is collected, Figure 13. This initial data set is then used to precisely calculate the distance between the sample chamber within the diamond anvil cell and the detector. The next step is to load the cell

with the powdered sample to be studied along with any pressure-transmitting medium and pressure calibrants. A simplified schematic of a synchrotron x-ray diffraction experiment in a diamond anvil cell is shown in Figure 14.

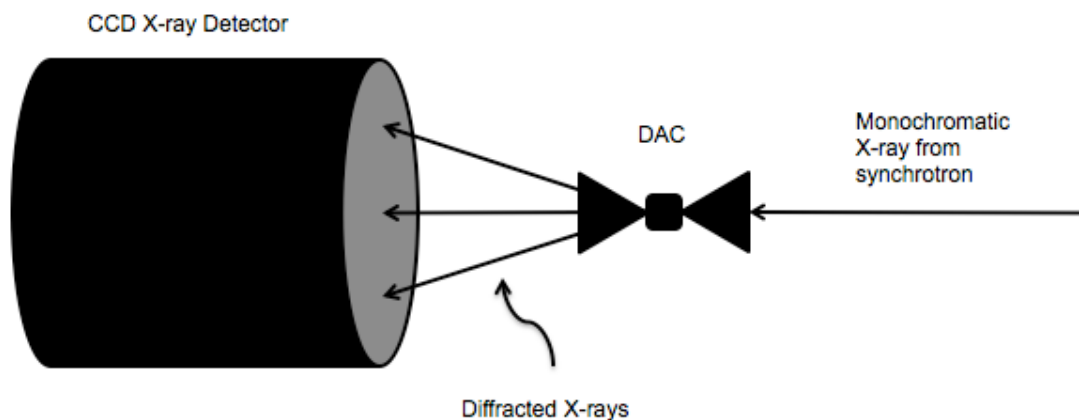


Figure 14. Synchrotron XRD experiment. A monochromatic x-ray beam from a synchrotron source is directed through a sample within a diamond anvil cell. The distance between the cell and the CCD detector must be precisely known so that the angle of the diffracted beams can be known.

#### 2.2.4 Rietveld Refinement Analysis of X-ray Diffraction Data

Developed in 1967 by Hugo Rietveld, Rietveld refinement is an x-ray diffraction analysis method used for full pattern profile refinement and simultaneous crystal structure refinement<sup>61, 62</sup>. All of the factors described above in section 2.2.1 are used to calculate a full diffraction pattern for a material. Therefore, Rietveld refinement is of general interest if most of the information about the material under study is already known. In other words it is difficult, if not impossible, for use in *ab initio* crystal

structure analysis. Once the starting parameters are reasonably close to the proper values a sequence needs to be followed for the parameters that are to be refined. Generally the following parameters can be refined either in sequence or simultaneously (however simultaneous use should be restricted to the highly advanced user): lattice parameters, atomic positions, site occupancies, isotropic/anisotropic thermal vibration, Cagliotti formula, asymmetry, preferred orientation, background, 2-theta zero correction, scale factor, and the isotropic thermal factor, B. All of these parameters require initial values before fitting can begin. Data must be in equal steps in 2-theta and the incident wavelength must be known. Once the initial pattern is set up then profile fitting is obtained by fitting a least squares profile function by stepping point by point through the pattern and minimizing the following:

$$M = \sum_i w_i (y_i - K \sum_k I_k G_{i,k})^2 \quad (2.2.4.1)$$

Where  $w_i$  is the weight of each separate step observation ( $w_i = 1/y_i$ ),  $y_i$  is the background corrected observed intensity, the summation over  $k$  is the summation over the different Bragg peaks,  $K$  is the scale factor, and  $G$  represents the profile function. Written a little more simply where  $y_{ci}$  is the calculated intensity at the  $i$ th step:

$$M = \sum_i w_i (y_i - y_{ci})^2 \quad (2.2.4.2)$$

The calculated intensity is determined from the  $|F_{hkl}|^2$  values from the structural model by summing the background plus all of the contributing reflections.

$$y_{ci} = s \sum_{hkl} L_k |F_{hkl}|^2 \phi(2\theta_i - 2\theta_{hkl}) P_{hkl} A + y_{bi} \quad (2.2.4.3)$$

Where  $s$  is the scale factor,  $hkl$  are the Miller indices,  $L_k$  contains the Lorentz, polarization, and multiplicity factors,  $\phi$  is the reflection profile,  $P_{hkl}$  is the preferred orientation function,  $A$  is the absorption factor,  $F_{hkl}$  is the structure factor and  $y_{bi}$  is the background at step  $i$ .

The software implementation of Rietveld refinement used in this work is known as MAUD (material analysis using diffraction)<sup>63</sup>. MAUD is a highly powerful program and should be approached with caution such that the user does not generate non-factual information. To do this, a series of steps should be followed so that the parameters being refined are done sequentially up until they are all refined well enough in order to be refined simultaneously. The instrument function should be setup first. This defines the key parameters of the actual diffraction instrumentation being used such as a synchrotron or a bench-top diffractometer. The instrument function should be setup using a known sample, often CeO<sub>2</sub> or LaB<sub>6</sub>. Once the instrument function is setup and refined then all of its parameters, besides incident intensity, should be locked for all other analyses that are done for that particular experiment. Next the initial parameters for the material under study should be input. These include, but are not limited to: space group, lattice

parameters, atomic positions, and temperature factors. Before performing an initial fit of the data a background function must also be setup. The background can either be done using polynomials or interpolation. Generally an interpolated background will prove best as long as the user does not need to calculate any physical value from the background itself. Once all of this is setup and the initial fit looks like it will prove useful then the user can begin to unlock parameters and allow them to be refined. First and foremost the user should refine the lattice parameters and scale. These should then be followed by the phase percentage, in the case of multiple phases, and then incrementally by microstrain, and crystal size. For a more advanced analysis other more sensitive factors can be refined if the data is of sufficient quality.

## 2.3 Raman Spectroscopy

### 2.3.1 Raman Spectroscopy

In 1928, Sir Chandrasekhra Venkata Raman discovered the effect, which now bears his name, known as Raman spectroscopy<sup>64</sup>. This discovery quickly led to his winning of the Nobel Prize in Physics in 1930. The Raman effect is when photons are scattered from a material in such a way that a phonon is either absorbed or created. When this occurs, the photon that is scattered has a different energy level than that of the incident photon, as opposed to Rayleigh scattering where the emitted photon is of the same wavelength. Raman scattering occurs in approximately 1 in 10 million of the total scattered photons. In classical theory, Raman scattering can be described mathematically

for a diatomic molecule as follows<sup>65</sup>: The electric field strength,  $E$ , as a function of time,  $t$ , of an electromagnetic wave is:

$$E = E_0 \cos(2\pi\nu_0 t) \quad (2.3.1.1)$$

where  $E_0$  is the vibrational amplitude and  $\nu_0$  is the frequency of the incident photon. If a diatomic molecule is illuminated by this light then an electric dipole moment,  $P$ , is induced:

$$P = \alpha E = \alpha E_0 \cos(2\pi\nu_0 t) \quad (2.3.1.2)$$

where  $\alpha$  is a proportionality constant and is defined as polarizability. If the molecule is vibrating with a frequency  $\nu_m$  then the displacement of the nuclei,  $q$ , can be defined as:

$$q = q_0 \cos(2\pi\nu_m t) \quad (2.3.1.3)$$

where  $q_0$  is the vibrational amplitude. So, for a small vibration  $\alpha$  is a linear function in  $q$ :

$$\alpha = \alpha_0 + \left(\frac{\partial \alpha}{\partial q}\right)_0 q_0 + \dots \quad (2.3.1.4)$$

where  $\alpha_0$  is the polarizability at the equilibrium position. Combining equations yields:

$$P = \alpha_0 E_0 \cos(2\pi\nu_0 t) + \frac{1}{2} \left( \frac{\partial \alpha}{\partial q} \right)_0 q_0 E_0 [\cos\{2\pi(\nu_0 + \nu_m)t\} + \cos\{2\pi(\nu_0 - \nu_m)t\}] \quad (2.3.1.5)$$

The first term, which indicates light being emitted at the same frequency,  $\nu_0$ , as the incident light, represents Rayleigh scattering, the second term represent a frequency of  $\nu_0 + \nu_m$  (anti-Stokes Raman) and  $\nu_0 - \nu_m$  (Stokes Raman) scattered light. It is particularly important to note that if  $\left( \frac{\partial \alpha}{\partial q} \right)_0 = 0$  then the vibration is not Raman active and therefore cannot be studied with Raman spectroscopy.

### 2.3.2 Raman Spectroscopy in the Diamond Anvil Cell

The Raman spectrometer setup used in this work has been specially built in order to work with the constraints imposed by the diamond anvil cell: long working distances and small samples. An incident laser is routed to a beam splitter after which it is focused through a microscope objective into the DAC. Raman scattered light, in a back scattered geometry, then travels back through the objective as well as the beam splitter. A large amount of Rayleigh scattered light is present and must be filtered out using an edge filter. After the filter, the light travels into a spectrometer where the light is diffracted from a grating and then illuminates a nitrogen-cooled CCD. A schematic of this setup can be seen in Figure 15.

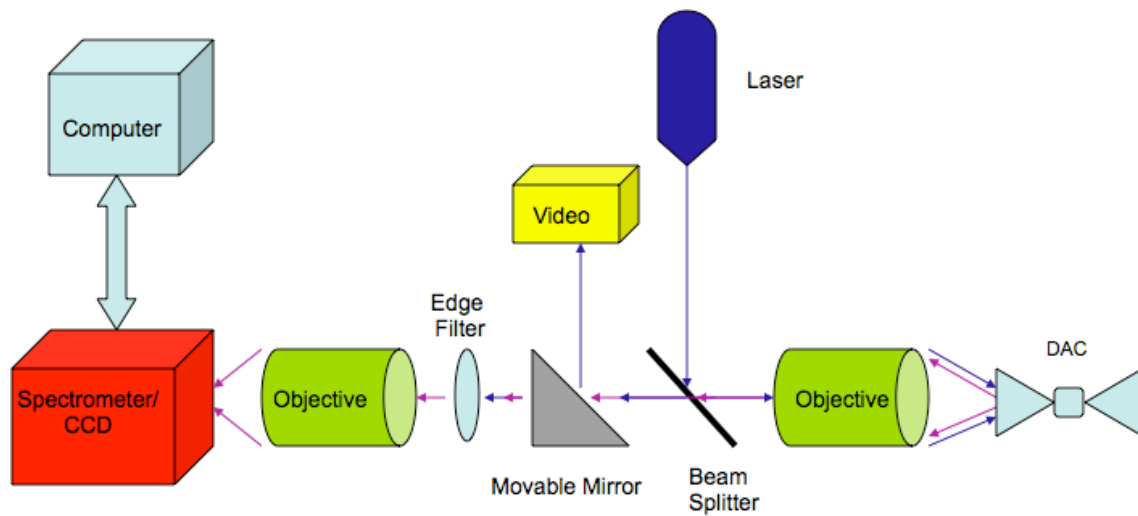


Figure 15. Raman spectroscopy system. Schematic of a Raman spectrometer for use on a diamond anvil cell.

## CHAPTER 3

### DATA AND ANALYSIS

#### 3.1 Bi<sub>2</sub>MoO<sub>6</sub>

##### 3.1.1 Abstract

Synchrotron based x-ray diffraction through a diamond anvil cell was used to determine the equations of state and pressure-induced phase transitions in Bi<sub>2</sub>MoO<sub>6</sub>. It was observed that Bi<sub>2</sub>MoO<sub>6</sub> undergoes a phase transformation at ~ 6.8 GPa. The high-pressure phase can be indexed to the orthorhombic structure and the transition is reversible on decompression from ~ 47 GPa. The bulk moduli of the low and high-pressure phases were calculated, while holding  $K' = 4$ , to be:  $K = 51 \pm 1$  GPa and  $K = 141.5 \pm 0.1$  GPa, respectively.

##### 3.1.2 Introduction

Bi<sub>2</sub>MoO<sub>6</sub> belongs to the Aurivillius family of bismuth-layered compounds of general formula (Bi<sub>2</sub>O<sub>2</sub>)(A<sub>m-1</sub>B<sub>m</sub>O<sub>3m+1</sub>)<sup>66</sup>. These compounds have received much attention for device applications. For instance, some are important candidates for the development of ferroelectric random access memories<sup>5, 67</sup>. They also constitute an important class of oxide anion conductors<sup>66, 68, 69</sup>. Bi<sub>2</sub>MoO<sub>6</sub> also exhibits photocatalytic and photoelectrochemical properties<sup>70-72</sup>.

Bi<sub>2</sub>MoO<sub>6</sub> has three phases at ambient pressure<sup>73-76</sup>. The room temperature structure is *Pca2*<sub>1</sub> (often referred to in the non-standard setting of *P2*<sub>1</sub>*ab* in order to

conform with the convention for Aurivillius phase ferroelectrics of assigning the long axis as  $c$ , and the polar axis as  $a$ )<sup>75</sup>. This structure consists of alternating fluorite-like  $(\text{Bi}_2\text{O}_2)^{2+}$  layers and perovskite-like  $(\text{MoO}_4)^{2-}$  layers.  $\text{Bi}_2\text{MoO}_6$  exhibits a reversible phase transition at 840–877 K<sup>74, 76, 77</sup>. A 3D representation of this structure can be seen in Figure 16. Sankar *et al.* suggested that this phase has the same  $Pca2_1$  symmetry as the low temperature phase but with more distorted  $\text{MoO}_6$  octahedra<sup>76</sup>. However, recent studies have suggested that this orthorhombic phase is nonpolar (point group  $mmm$ )<sup>77</sup>.  $\text{Bi}_2\text{MoO}_6$  also exhibits an irreversible, reconstructive phase transition at 877–943 K into a fluorite-related structure described by the  $P2_1/c$  space group<sup>74, 76, 77</sup>. It is worth adding that recent studies suggested that  $\text{Bi}_2\text{MoO}_6$  might exhibit one more phase transition at 583 K into a polar Aurivillius type phase<sup>77</sup>. The structure of this phase has not been solved but it has been suggested that it has orthorhombic symmetry (point group  $2mm$ )<sup>77</sup>.

Pressure dependent studies of this family of compounds are scarce and only high-pressure Raman spectroscopy has been undertaken for  $\text{Bi}_2\text{MoO}_6$ <sup>31, 34</sup>. Raman scattering studies under pressure have also been reported for a few other crystals belonging to this family of compounds such as  $\text{Na}_{0.5}\text{Bi}_{4.5}\text{Ti}_4\text{O}_{15}$ ,  $\text{Bi}_4\text{Ti}_3\text{O}_{12}$ ,  $\text{Bi}_2\text{WO}_6$  and  $\text{Bi}_2\text{W}_2\text{O}_9$ <sup>32, 33, 78, 79</sup>. These studies showed that high pressure may provide valuable information on the origin of lattice instabilities in this family of compounds. For instance,  $\text{Bi}_2\text{MoO}_6$  has been found to undergo phase transitions at 2.8 GPa and 7.0 GPa while  $\text{Bi}_2\text{WO}_6$  transforms at 3.4 GPa and 6.2 GPa<sup>31, 32</sup>. Raman data also indicated that the pressure-induced structural changes in  $\text{Bi}_2\text{MoO}_6$  are mainly related to the rigid rotations of  $\text{MoO}_6$  octahedra and changes in the  $\text{Bi}_2\text{O}_2$  layers<sup>31, 34</sup>. In contrast to this behavior, distortion of the  $\text{WO}_6$

octahedra significantly increases in  $\text{Bi}_2\text{WO}_6$  with increasing pressure <sup>32</sup>. It was also shown that the high-pressure phases of  $\text{Bi}_2\text{WO}_6$  and  $\text{Bi}_2\text{MoO}_6$  are orthorhombic and most likely centrosymmetric <sup>31, 32, 34</sup>.

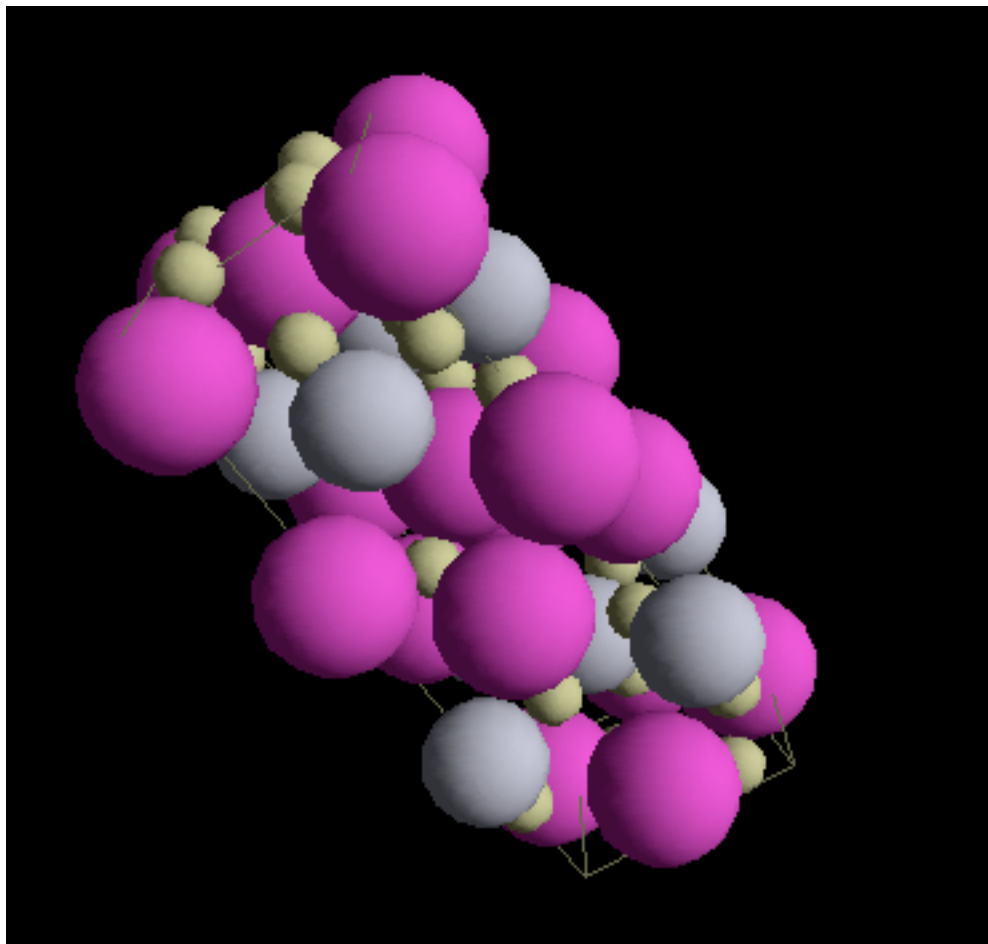


Figure 16. 3D model of  $\text{Bi}_2\text{MoO}_6$ . The large purple atoms are bismuth, the medium grey atoms are molybdenum and the small tan atoms are oxygen.

### 3.1.3 Material and Methods

High-pressure x-ray experiments were performed at room temperature at beamline X17C of the National Synchrotron Light Source (NSLS) at Brookhaven National Laboratory.  $\text{Bi}_2\text{MoO}_6$  was prepared as described by Maczka *et al.*<sup>31</sup>. The powdered samples were loaded into a Mao-Bell type diamond anvil cell along with a small amount of gold, which was used to determine the pressure inside of the cell<sup>56, 57</sup>. Hydrostatic conditions were obtained in the cell by filling approximately 1/4<sup>th</sup> of the hole with sample and then adding a mixture of methanol:ethanol:water (16:3:1) for the pressure transmitting medium<sup>43</sup>. For each experiment a spring steel gasket with a hole of  $\sim 100 \mu\text{m}$  diameter drilled into a pre-indented area was used to contain the sample. The experiment was performed to  $\sim 47 \text{ GPa}$  using monochromatic x-rays ( $\lambda = 0.4066 \text{ \AA}$ ) and a two-dimensional (2D) imaging plate at a distance of 262.29 mm from the sample. The distance of the 2D plate and broadening due to the instrument were calculated at ambient conditions using  $\text{CeO}_2$ . X-ray diffraction patterns were refined using the Rietveld method with the MAUD program<sup>63</sup>. Atomic coordinates and temperature factors for use in refinement were obtained from Van Den Elzen *et al.*<sup>75</sup> and can be seen in Table 1. The following parameters were refined: scale factors, background coefficients (third order polynomial), unit-cell parameters, volume fraction of Au and  $\text{Bi}_2\text{MoO}_6$ , atomic positions, incident intensity and microstrain. Delft line broadening was used along with an isotropic size-strain model<sup>80</sup>. The crystallite size was refined at the initial pressure and it was then held constant for the remainder of the experiments. R<sub>w</sub> factors, as reported by MAUD, were typically between 7% and 15%.

Table 1: Atomic coordinates and temperature factors for  $\text{Bi}_2\text{MoO}_6$ <sup>75</sup>.

Atom	x	y	z	B
Bi(1)	0.5221	0.4222	0.9794	0.63
Bi(2)	0.4812	0.0779	0.9731	0.54
Mo	0.0099	0.2486	0	0.47
O(1)	0.039	0.14	0.099	0.76
O(2)	0.24	0.999	0.196	0.76
O(3)	0.25	0.5	0.26	0.76
O(4)	0.693	0.236	0.255	0.76
O(5)	0.214	0.265	0.35	0.76
O(6)	0.597	0.358	0.41	0.76

### 3.1.4 Results and Discussion

Representative integrated diffraction images for  $\text{Bi}_2\text{MoO}_6$  are shown in Figure 17. It was found that under compression the structure remains in the  $Pca2_1$  orthorhombic crystal system to the highest pressure achieved in this study,  $\sim 47$  GPa, which is consistent with previous findings in the analog  $\text{Bi}_2\text{WO}_6$ <sup>32</sup>.

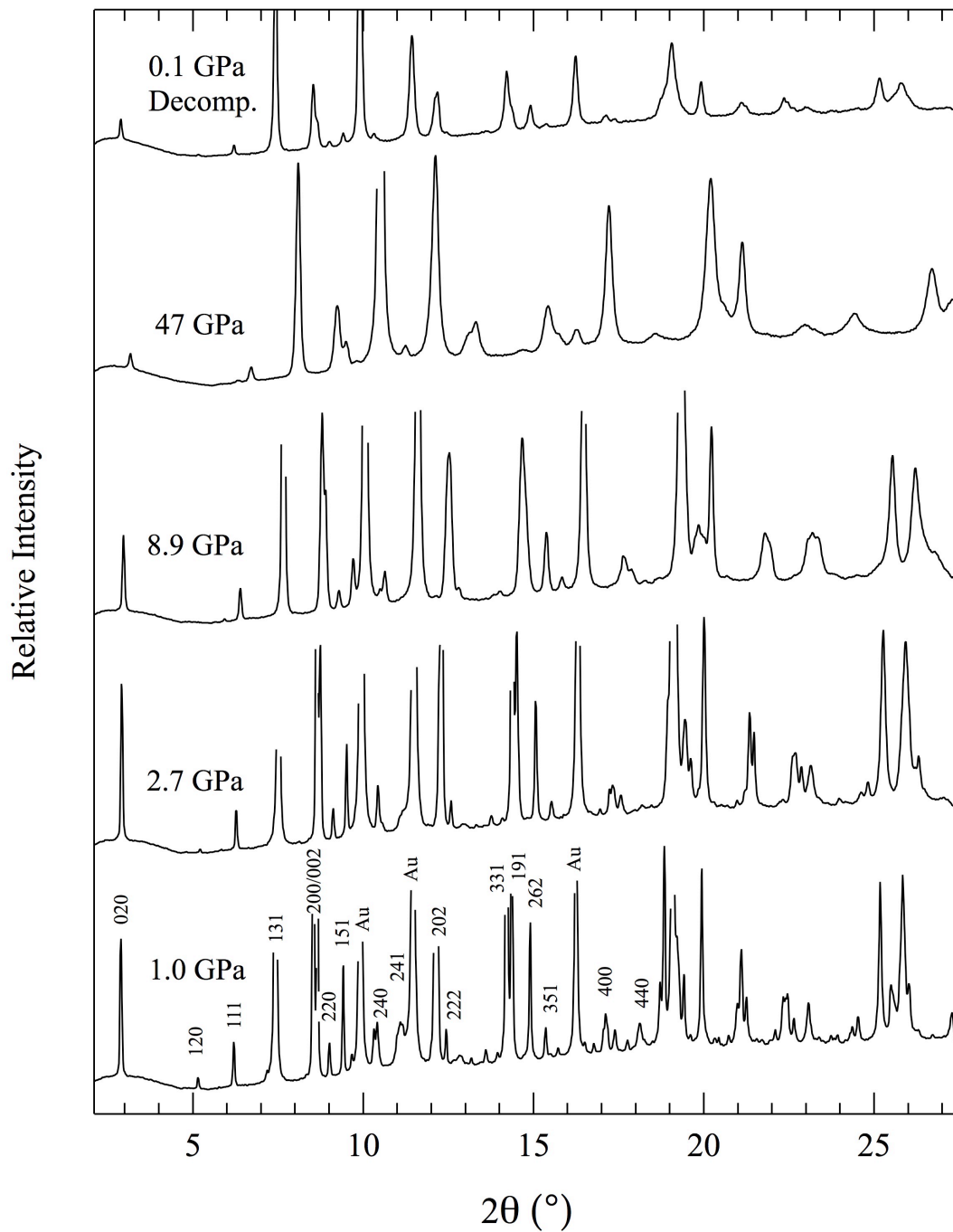


Figure 17.  $\text{Bi}_2\text{MoO}_6$  XRD. X-ray diffraction data at select pressures for  $\text{Bi}_2\text{MoO}_6$ . Miller indices are labeled for a select few peaks at 1 GPa. Peaks of gold are observed due to their use as pressure markers.

Figure 18 shows a plot of unit cell volume versus pressure. The unit cell volume at 1 GPa was calculated from the experimental data to be  $481.3 \pm 0.1 \text{ \AA}^3$ . This value is in good agreement with the atmospheric pressure value of  $489.23 \text{ \AA}^3$  obtained by neutron diffraction <sup>81</sup>. A bend in the compressibility curve is observed between 6.8 and 7.4 GPa and suggests a phase transition has occurred. A first order Birch-Murnaghan equation of state <sup>82</sup> was fit to the unit cell volume low-pressure phase for pressures up to 6.8 GPa. This was accomplished by a Taylor expansion of the Helmholtz free energy in terms of the Eulerian finite-strain parameter  $f_v = (1/2)[(V/V_0)^{-2/3} - 1]$  which yields the following isothermal equation of state for the pressure (P):

$$P = 3K_0 f_v (1 + 2f_v)^{5/2} [1 + a f_v + \dots] \quad (3.1.4.1)$$

where  $K_0$  is the bulk modulus and the third order coefficient of energy in strain is given by

$$a = 3(K'_0 - 4)/2 \quad (3.1.4.2)$$

Here, primes indicate differentiation with respect to pressure, and the subscript zero refers to zero pressure conditions. Defining the normalized pressure,  $F_v$ , as

$$F_v = P/[3f_v(1+2f_v)^{5/2}] \quad (3.1.4.3)$$

yields a third-order finite-strain equation of state that is linear in  $f_v$ :

$$F_v = K_0[1 - 1.5(4 - K'_0)f_v] \quad (3.1.4.4)$$

When the P-V data are input into the form of Eq. 3.1.4.4, the intercept, which yields the bulk modulus, can be calculated using a least squares method fit to a line. The slope of this fit indicates the deviation of  $K'_0$  from a value of 4. As  $K'_0$  is close to 4 for most materials, a second-order equation of state is often adequate<sup>82, 83</sup> and given the nature of our data, we hold  $K'_0 = 4$ . The calculation yielded a bulk modulus of  $K = 51 \pm 1$  GPa.

For data from 6.8 GPa to 47 GPa, the region of stability for the high-pressure phase, a G vs g analysis was performed<sup>84</sup>. The difficulty in performing the same “F vs f” analysis for a high-pressure phase that cannot be maintained at atmospheric conditions is that the initial density is not known and therefore you cannot calculate the strain, f. To get around this one defines an arbitrary reference density  $\rho^*$  and the density ratio,  $\alpha$ , is defined as:

$$\alpha = (\rho^* / \rho_{02})^{1/3} \quad (3.1.4.5)$$

Where the subscripts one and two refer to the low- and high- pressure phases respectively. With this an effective strain,  $g$ , can be defined as:

$$g = (f_2 + 1/2)\alpha^{-2} - 1 \quad (3.1.4.6)$$

This can be rearranged such that:

$$f_2 = (g + 1/2)\alpha^2 - 1/2 \quad (3.1.4.7)$$

Substituting  $f_2$  into  $f$  of equation 3.1.4.1 now yields:

$$P = 3K_{02}\alpha^5(1+2g)^{5/2}[(\alpha^2 - \frac{1}{2})(1 + -\frac{1}{2}a_2(1-\alpha^2) + \dots)] \quad (3.1.4.8)$$

Thusly a new normalized pressure can be defined as:

$$G = \frac{P}{3(1+2g)^{5/2}} \quad (3.1.4.9)$$

and

$$G = a + bg + cg^2 + dg^3 + \dots \quad (3.1.4.10)$$

Furthermore, the most convenient way to define strain at zero pressure,  $g_0$ , is:

$$g_0 = \frac{1 - \alpha^2}{2\alpha^2} \quad (3.1.4.11)$$

Such that  $G(g_0) = 0$  and changing variables  $g' = g - g_0$  yields:

$$G = (a + bg_0 + cg_0^2 + dg_0^3) + (b + 2cg_0 + 3dg_0^2)g' + (c + 2dg_0)(g')^2 + d(g')^3 \quad (3.1.4.12)$$

This can subsequently be expanded as a polynomial in  $g'$ :

$$G = \lambda_0 + \lambda_1 g' + \dots \quad (3.1.4.13)$$

With  $\lambda_0 = 0$  and  $\lambda_1 = \alpha^7 K_{02}$ . Finally and rather simply one finds  $g_0$  by fitting to the experimental data and:

$$g_0 = \frac{-a}{b} \quad (3.1.4.14)$$

$$K_{02} = \frac{\lambda_1}{\alpha^7} \quad (3.1.4.15)$$

$$\rho_{02} = \rho^* \alpha^{-3} \quad (3.1.4.16)$$

This analysis yielded a bulk modulus of  $K = 141.5 \pm 0.1$  GPa with  $K'$  held at 4 and an atmospheric unit cell volume of  $463.8 \pm 0.1 \text{ \AA}^3$ . Upon decompression the unit cell volume follows the high-pressure equation of state until approximately 1.7 GPa where the data point lies between the two calculated equations of state. Upon full decompression the sample returns to its original, low-pressure, structure. This reversibility was also observed in Raman data by Maczka *et al.*<sup>31</sup>.

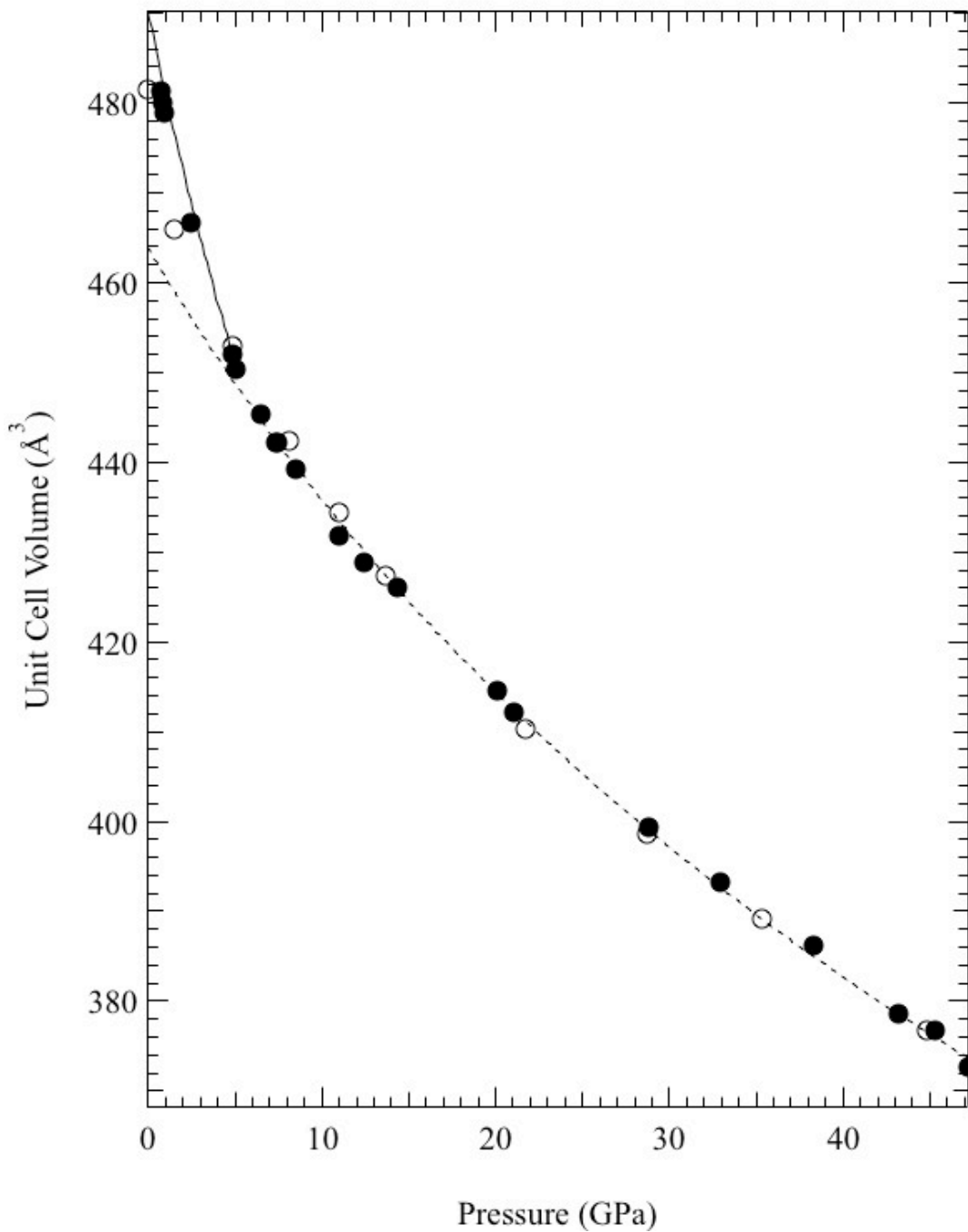


Figure 18.  $\text{Bi}_2\text{MoO}_6$  V vs P. Plot of volume versus pressure for  $\text{Bi}_2\text{MoO}_6$ . Volume under compression is shown with closed circles and decompression with open circles. Uncertainties generated by MAUD are smaller than the symbols and may not be truly representative of experimental uncertainty. A Birch-Murnaghan equation of state fit for the low-pressure phase is shown with the solid line,  $K =$

51 ±1 GPa. A G vs g analysis was performed for the high-pressure phase and is shown as a dashed line with  $K = 141.5 \pm 0.1$  GPa and  $V_0 = 463.8 \pm 0.1 \text{ \AA}^3$ .

Figure 19 shows a plot of normalized unit cell parameters versus pressure. Anisotropic compression is observed in three different instances. Immediately upon compression the ‘c’ parameter is more compressible. At ~2.4 GPa the ‘b’ parameter separates from the ‘a’ parameter. The pressure at which this takes place coincides with the subtle second-order phase transition at 2.8 GPa reported in a recent high pressure Raman experiment <sup>31</sup>. Finally, at ~7.4 GPa, the ‘a’ and ‘c’ parameters compress isotropically while ‘b’ follows a more compressible curve. The higher compressibility of the ‘b’ axis is in the layered arrangement of the fluorite-like  $(\text{Bi}_2\text{O}_2)^{2+}$  layers and the perovskite-like  $(\text{MoO}_4)^{2-}$  layers. The location, in pressure, of this behavior is at nearly the same pressure of 7.0 GPa where Maczka *et al.* observed the narrowing, and increased intensity, of several Raman modes <sup>31</sup>. Furthermore, they observed that several Raman modes, which are due to orthorhombic distortions, remain near 850 and 720  $\text{cm}^{-1}$  suggesting that the crystal structure remains orthorhombic.

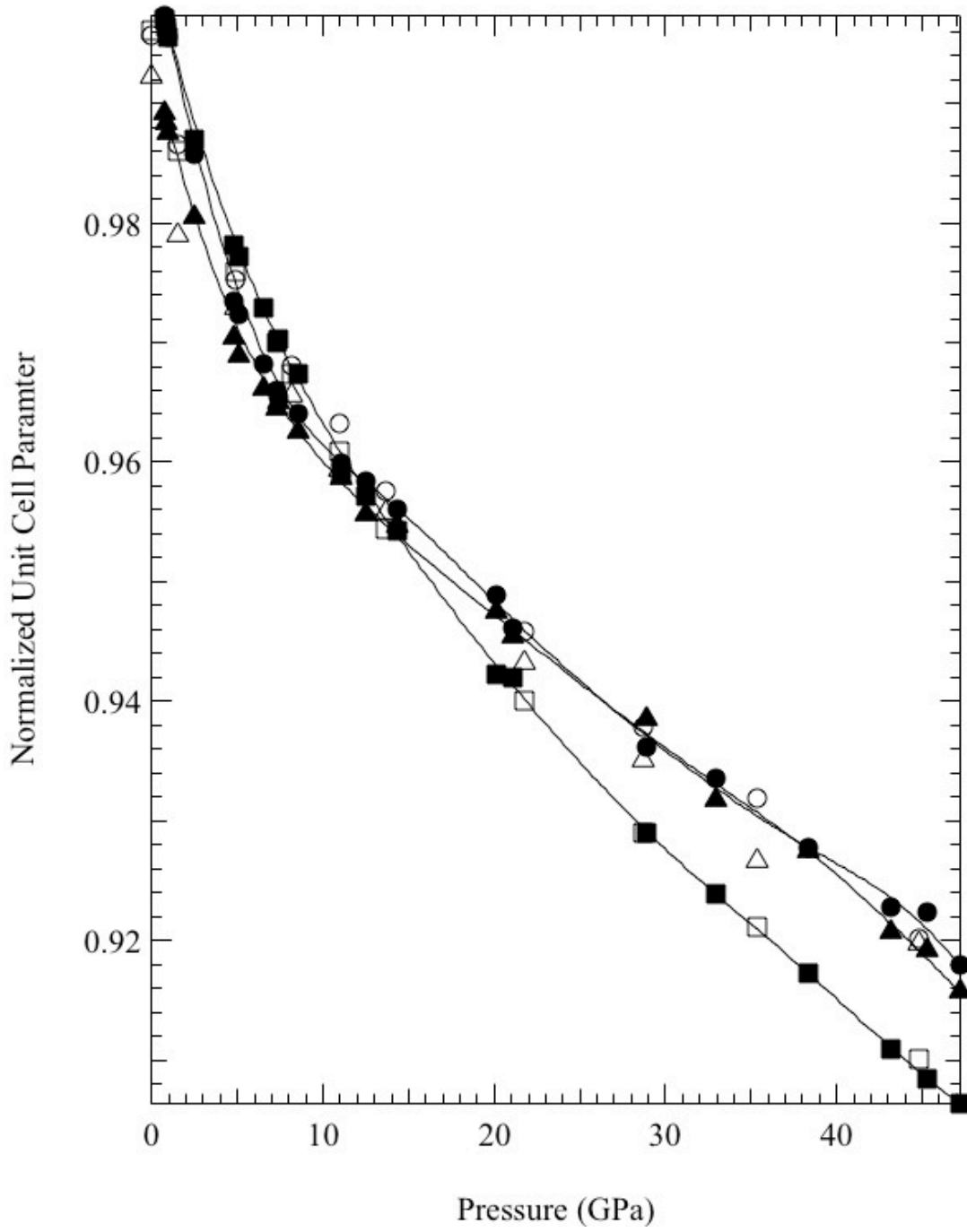


Figure 19.  $\text{Bi}_2\text{MoO}_6$  normalized unit cell parameters. Plot of normalized unit cell parameters versus pressure. The parameters for 'a', 'b', and 'c' are shown with circles, squares, and triangles respectively (closed for compression and open for decompression). The solid lines are cubic spline interpolations and are meant only as a guide to the eye. Uncertainties generated by MAUD are smaller than the

symbols and may not be truly representative of experimental uncertainty. Different anisotropic compression is observed in three different pressure regimes. Once immediately upon compression where the 'c' parameter is more compressible, again at  $\sim 2.4$  GPa where the 'b' parameter separates from the 'a' parameter, and finally at  $\sim 7.4$  GPa where the 'a' and 'c' parameters compress isotropically while 'b' follows a different curve.

Figure 20 shows a plot of microstrain versus pressure. Microstrain increases linearly upon compression until  $\sim 20$  GPa where it levels to a constant. Behavior under decompression is similar. Nothing is observed in the microstrain to give further insight in to the phase transitions.

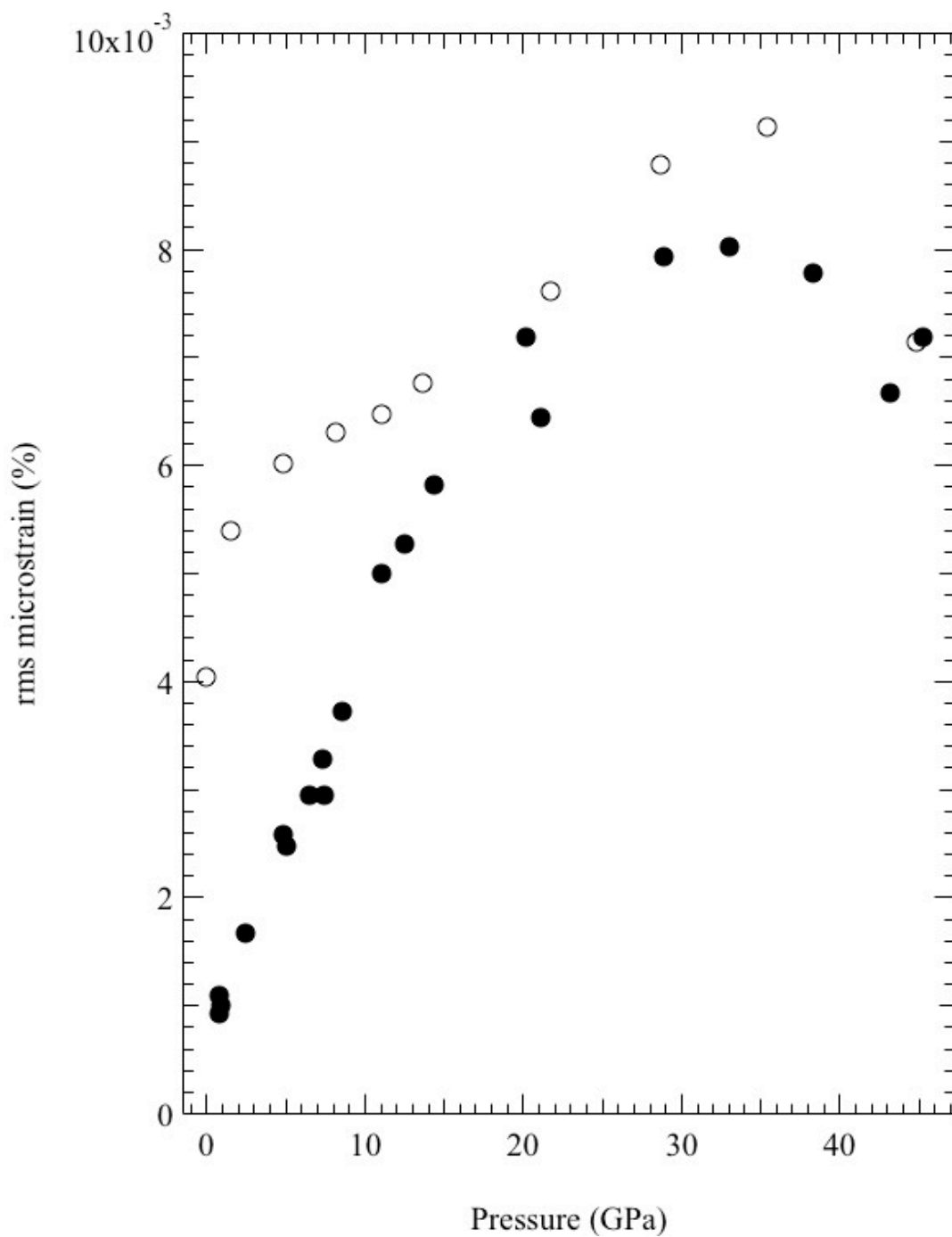


Figure 20. Bi<sub>2</sub>MoO<sub>6</sub> microstrain vs pressure. Plot of the room mean square (rms) microstrain versus pressure. Closed circles are for compression and open circles are for decompression. The microstrain increases linearly upon compression, to ~ 20 GPa, with no indication of a phase change.

A review of the atomic positions from Rietveld refinement shows minor fluctuations in some of the oxygen atoms between 6.8 and 7.4 GPa. However, the fluctuations are small and no trends are observed. Perhaps a high-pressure neutron diffraction experiment could reveal a more detailed picture of the phase transition.

### 3.1.5 Conclusions

Synchrotron based x-ray diffraction was used to determine the equations of state and phase transitions in  $\text{Bi}_2\text{MoO}_6$ . Based upon the equation of state, it was observed that  $\text{Bi}_2\text{MoO}_6$  undergoes a phase transformation at  $\sim 6.8$  GPa which confirms the previous reports from Raman experiments<sup>31, 34</sup>. This high-pressure phase continues to be indexed to an orthorhombic structure and upon decompression from  $\sim 47$  GPa reverts to the low-pressure structure at  $\sim 1.7$  GPa. The bulk moduli were calculated to be  $K = 51 \pm 1$  GPa and  $K = 141.5 \pm 0.1$  GPa for the low and high pressure phases respectively.

## 3.2 Bi<sub>2</sub>W<sub>2</sub>O<sub>9</sub>

### 3.2.1 Abstract

Synchrotron based x-ray diffraction through a diamond anvil cell was used to determine the equation of state and pressure-induced phase transitions in Bi<sub>2</sub>W<sub>2</sub>O<sub>9</sub>. It was observed that Bi<sub>2</sub>W<sub>2</sub>O<sub>9</sub> undergoes a phase transformation at ~11 GPa. This new high-pressure phase is yet to be identified and requires further study. It remains until the highest pressure achieved in this study ~ 49.3 GPa. The bulk modulus of the low-pressure phase was calculated to be:  $K = 76.6 \pm 0.2$  GPa while holding  $K' = 4$ .

### 3.2.2 Introduction

Bi<sub>2</sub>W<sub>2</sub>O<sub>9</sub> belongs to the Aurivillius family of bismuth-layered compounds of general formula (Bi<sub>2</sub>O<sub>2</sub>)(A<sub>m-1</sub>B<sub>m</sub>O<sub>3m+1</sub>)<sup>66</sup>. The room temperature structure is *Pna2<sub>1</sub>* with  $a = 5.440$  Å,  $b = 5.413$  Å, and  $c = 23.740$  Å<sup>85</sup>. This structure consists of alternating fluorite-like (Bi<sub>2</sub>O<sub>2</sub>)<sup>2+</sup> layers and perovskite-like (MoO<sub>4</sub>)<sup>2-</sup> layers. Similar to Bi<sub>2</sub>WO<sub>6</sub> and Bi<sub>2</sub>MoO<sub>6</sub>, this orthorhombic structure can be regarded as derived from a high symmetry tetragonal structure (space group *I4/mmm*)<sup>86-88</sup>. However, the structure of Bi<sub>2</sub>W<sub>2</sub>O<sub>9</sub> is unique among bismuth-layered materials since the direction of the cooperative displacement of the W atoms is antiparallel from one octahedral layer to the other and from one (W<sub>2</sub>O<sub>7</sub>)<sup>2-</sup> slab to the other therefore leading the Bi<sub>2</sub>W<sub>2</sub>O<sub>9</sub> to be non-ferroelectric<sup>85</sup>. For Bi<sub>2</sub>W<sub>2</sub>O<sub>9</sub>, no A cation is present on the sites of the W<sub>2</sub>O<sub>7</sub> slabs<sup>85, 89</sup>. Therefore, Bi<sub>2</sub>W<sub>2</sub>O<sub>9</sub> is the  $m = 2$  member of the family of cation-deficient Aurivillius phases. As of this writing only Bi<sub>2</sub>MoO<sub>6</sub>, Bi<sub>2</sub>WO<sub>6</sub>, and Bi<sub>2</sub>W<sub>2</sub>O<sub>9</sub> have been identified as belonging to

this cation-deficient Aurivillius family<sup>85</sup>. A 3D model of the structure can be seen in Figure 21. Recently,  $\text{Bi}_2\text{W}_2\text{O}_9$  was found to be a photocatalytic material for  $\text{H}_2$  and  $\text{O}_2$  evolution as well as photodegradation of organic compounds<sup>3, 90</sup>. It was also found to be a promising material for microwave applications<sup>4</sup>.

Pressure-dependent studies of this family of compounds are scarce. Raman-scattering studies under pressure were carried out for  $\text{Na}_{0.5}\text{Bi}_{4.5}\text{Ti}_4\text{O}_{15}$ ,  $\text{Bi}_4\text{Ti}_3\text{O}_{12}$ ,  $\text{Bi}_2\text{WO}_6$ ,  $\text{Bi}_2\text{MoO}_6$ , and  $\text{Bi}_2\text{W}_2\text{O}_9$ <sup>31-33, 78, 79</sup>. These published reports show that high-pressure studies may provide information on the origin of lattice instabilities in this family of compounds. The previous works showed that  $\text{Na}_{0.5}\text{Bi}_{4.5}\text{Ti}_4\text{O}_{15}$  and  $\text{Bi}_4\text{Ti}_3\text{O}_{12}$  exhibit second-order phase transitions at about 1.94 GPa and near 3 GPa, respectively<sup>78</sup>. It was also shown that  $\text{Bi}_2\text{MoO}_6$ ,  $\text{Bi}_2\text{WO}_6$ , and  $\text{Bi}_2\text{W}_2\text{O}_9$  undergo two phase transitions at 2.8/7.0 GPa, 3.4/6.2 GPa, and 2.8/4.8 GPa, respectively<sup>31-33</sup>. Therefore, different bismuth layered crystals behave in a different way upon application of pressure, in spite of the same underlying  $I4/mmm$  structure. To better understand the lattice instabilities a high-pressure XRD study of  $\text{Bi}_2\text{W}_2\text{O}_9$  has been completed in this work.

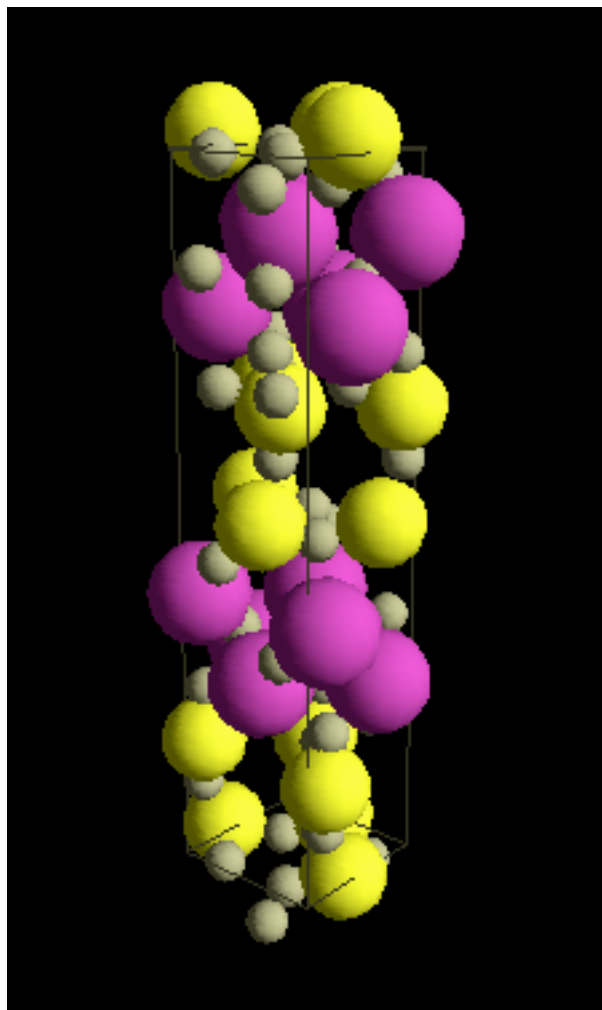


Figure 21. 3D model of  $\text{Bi}_2\text{W}_2\text{O}_9$ . The large purple atoms are bismuth, the medium yellow atoms are tungsten and the small tan atoms are oxygen.

### 3.2.3 Material and Methods

High-pressure x-ray experiments were performed to  $\sim 49$  GPa for  $\text{Bi}_2\text{W}_2\text{O}_9$  as described above for  $\text{Bi}_2\text{MoO}_6$ .  $\text{Bi}_2\text{W}_2\text{O}_9$  was prepared as described by Maczka *et al.*<sup>31</sup>. Atomic coordinates and temperature factors, Table 2, for use in refinement were obtained from Champarnaud-Mesjard *et al.*<sup>85</sup>. R<sub>w</sub> factors, as reported by MAUD, were typically between 7.5% and 13.1%.

Table 2: Atomic coordinates and temperature factors for  $\text{Bi}_2\text{W}_2\text{O}_9$  <sup>85</sup>.

Atom	x	y	z	B
Bi(1)	0.1442	0.4779	0.2899	1.13
Bi(2)	0.1443	0.9812	0.3984	1.24
W(1)	0.1631	-0.0031	0.1708	0.5
W(2)	0.8322	0.5086	0.0172	0.58
O(1)	0.9092	0.76	0.3396	1.1
O(2)	0.9371	0.2266	0.3401	1.2
O(3)	0.7638	0.5544	0.0951	0.9
O(4)	0.8989	0.1941	0.1633	1.3
O(5)	0.0671	0.297	0.0281	1.1
O(6)	0.7699	0.4088	0.9365	1.8
O(7)	0.9888	0.7214	0.1839	0.9
O(8)	0.998	0.8005	0.0096	0.8
O(9)	0.2148	0.0512	0.2445	1.1

### 3.2.4 Results and Discussion

Representative integrated diffraction images for  $\text{Bi}_2\text{W}_2\text{O}_9$  are shown in Figure 22. It was found that under compression that the initial structure,  $Pna2_1$  orthorhombic, transitions to a different structure at  $\sim 11$  GPa and remains up to at least the highest pressure achieved in this study,  $\sim 49.3$  GPa.

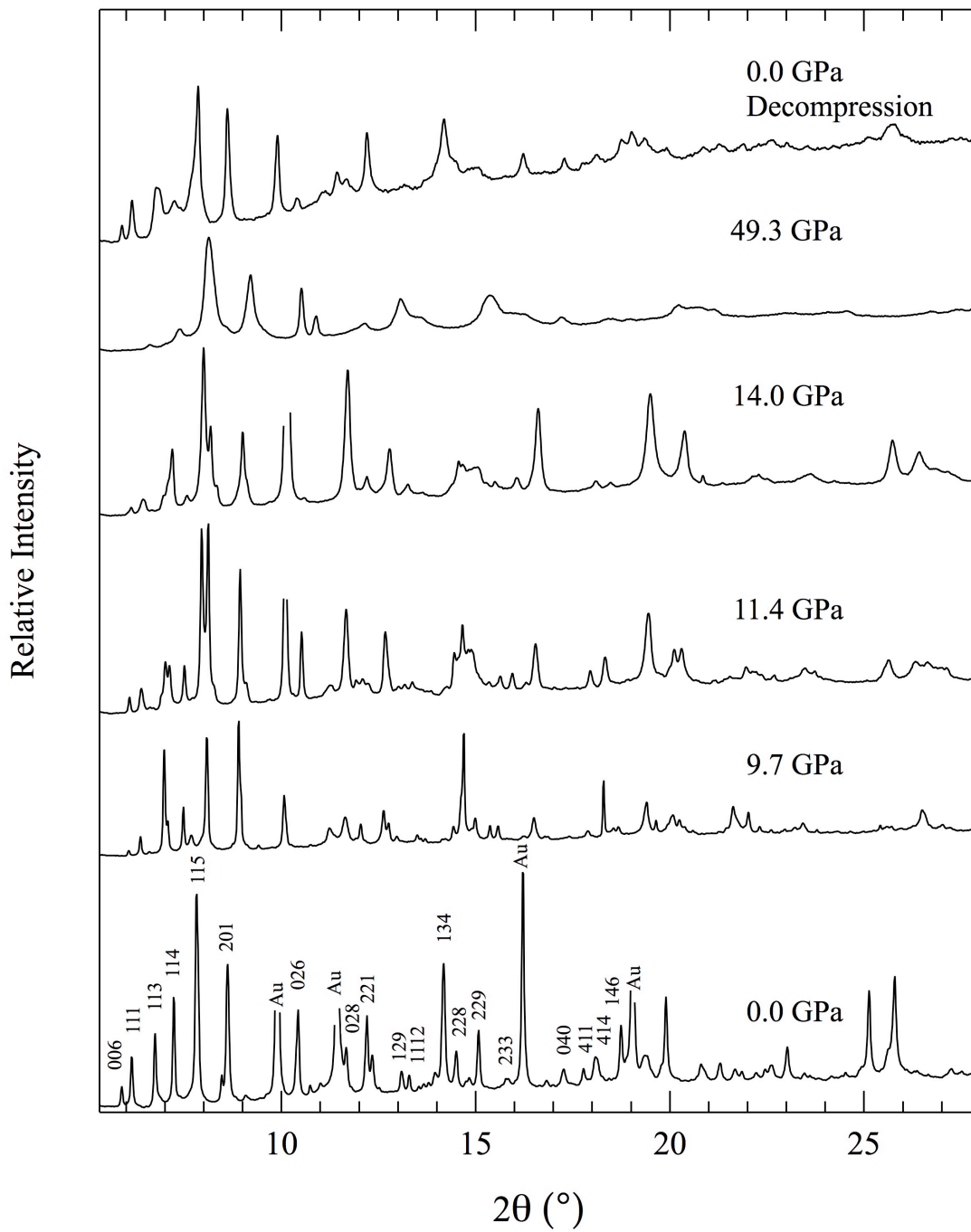


Figure 22.  $\text{Bi}_2\text{W}_2\text{O}_9$  XRD. X-ray diffraction data at select pressures for  $\text{Bi}_2\text{W}_2\text{O}_9$ . Peaks of gold are observed due to their use as pressure markers.

Figure 23 shows a plot of unit cell volume versus pressure. The unit cell volume at atmospheric pressure from within the diamond anvil cell was calculated from the experimental data to be  $697.1 \pm 0.2 \text{ \AA}^3$ . This value is in good agreement with the atmospheric pressure value of  $699.06 \text{ \AA}^3$  obtained by single crystal x-ray diffraction<sup>85</sup>. A first order Birch-Murnaghan equation of state<sup>82</sup> was fit to the unit cell volume for pressures up to 11.1 GPa. The calculation yielded a bulk modulus of  $K = 76.6 \pm 0.2 \text{ GPa}$  while holding  $K' = 4$ .

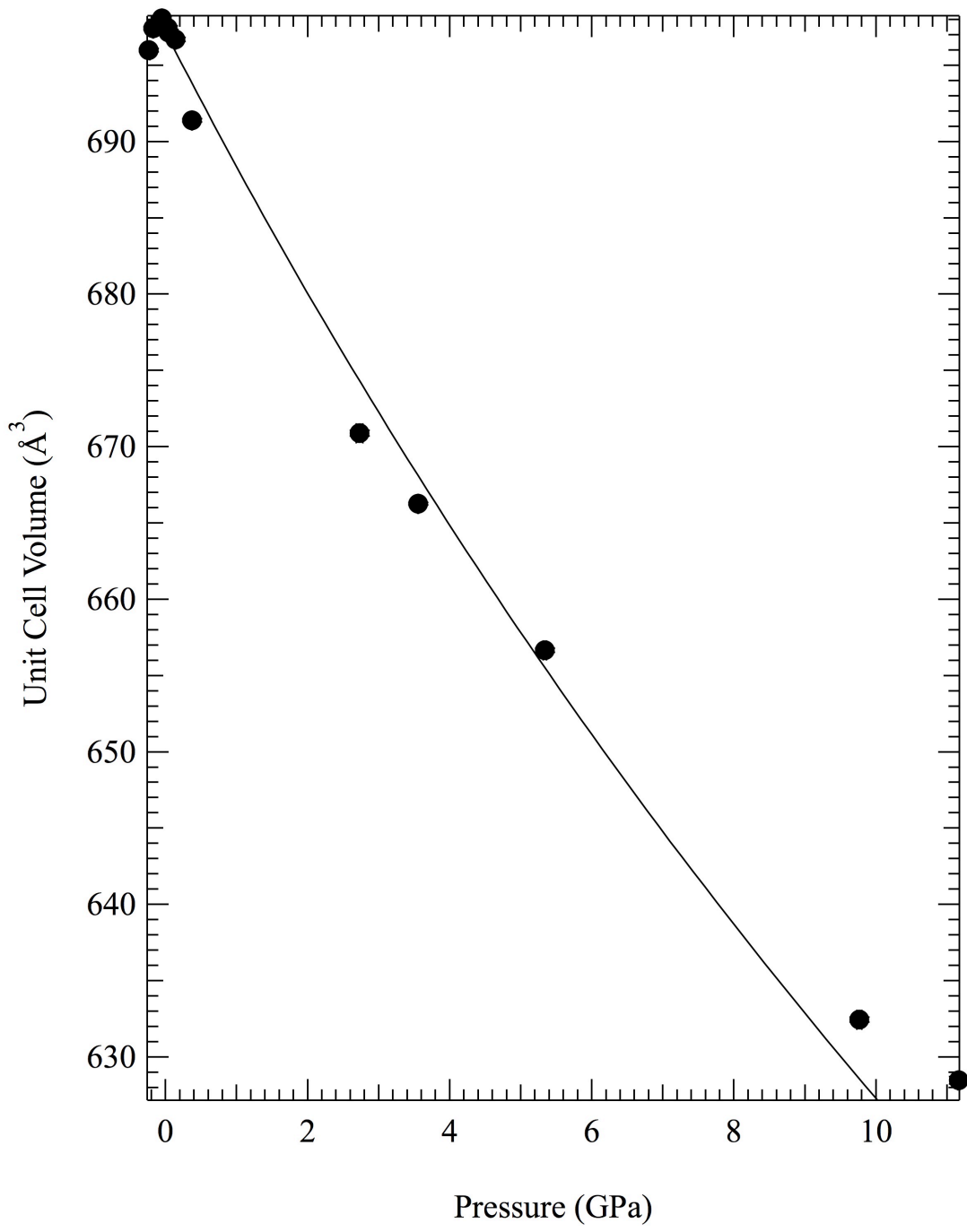


Figure 23.  $\text{Bi}_2\text{W}_2\text{O}_9$  V vs P. Plot of volume versus pressure for  $\text{Bi}_2\text{W}_2\text{O}_9$ . Uncertainties generated by MAUD are smaller than the symbols and may not be truly representative of experimental uncertainty. A Birch-Murnaghan equation of state fit for the low-pressure phase is shown with the solid line,  $K = 76.6 \pm 0.2$  GPa while holding  $K' = 4$ .

### 3.2.5 Conclusions

Synchrotron based x-ray diffraction was used to determine the equation of state and phase transitions in  $\text{Bi}_2\text{W}_2\text{O}_9$ . Based upon the XRD data, it was observed that  $\text{Bi}_2\text{W}_2\text{O}_9$  undergoes a phase transformation at  $\sim 11$  GPa. This new high-pressure phase has yet to be identified. The bulk modulus for the low-pressure phase was calculated to be  $K = 76.6 \pm 0.2$  GPa while holding  $K' = 4$ .

### 3.3 Bi<sub>2</sub>WO<sub>6</sub>

#### 3.3.1 Abstract

Synchrotron based x-ray diffraction through a diamond anvil cell was used to determine the equations of state and pressure-induced phase transitions in Bi<sub>2</sub>WO<sub>6</sub>. It was observed that Bi<sub>2</sub>WO<sub>6</sub> undergoes a phase transformation between 4.8 and 8.3 GPa. The high-pressure phase can be indexed to the orthorhombic structure and remains until the highest pressure achieved in this study ~ 48.5 GPa. The bulk moduli of the low and high-pressure phases were calculated, while holding  $K' = 4$ , to be:  $K = 52.2 \pm 0.3$  GPa. and  $K = 121.8 \pm 0.1$  GPa, respectively.

#### 3.3.2 Introduction

The rare bismuth tungstate mineral russellite was first discovered in the tungsten concentrates at the Castle-an-Dinas mine, St. Columb Major, Cornwall, in 1934 and described as a new species by Hey and Bannister <sup>91</sup>. Although russellite remains a somewhat poorly characterized mineral species, the artificial compound Bi<sub>2</sub>WO<sub>6</sub> has been studied in great detail as a result of its exhibiting a number of interesting solid-state and optical properties such as ferroelectricity, piezoelectricity, pyroelectricity, and a non-linear dielectric susceptibility <sup>92-96</sup>.

Bi<sub>2</sub>WO<sub>6</sub> belongs to the Aurivillius family of bismuth-layered compounds of general formula (Bi<sub>2</sub>O<sub>2</sub>)(A<sub>m-1</sub>B<sub>m</sub>O<sub>3m+1</sub>) <sup>66</sup>. The room temperature structure is *Pca2<sub>1</sub>* with  $a = 5.43726$  Å,  $b = 16.43018$  Å, and  $c = 5.458422$  Å <sup>97</sup>. This structure consists of alternating fluorite-like (Bi<sub>2</sub>O<sub>2</sub>)<sup>2+</sup> layers and perovskite-like (MoO<sub>4</sub>)<sup>2-</sup> layers. Similar to

$\text{Bi}_2\text{W}_2\text{O}_9$  and  $\text{Bi}_2\text{MoO}_6$ , this orthorhombic structure can be regarded as derived from a high symmetry tetragonal structure (space group  $I4/mmm$ )<sup>86-88</sup>.  $\text{Bi}_2\text{WO}_6$  is an archetypal  $m = 1$  member of this family of compounds. As of this writing only  $\text{Bi}_2\text{MoO}_6$ ,  $\text{Bi}_2\text{WO}_6$ , and  $\text{Bi}_2\text{W}_2\text{O}_9$  have been identified as belonging to the cation-deficient Aurivillius family<sup>85</sup>. A 3D model of the structure can be seen in Figure 24.

$\text{Bi}_2\text{WO}_6$  is a well-known ferroelectric compound with a high Curie temperature ( $T_c \sim 960$  °C) and the largest spontaneous polarization among bismuth layered ferroelectrics<sup>5, 98, 99</sup>. This compound exhibits a second order phase transition at 660 °C to the  $B2cb$  structure and a first order phase transition at 960 °C to the  $A2/m$  structure<sup>98</sup>. The transition at 960 °C is unique among Aurivillius ferroelectrics because, whereas the other bismuth layered compounds transform at high temperature into the centrosymmetric  $I4/mmm$  structure, this prototype tetragonal phase is never reached in  $\text{Bi}_2\text{WO}_6$ <sup>98</sup>. Instead, this material exhibits a reconstructive phase transition into the  $A2/m$  structure<sup>98</sup>.

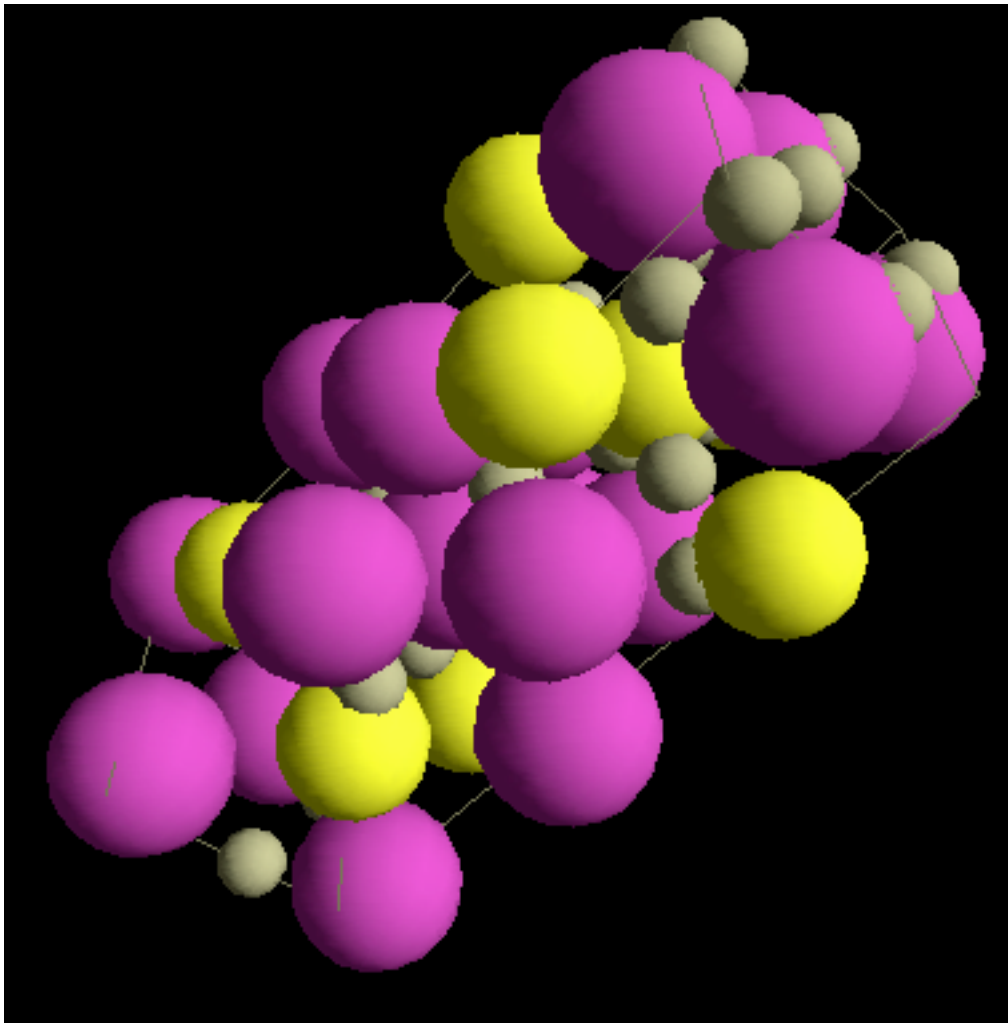


Figure 24. 3D model of  $\text{Bi}_2\text{WO}_6$ . The large purple atoms are bismuth, the medium yellow atoms are tungsten and the small tan atoms are oxygen.

### 3.3.3 Material and Methods

High-pressure x-ray experiments were performed to 48.5 GPa for  $\text{Bi}_2\text{WO}_6$  as described above for  $\text{Bi}_2\text{W}_2\text{O}_9$  and  $\text{Bi}_2\text{MoO}_6$ .  $\text{Bi}_2\text{WO}_6$  was prepared as described by Maczka *et al.*<sup>31</sup>. Atomic coordinates and temperature factors, Table 3, for use in

refinement were obtained from Knight *et al.*<sup>97</sup>. Rw factors, as reported by MAUD, were typically between 7.3% and 9.6%.

Table 3: Atomic coordinates and temperature factors for Bi<sub>2</sub>WO<sub>6</sub><sup>97</sup>.

Atom	x	y	z	B
Bi(1)	0.52055	0.42238	0.97608	0.436
Bi(2)	0.4824	0.07712	0.97956	0.595
W(1)	0.00706	0.24948	0	0.159
O(1)	0.05787	0.14016	0.0768	0.852
O(2)	0.25969	0.99942	0.26347	0.687
O(3)	0.24029	0.50056	0.25763	0.397
O(4)	0.70587	0.23237	0.25069	0.786
O(5)	0.21308	0.26392	0.33079	0.957
O(6)	0.56157	0.35984	0.56183	0.689

### 3.3.4 Results and Discussion

Representative integrated diffraction images for Bi<sub>2</sub>WO<sub>6</sub> are shown in Figure 25. It was found that under compression the structure remains in the *Pca2*<sub>1</sub> orthorhombic crystal system to the highest pressure achieved in this study, ~ 48.5 GPa, which is consistent with previous findings<sup>32</sup>.

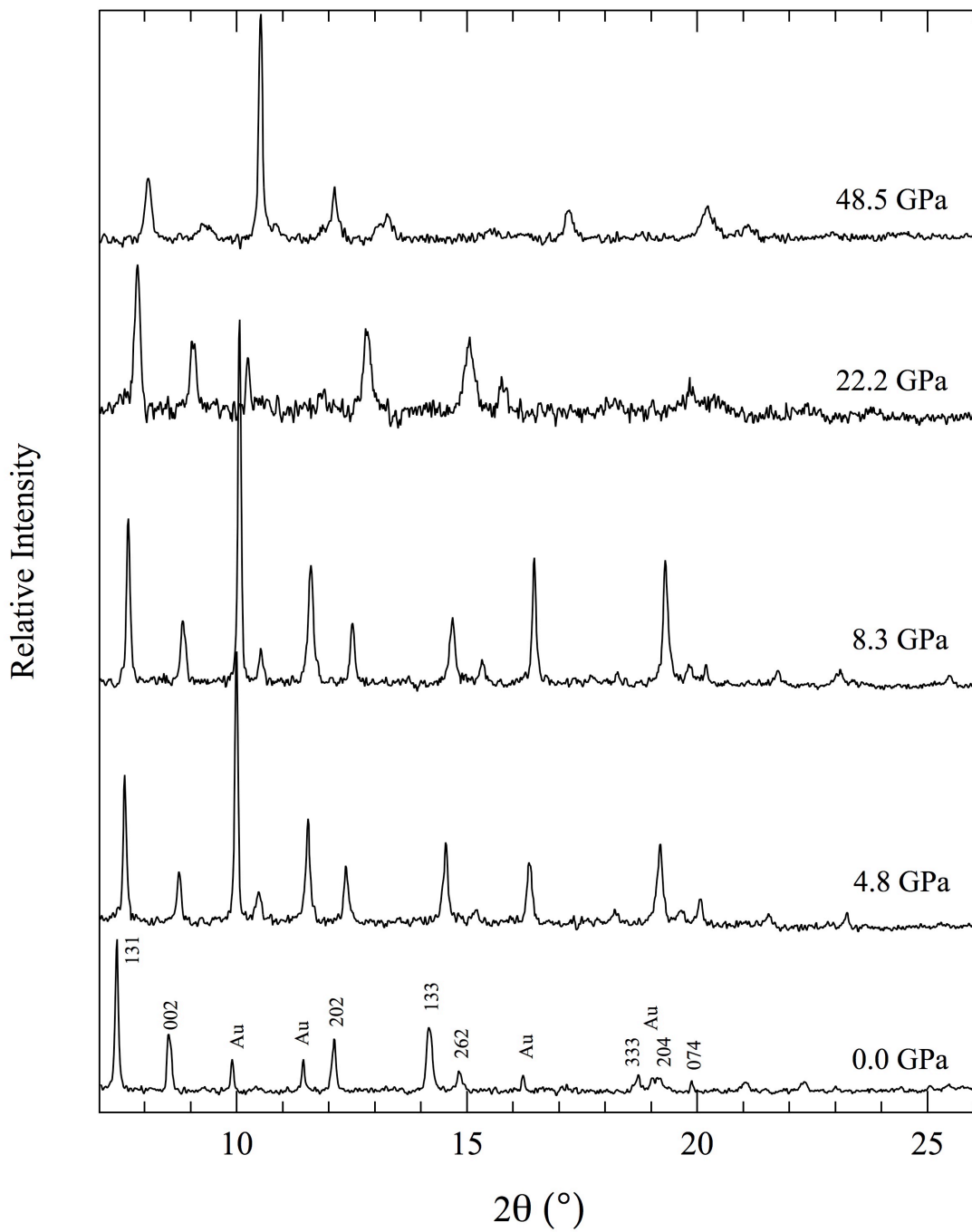


Figure 25.  $\text{Bi}_2\text{WO}_6$  XRD. X-ray diffraction data at select pressures for  $\text{Bi}_2\text{WO}_6$ . Peaks of gold are observed due to their use as pressure markers.

Figure 26 shows a plot of unit cell volume versus pressure. The unit cell volume at atmospheric pressure from within the diamond anvil cell was calculated from the experimental data to be  $487.6 \pm 0.2 \text{ \AA}^3$ . This value is in good agreement with the atmospheric pressure value of  $487.63 \text{ \AA}^3$  obtained by neutron diffraction<sup>97</sup>. A bend in the compressibility curve is observed between 4.8 and 8.3 GPa and suggests a phase transition has occurred. This phase change corresponds to a previous high-pressure Raman study that observes a transition at 6.2 GPa<sup>32</sup>. A first order Birch-Murnaghan equation of state<sup>82</sup> was fit to the unit cell volume low-pressure phase for pressures up to 4.8 GPa. The calculation yielded a bulk modulus of  $K = 52.2 \pm 0.3 \text{ GPa}$ .

For data from 8.3 GPa to 48.5 GPa, the region of stability for the high-pressure phase, a G vs g analysis was performed<sup>84</sup>. This analysis yielded a bulk modulus of  $K = 121.8 \pm 0.1 \text{ GPa}$  with  $K'$  held at 4 and an atmospheric unit cell volume of  $459.0 \pm 0.1 \text{ \AA}^3$ . No decompression data is available due to a gasket failure at the end of the experiment.

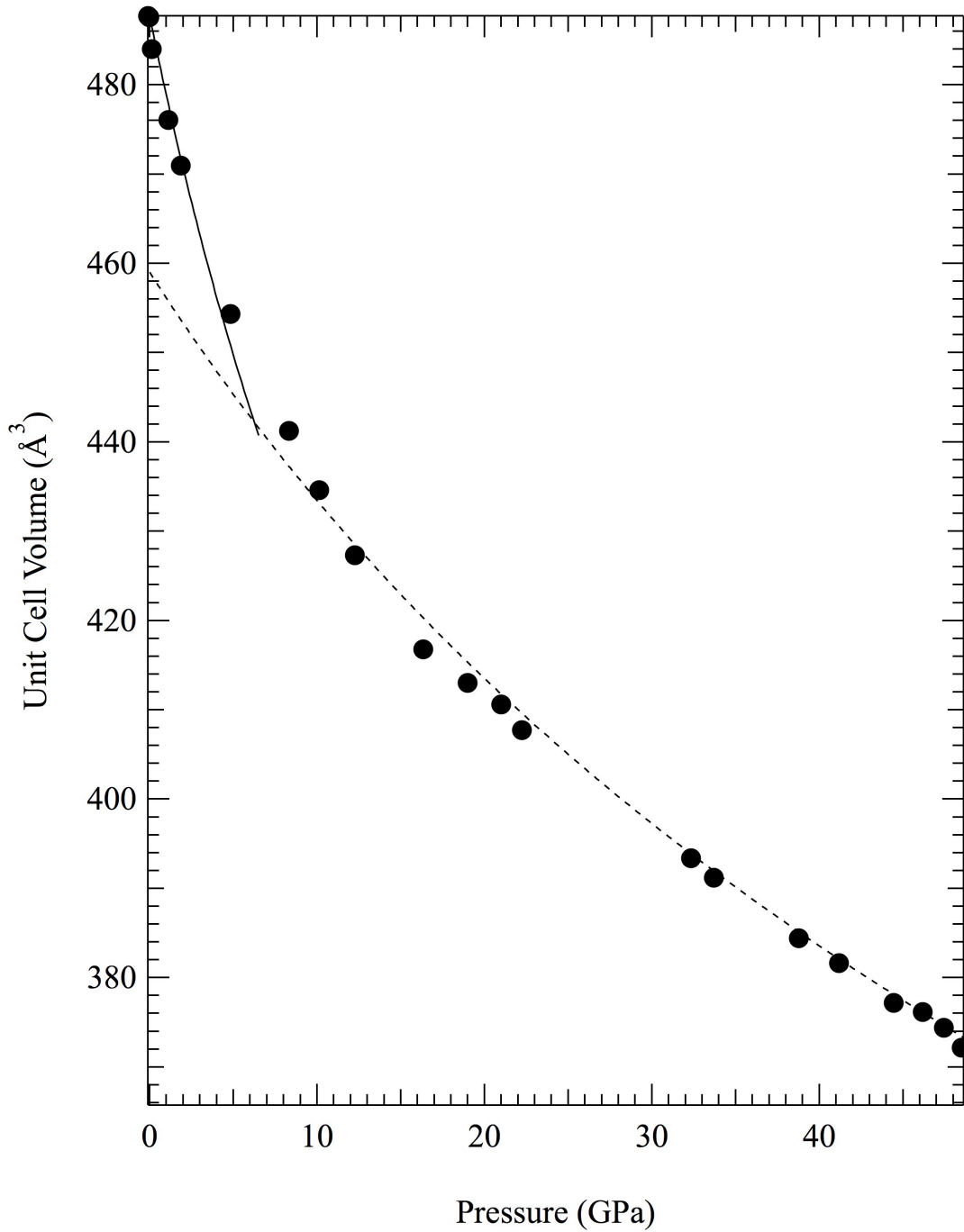


Figure 26.  $\text{Bi}_2\text{WO}_6$  V vs P. Plot of volume versus pressure for  $\text{Bi}_2\text{WO}_6$ . Uncertainties generated by MAUD are smaller than the symbols and may not be truly representative of experimental uncertainty. A Birch-Murnaghan equation of state fit for the low-pressure phase is shown with the solid line,  $K = 52.2 \pm 0.3$

GPa. A G vs g analysis was performed for the high-pressure phase and is shown as a dashed line with  $K = 121.8 \pm 0.1$  GPa and  $V_0 = 459.0 \pm 0.1 \text{ \AA}^3$ .

Figure 27 shows a plot of normalized unit cell parameters versus pressure. Anisotropic compression is observed in two different instances. At  $\sim 8.3$  GPa the 'c' parameter separates from the 'a' and 'b' parameters. The pressure at which this takes place is slightly higher than with the subtle second-order phase transition at 6.2 GPa reported in a recent high pressure Raman experiment <sup>32</sup>. Finally, at  $\sim 30$  GPa, the 'b' parameter compressibility changes such that it better matches that of the 'c' parameter.

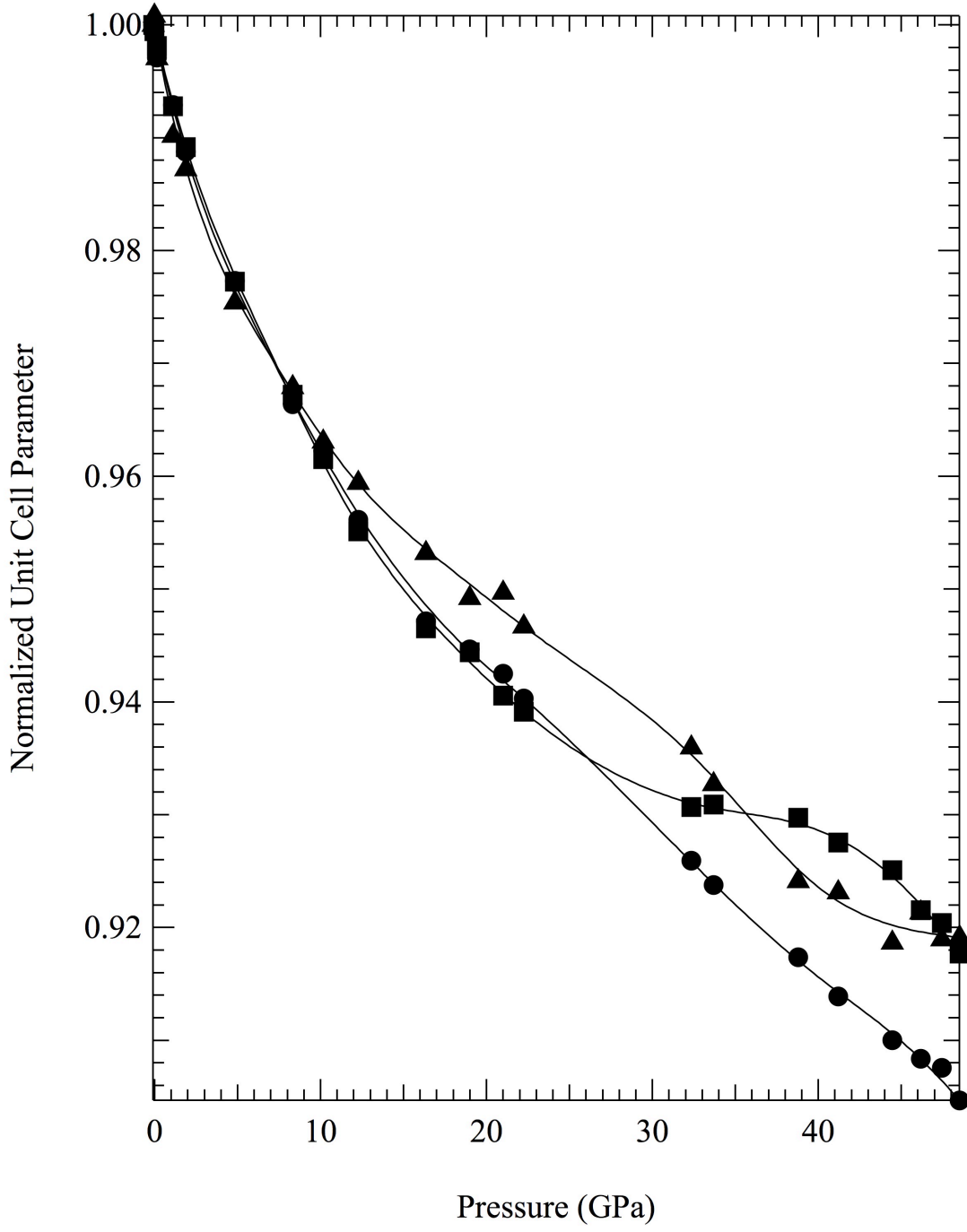


Figure 27.  $\text{Bi}_2\text{WO}_6$  normalized unit cell parameters. Plot of normalized unit cell parameters versus pressure. The parameters for 'a', 'b', and 'c' are shown with circles, squares, and triangles respectively (closed for compression and open for decompression). The solid lines are cubic spline interpolations and are meant only as a guide to the eye. Uncertainties generated by MAUD are smaller than the

symbols and may not be truly representative of experimental uncertainty. Anisotropic compression is observed in the 'c' parameter is observed near the proposed phase transition of  $\sim 8.3$  GPa. Further anisotropic compression is observed in the 'b' parameter at  $\sim 30$  GPa.

### 3.3.5 Conclusions

Synchrotron based x-ray diffraction was used to determine the equations of state and phase transitions in  $\text{Bi}_2\text{WO}_6$ . Based upon the equation of state, it was observed that  $\text{Bi}_2\text{WO}_6$  undergoes a phase transformation between 4.8 and 8.3 GPa, which partially confirms the previous reports from Raman experiments that a phase change occurs at 6.2 GPa<sup>32</sup>. This previous report also observed a phase change at 3.4 GPa however our study did not observe it. This high-pressure phase continues to be indexed to an orthorhombic structure up to at least 48.5 GPa. The bulk moduli were calculated, with  $K'$  held at 4, to be  $K = 52.2 \pm 0.3$  GPa and  $K = 121.8 \pm 0.1$  GPa for the low- and high-pressure phases respectively.

### 3.4 La<sub>2</sub>Mo<sub>4</sub>O<sub>15</sub>

#### 3.4.1 Abstract

Synchrotron based x-ray diffraction was used to determine the equations of state and phase transitions in La<sub>2</sub>Mo<sub>4</sub>O<sub>15</sub>. It was observed that La<sub>2</sub>Mo<sub>4</sub>O<sub>15</sub> undergoes phase transformations at ~2 GPa and ~17 GPa. The intermediate structure has yet to be identified and the high-pressure phase is amorphous. On decompression the transition from the high pressure disordered structure is irreversible from ~21 GPa. The bulk modulus of the initial phase was calculated to be,  $K = 65.7 \pm 4.7$  GPa with  $K'$  held at 4.

#### 3.4.2 Introduction

The lanthanide molybdate compounds form a large family of materials with interesting physical properties. These properties depend on the crystal structures of these oxides and on the oxidation state of molybdenum<sup>100</sup>. In the case of the highest oxidation state one can mention the ferroelectric/ferroelastic properties of Gd<sub>2</sub>Mo<sub>3</sub>O<sub>12</sub><sup>101</sup>, the unusual negative thermal expansion of at least 10 materials from the Ln<sub>2</sub>Mo<sub>3</sub>O<sub>12</sub> and Ln<sub>2</sub>W<sub>3</sub>O<sub>12</sub> groups<sup>102</sup>, the catalytic properties of La<sub>2</sub>MoO<sub>6</sub><sup>103</sup>, and the fast oxide- ion conduction in La<sub>2</sub>Mo<sub>3</sub>O<sub>9</sub><sup>104-106</sup>. Interest has been focused on the solid state chemistry and physics of rare earth (RE) molybdates because of their ferroelectricity and ferroelasticity<sup>107</sup>, their applications to lasers<sup>108</sup>, phosphors<sup>109-111</sup>, and ionic conductors<sup>104, 105</sup>.

The family of RE<sub>2</sub>Mo<sub>4</sub>O<sub>15</sub> is known to exhibit different structures with RE = La<sup>100</sup>, Tb<sup>112</sup>, Ho<sup>113</sup> (monoclinic), RE = Ce<sup>114</sup>, Pr<sup>113</sup>, Sm<sup>115</sup> (triclinic). La<sub>2</sub>Mo<sub>4</sub>O<sub>15</sub> crystallizes in a monoclinic space group *P21/n* with cell parameters  $a = 9.0357 \text{ \AA}$ ,  $b =$

12.7737 Å,  $c = 10.6408$  Å ,  $\beta = 90.2491^\circ$ . The structure consists of molybdenum octahedra [MoO<sub>6</sub>] and tetrahedra [MoO], and lanthanum polyhedra [LaO<sub>9</sub>]. Molybdenum polyhedra are connected together, forming large units [Mo<sub>6</sub>O<sub>22</sub>], isolated by lanthanum polyhedral chains <sup>100</sup>. A 3D model of the structure can be observed in Figure 28.

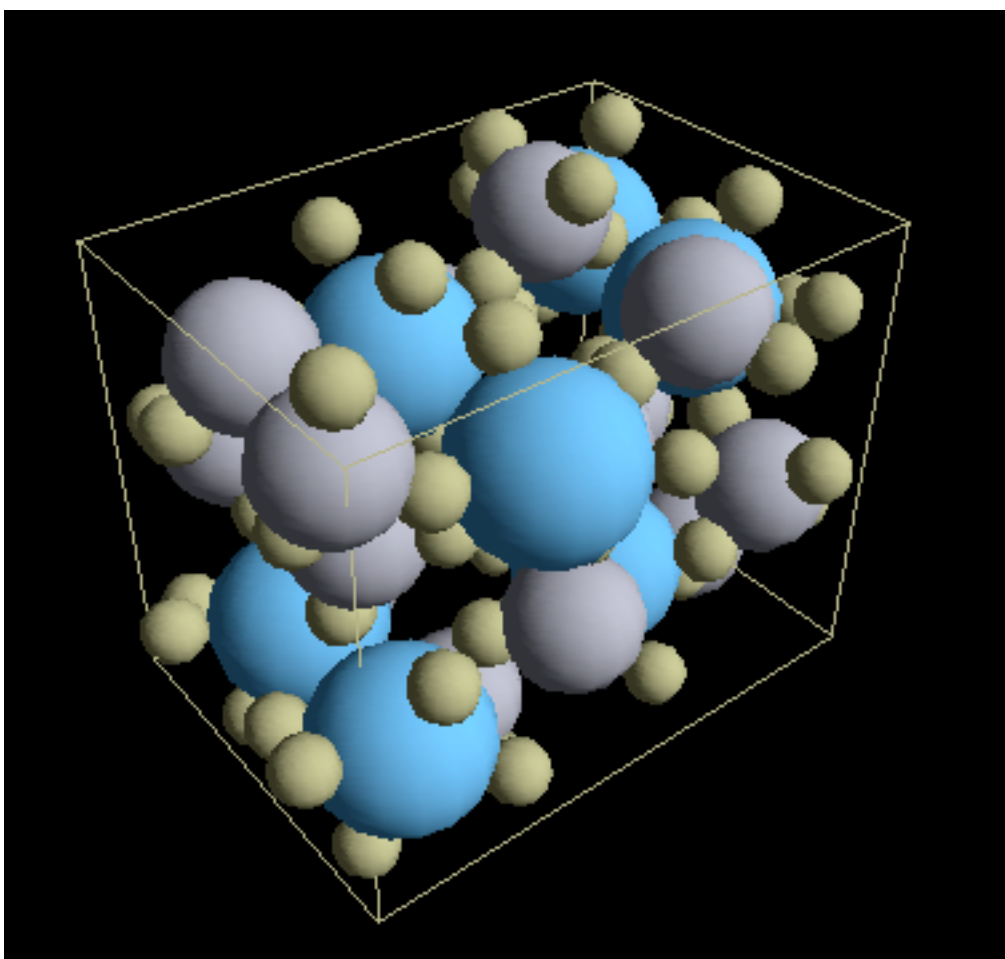


Figure 28. 3D model of La<sub>2</sub>Mo<sub>4</sub>O<sub>15</sub>. The large blue atoms are lanthanum, the medium grey atoms are molybdenum and the small tan atoms are oxygen.

### 3.4.3 Material and Methods

High-pressure x-ray experiments were performed at room temperature at beamline 12.2.2 of the Advanced Light Source (ALS) at Lawrence Berkeley National Laboratory.  $\text{La}_2\text{Mo}_4\text{O}_{15}$  was obtained from Mirek Mączka at the Institute of Low Temperature and Structure Research, Polish Academy of Sciences. The powdered samples were loaded into a symmetric type diamond anvil cell along with a small amount of gold, which was used to determine the pressure inside of the cell.<sup>56, 57</sup> Quasi-hydrostatic conditions were obtained in the cell by filling approximately  $\sim 1/16^{\text{th}}$  of the hole with sample and then adding a mixture of methanol:ethanol:water (16:3:1) for the pressure transmitting medium.<sup>43</sup> For each experiment a spring steel gasket with a hole of  $\sim 100$   $\mu\text{m}$  diameter drilled into a pre-indented area was used to contain the sample. The experiment was performed to a maximum pressure of 21.2 GPa using monochromatic x-rays ( $\lambda = 0.4959$  Å) and a two-dimensional (2D) imaging plate at a distance of 237.36 mm from the sample. The distance of the 2D plate was calculated at ambient conditions using  $\text{LaB}_6$ . The 2D images were transformed into plots of intensity versus  $2\theta$  by radial integration using the FIT2D software package<sup>116</sup>. X-ray diffraction patterns were refined using the Rietveld method with the MAUD program<sup>63</sup>. Atomic coordinates and temperature factors, Table 4, for use in refinement were obtained from Dubois *et al.*<sup>100</sup>. The following parameters were refined: scale factors, background coefficients (third order polynomial), unit-cell parameters, volume fraction of Au and  $\text{La}_2\text{Mo}_4\text{O}_{15}$ , incident intensity and micro-strain. Delft line broadening was used along with an isotropic size-strain model<sup>80</sup>. The crystallite size was refined at the initial pressure and it was then held

constant for the remainder of the experiments. R<sub>w</sub> factors, as reported by MAUD, were typically between 1.2% and 3.7%.

Table 4: Atomic coordinates and temperature factors for La<sub>2</sub>Mo<sub>4</sub>O<sub>15</sub><sup>100</sup>.

Atom	x	y	z	B
La(1)	0.0874	0.3578	0.7724	0.57
La(2)	-0.3464	0.3728	0.7574	0.62
Mo(1)	-0.1365	0.336	0.0915	0.61
Mo(2)	0.3741	0.3446	0.0605	0.54
Mo(3)	-0.0747	0.5902	0.6006	0.66
Mo(4)	0.306	0.5597	0.6199	0.65
O(1)	0.378	0.227	0.155	0.8
O(2)	0.89	0.488	0.711	0.6
O(3)	0.884	0.551	0.44	0.8
O(4)	0.829	0.453	0.183	1.3
O(5)	0.11	0.647	0.607	1
O(6)	0.875	0.366	-0.075	0.7
O(7)	0.807	0.69	0.636	1.2
O(8)	0.41	0.663	0.677	1
O(9)	0.349	0.555	0.46	1.1
O(10)	0.525	0.356	-0.041	1.4
O(11)	0.384	0.446	0.691	0.9
O(12)	0.376	0.452	0.16	1.4
O(13)	0.216	0.351	-0.034	1.2
O(14)	-0.278	0.247	0.121	1.1
O(15)	0.023	0.276	0.147	1.3

#### 3.4.4 Results and Discussion

Representative integrated diffraction images, after background subtraction, for La<sub>2</sub>Mo<sub>4</sub>O<sub>15</sub> are shown in Figure 29. The Miller indices of some of the identified peaks are presented in the plot for 0 GPa. Under compression the structure remains in the

monoclinic crystal system to  $\sim 2.1$  GPa where it then transforms into an unidentified structure. At  $\sim 16.7$  GPa a transition to a glass is observed. This glassy phase remains through the remainder of the experiment to 21.2 GPa. Upon decompression the amorphous phase remains.

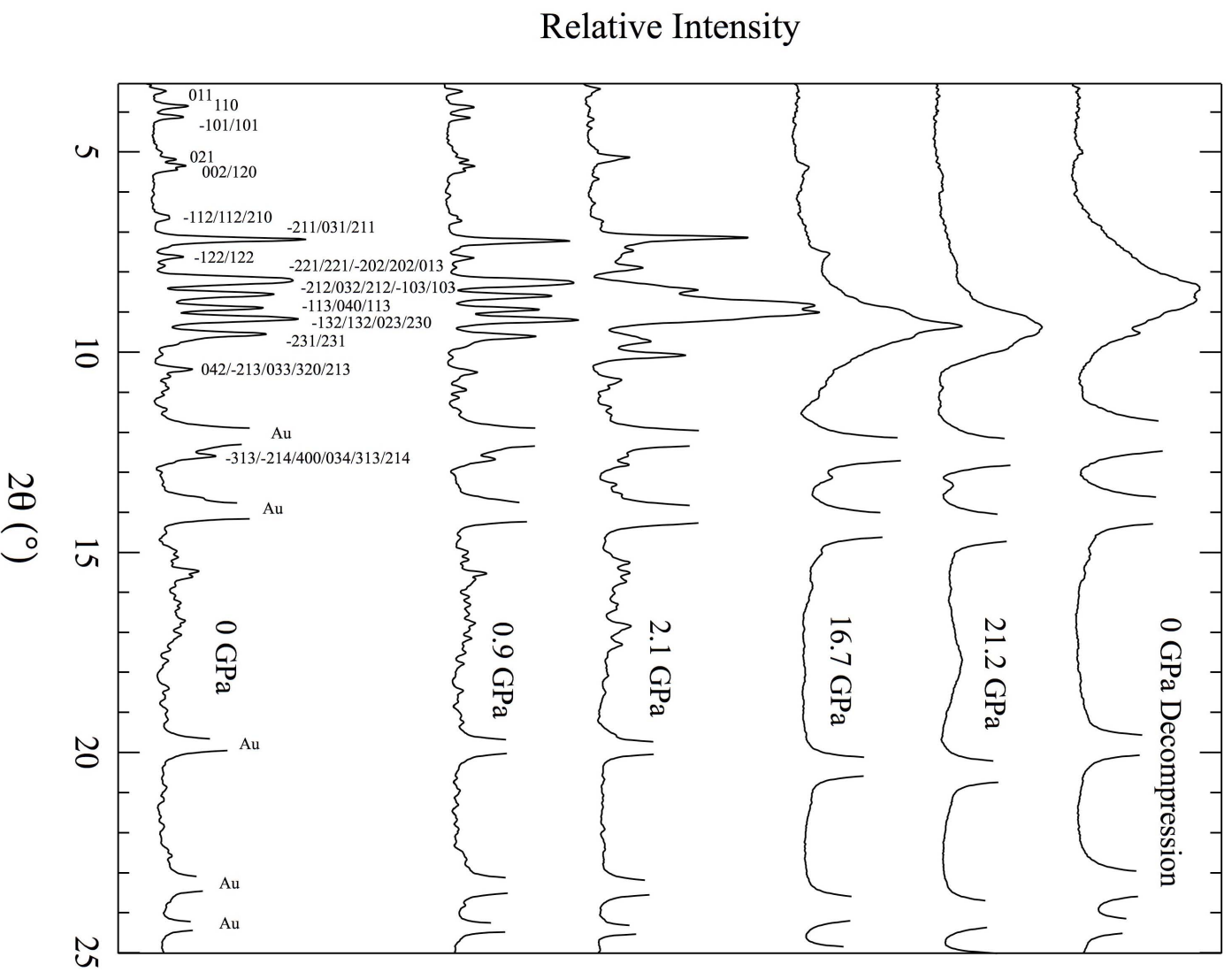


Figure 29.  $\text{La}_2\text{Mo}_4\text{O}_{15}$  XRD. Background subtracted x-ray diffraction data at select pressures for  $\text{La}_2\text{Mo}_4\text{O}_{15}$ . Miller indices are identified for the monoclinic, low pressure, phase at atmospheric pressure. Peaks of gold, truncated, are observed due to their use as pressure markers.

Figure 30 shows a plot of unit cell volume versus pressure. The unit cell volume at 0 GPa was calculated from the experimental data to be  $1226.8 \pm 1.3 \text{ \AA}^3$ . This value is in good agreement with the atmospheric pressure value of  $1228.1 \text{ \AA}^3$  obtained by neutron diffraction <sup>100</sup>. A first order Birch-Murnaghan equation of state <sup>82</sup> was fit to the unit cell volume low-pressure phase for pressures up to 2.1 GPa. The calculation yielded a bulk modulus of  $K = 65.7 \pm 4.7 \text{ GPa}$  with  $K'$  held at 4.

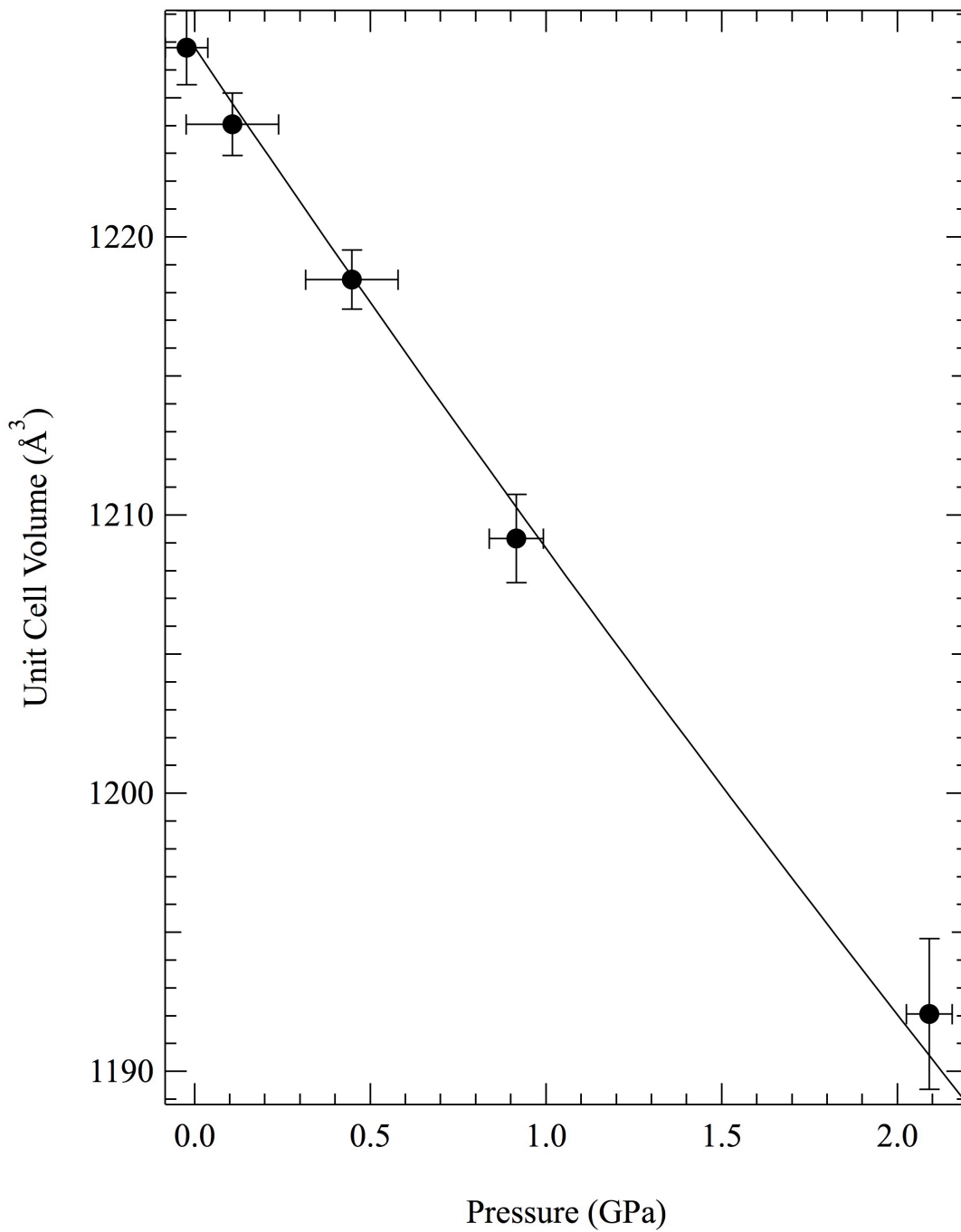


Figure 30.  $\text{La}_2\text{Mo}_4\text{O}_{15}$  V vs P. Plot of volume versus pressure for  $\text{La}_2\text{Mo}_4\text{O}_{15}$ . A Birch-Murnaghan EOS fit for the low-pressure phase is shown with the solid line,  $K = 65.7 \pm 4.7$  GPa.

### 3.4.5 Conclusions

Synchrotron based x-ray diffraction was used to determine the equation of state and phase transitions in  $\text{La}_2\text{Mo}_4\text{O}_{15}$ . Based upon the diffraction pattern it was observed that  $\text{La}_2\text{Mo}_4\text{O}_{15}$  undergoes a phase transformation at  $\sim 2.1$  GPa to an unidentified structure followed by a transition to a glass at  $\sim 16.7$  GPa. This high-pressure amorphous phase continues to the highest pressure of 21.2 GPa and remains upon decompression. The bulk modulus was calculated to be  $K = 65.7 \pm 1.7$  GPa with  $K'$  held at 4.

### 3.5 Sm<sub>2</sub>Mo<sub>4</sub>O<sub>15</sub>

#### 3.5.1 Abstract

Synchrotron based x-ray diffraction was used to determine the equations of state and phase transitions in Sm<sub>2</sub>Mo<sub>4</sub>O<sub>15</sub>. It was observed that Sm<sub>2</sub>Mo<sub>4</sub>O<sub>15</sub> undergoes a phase transformation at ~5.4 GPa. The new high-pressure structure has yet to be identified and remains through the highest compression point of ~28.6 GPa. The new phase remains under decompression through the final data point at ~2.2 GPa (sample chamber failure occurred upon complete decompression). The bulk modulus of the initial phase was calculated to be,  $K = 55.4 \pm 1.4$  GPa and  $K' = 1.7 \pm 1.5$ ; holding  $K' = 4$  yields  $K = 53.4 \pm 0.4$  GPa.

#### 3.5.2 Introduction

The lanthanide molybdate compounds form a large family of materials with interesting physical properties. These properties depend on the crystal structures of these oxides and on the oxidation state of molybdenum <sup>100</sup>. Also of interest is that the RE molybdates can often exhibit polymorphs with various coordination polyhedra <sup>117</sup>. A replacement of RE with other species in RE molybdates can create drastic structural changes. Examples are the RE<sub>2</sub>MoO<sub>6</sub> compounds, which crystallize in monoclinic, cubic, and tetragonal systems depending on the size of RE and preparation conditions <sup>103</sup>.

The family of RE<sub>2</sub>Mo<sub>4</sub>O<sub>15</sub> is known to exhibit different structures with RE = La <sup>100</sup>, Tb <sup>112</sup>, Ho <sup>113</sup> (monoclinic), RE = Ce <sup>114</sup>, Pr <sup>113</sup>, Sm <sup>115</sup> (triclinic). Sm<sub>2</sub>Mo<sub>4</sub>O<sub>15</sub> crystallizes in a triclinic structure of space group *P-1* with cell parameters  $a = 9.4076 \text{ \AA}$ ,

$b = 10.9583 \text{ \AA}$ ,  $c = 11.5234 \text{ \AA}$ ,  $\alpha = 104.225^\circ$ ,  $\beta = 109.603^\circ$ ,  $\gamma = 108.999^\circ$ <sup>115</sup>.  $\text{Sm}_2\text{Mo}_4\text{O}_{15}$  is isomorphous with the  $\text{Eu}_2\text{Mo}_4\text{O}_{15}$  and  $\text{Gd}_2\text{Mo}_4\text{O}_{15}$  analogs<sup>118</sup>, consisting of  $\text{RE}_3\text{Mo}_6\text{O}_{22.5}$  asymmetric unit. The structure consists of one  $[\text{Mo}(6)\text{O}_5]$  trigonal bipyramid, one  $[\text{Mo}(4)\text{O}_6]$  octahedron, four  $[\text{Mo}(1,2,3,5)\text{O}_4]$  tetrahedra, and three  $[\text{R}(1-3)\text{O}_8]$  square-antiprisms<sup>115</sup>. A 3D model of the structure can be observed in Figure 31.

As of the writing of this work only the  $Ln = \text{Dy}$  molybdate has been the subject of high-pressure spectroscopic studies<sup>119</sup>. For  $\text{Dy}_2\text{Mo}_4\text{O}_{15}$ , a pressure-induced structural phase transition was observed at about 2.0 GPa and above 4.7 GPa it exhibited irreversible amorphization. Other previous high-pressure works on  $Ln_2(\text{MoO}_4)_3$  reported observation of pressure-induced amorphization (PIA) in these systems. It has been proposed based on computer simulation studies that negative thermal expansion (NTE) and PIA have common origin in framework structures (tetrahedral bonded networks)<sup>120</sup>.

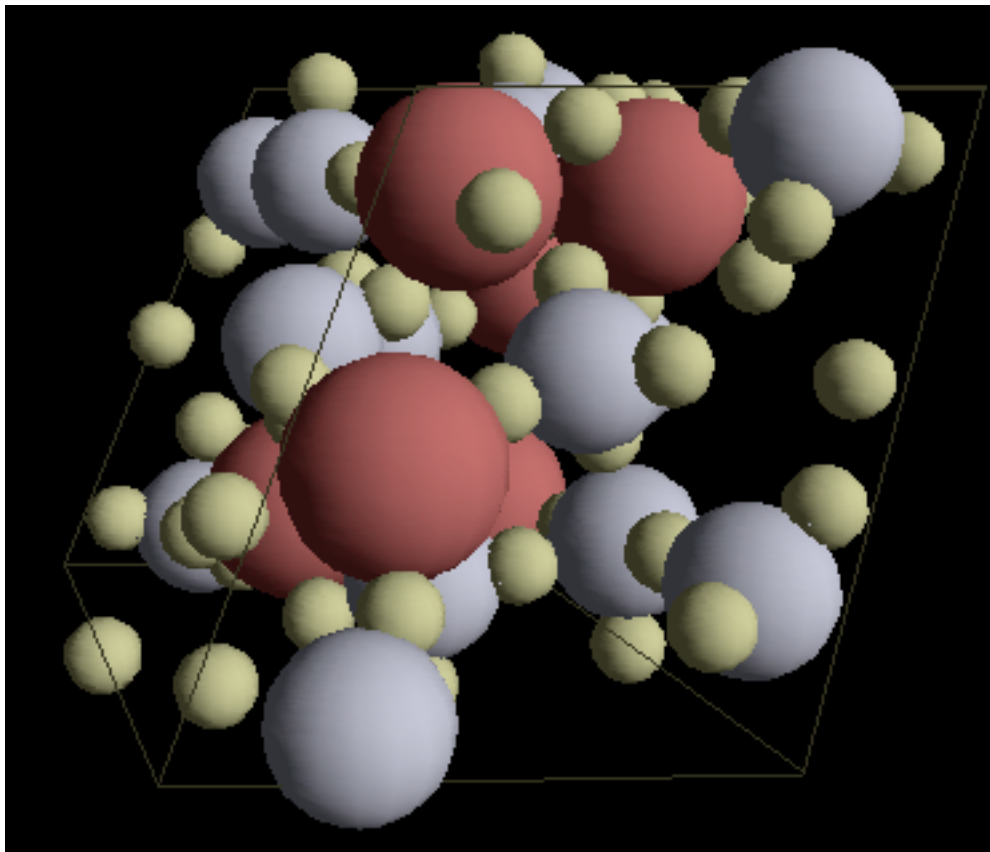


Figure 31. 3D model of  $\text{Sm}_2\text{Mo}_4\text{O}_{15}$ . The large red atoms are samarium, the medium grey atoms are molybdenum and the small tan atoms are oxygen.

### 3.5.3 Material and Methods

High-pressure x-ray experiments for  $\text{Sm}_2\text{Mo}_4\text{O}_{15}$  were performed to 28.6 GPa as described previously for  $\text{La}_2\text{Mo}_4\text{O}_{15}$ .  $\text{Sm}_2\text{Mo}_4\text{O}_{15}$  was obtained from Mirek Mączka at the Institute of Low Temperature and Structure Research, Polish Academy of Sciences. Atomic coordinates and temperature factors, Table 5, for use in refinement were obtained from Naruke *et al*<sup>115</sup>. R<sub>w</sub> factors, as reported by MAUD, were typically ~1.2%.

Table 5: Atomic coordinates and temperature factors for  $\text{Sm}_2\text{Mo}_4\text{O}_{15}$ <sup>115</sup>.

Atom	x	y	z	B
Sm(1)	0.21648	0.05654	0.59053	1.01
Sm(2)	-0.23473	-0.22234	0.82501	0.918
Sm(3)	-0.33574	-0.65935	0.20119	0.888
Mo(1)	0.58459	0.22374	0.48115	1
Mo(2)	0.06708	-0.13266	0.20314	1.03
Mo(3)	-0.08546	-0.31135	0.55248	0.94
Mo(4)	0.91054	0.46702	0.81832	0.87
Mo(5)	-0.26708	-0.98144	0.07939	0.93
Mo(6)	-0.47204	-0.56595	-0.13258	0.93
O(1)	0.4177	0.1646	0.5204	1.8
O(2)	0.3352	0.287	0.7564	1.7
O(3)	0.2888	0.0137	0.785	1.8
O(4)	-0.0347	-0.1599	0.513	1.48
O(5)	0.0309	-0.0671	0.3417	1.6
O(6)	0.658	0.0984	0.4513	2.3
O(7)	0.526	0.2669	0.3389	1.45
O(8)	0.7527	0.2824	0.619	1.8
O(9)	1	0.5	1	2.1
O(10)	0.2195	0.0089	0.199	1.8
O(11)	0.1509	-0.2541	0.2258	1.6
O(12)	-0.1189	-0.2155	0.0515	1.8
O(13)	0.1024	-0.3021	0.6643	1.9
O(14)	-0.2239	-0.3072	0.6224	1.9
O(15)	-0.1074	-0.3793	0.8328	1.7
O(16)	-0.1895	-0.4635	0.4059	1.8
O(17)	-0.0894	-0.5007	0.2	1.8
O(18)	-0.4068	-0.5541	0.0408	1.7
O(19)	-0.3325	-0.8531	0.053	1.6
O(20)	-0.0555	-0.9214	0.116	1.9
O(21)	-0.384	-1.1447	-0.0658	1.26
O(22)	-0.3264	-0.6129	-0.168	2.1
O(23)	-0.4498	-0.4246	-0.1921	1.24

### 3.5.4 Results and Discussion

Representative integrated diffraction images, after background subtraction, for  $\text{Sm}_2\text{Mo}_4\text{O}_{15}$  are shown in Figure 32. The Miller indices of some of the identified peaks are presented in the plot for 0.1 GPa. Under compression the structure remains in the triclinic crystal system to  $\sim 5.4$  GPa where it then transforms into an unidentified structure. This new phase remains through the remainder of the experiment to 28.6 GPa. Upon decompression the new phase remains to at least 2.2 GPa where the sample chamber failed thus eliminating the possibility of seeing the complete decompression dataset.

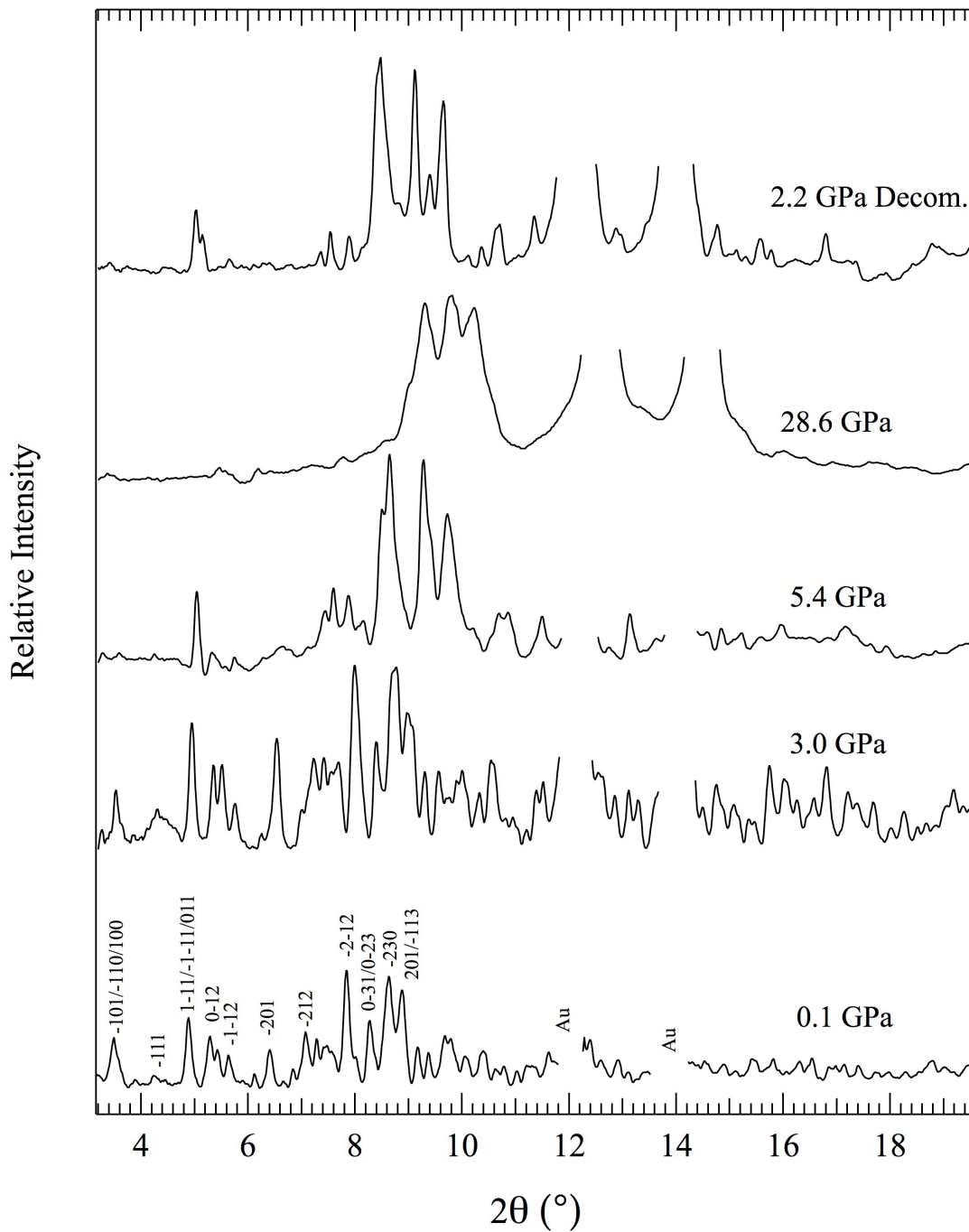


Figure 32.  $\text{Sm}_2\text{Mo}_4\text{O}_{15}$  XRD. Background subtracted x-ray diffraction data at select pressures for  $\text{Sm}_2\text{Mo}_4\text{O}_{15}$ . Miller indices for a few select peaks are identified for the triclinic, low pressure, phase at atmospheric pressure. Peaks of gold, truncated, are observed due to their use as pressure markers.

Figure 33 shows a plot of unit cell volume versus pressure. The unit cell volume at 0.1 GPa was calculated from the experimental data to be  $969.9 \pm 0.1 \text{ \AA}^3$ . This value is in good agreement with the atmospheric pressure value of  $970.5 \text{ \AA}^3$  obtained by single crystal x-ray diffraction<sup>115</sup>. A first order Birch-Murnaghan equation of state<sup>82</sup> was fit to the unit cell volume low-pressure phase for pressures up to 3.0 GPa. The calculation yielded a bulk modulus of,  $K = 55.4 \pm 1.4 \text{ GPa}$  and  $K' = 1.7 \pm 1.5$ ; holding  $K' = 4$  yields  $K = 53.4 \pm 0.4 \text{ GPa}$ .

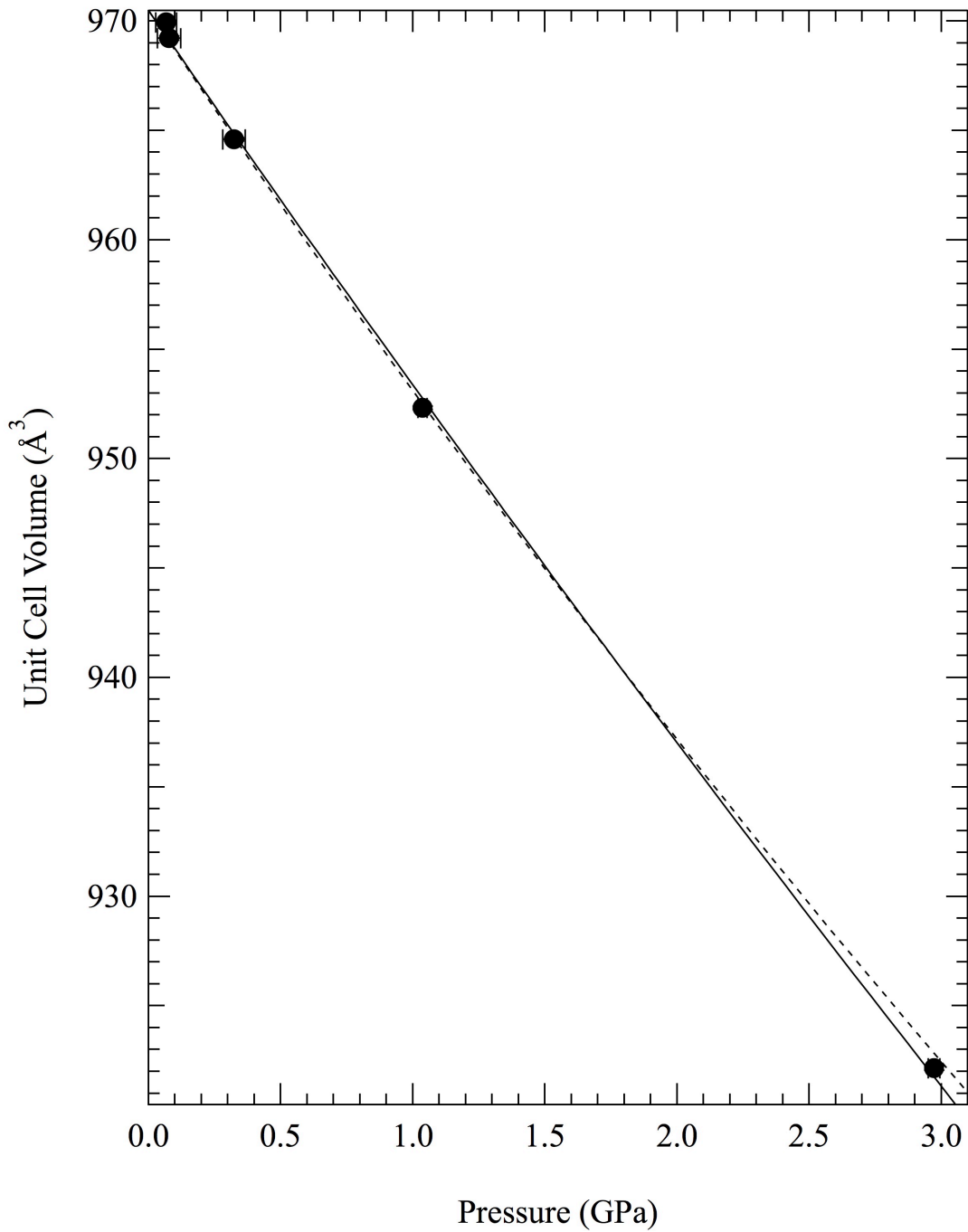


Figure 33.  $\text{Sm}_2\text{Mo}_4\text{O}_{15}$  V vs P. Plot of volume versus pressure for  $\text{Sm}_2\text{Mo}_4\text{O}_{15}$ . A Birch-Murnaghan EOS fit for the low-pressure phase is shown with the solid line,  $K = 55.4 \pm 1.4$  GPa;  $K' = 1.7 \pm 1.5$  and a dotted line,  $K = 53.4 \pm 0.4$  GPa with  $K'$  held at 4.

### 3.5.5 Conclusions

Synchrotron based x-ray diffraction was used to determine the equation of state and phase transitions in  $\text{Sm}_2\text{Mo}_4\text{O}_{15}$ . Based upon the diffraction pattern, it was observed that  $\text{Sm}_2\text{Mo}_4\text{O}_{15}$  undergoes a phase transformation at  $\sim 5.4$  GPa to an unidentified structure. This high-pressure phase continues to the highest pressure of 28.6 GPa and remains to at least 2.2 GPa upon decompression. The bulk modulus was calculated to be  $K = 55.4 \pm 1.4$  GPa and  $K' = 1.7 \pm 1.5$ ; holding  $K' = 4$  yields  $K = 53.4 \pm 0.4$  GPa.

## 3.6 MgNb<sub>2</sub>O<sub>6</sub>

### 3.6.1 Abstract

Synchrotron based x-ray diffraction was used to determine the equations of state and phase transitions in MgNb<sub>2</sub>O<sub>6</sub>. It was observed that MgNb<sub>2</sub>O<sub>6</sub> begins to undergo a phase transformation at ~10.3 GPa and is a mixture of phases until ~10.9 GPa. The new high-pressure structure has yet to be identified. The transition is reversible upon complete decompression from ~35 GPa. The bulk modulus of the initial phase was calculated to be,  $K = 155.9 \pm 1.2$  GPa with  $K'$  held at 4.

### 3.6.2 Introduction

Niobium mixed oxides have generated recent interest for further study<sup>121-130</sup>. The discovery of superconducting oxides, such as Li<sub>x</sub>NbO<sub>2</sub><sup>131</sup>. MgNb<sub>2</sub>O<sub>6</sub> has attracted interest with focus on its use a precursor for the synthesis of microwave dielectric material Ba(Mg<sub>1/3</sub>Nb<sub>2/3</sub>)O<sub>3</sub><sup>121</sup>, perovskite Pb(Mg<sub>1/3</sub>Nb<sub>2/3</sub>)O<sub>3</sub>, a potential candidate for multilayer ceramic capacitor, transducer, electrostrictor and actuator applications<sup>124-127</sup>. It is also a suitable reference material for investigating the defects induced in LiNbO<sub>3</sub> substrate for waveguide fabrication<sup>121, 132</sup>.

The crystal structure of MgNb<sub>2</sub>O<sub>6</sub> is of a columbite-type phase, orthorhombic, space group *Pbcn*, with unit cell parameters  $a=14.1875$  Å,  $b=5.7001$  Å,  $c=5.0331$  Å<sup>121</sup>. The columbite structures have general formula AB<sub>2</sub>O<sub>6</sub> (A being Fe, Mn, Mg and B representing Nb)<sup>133, 134</sup>. The structure contains chains of NbO<sub>6</sub> octahedra sharing edges along the c-axis, which are arranged in double layers through common corners. The

double layers, parallel to the bc-plane, are connected via  $\text{MgO}_6$  octahedra sharing corners

<sup>121</sup>. A 3D model of the structure can be observed in Figure 34.

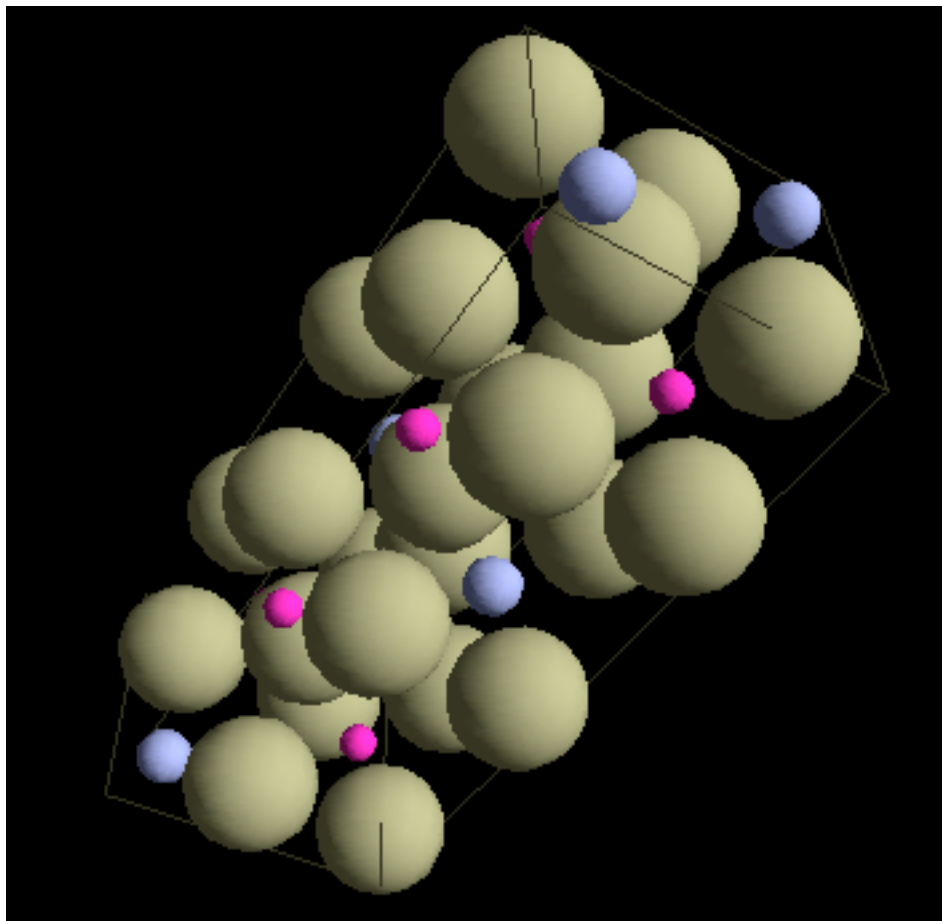


Figure 34. 3D model of  $\text{MgNb}_2\text{O}_6$ . The large tan atoms are oxygen, the medium blue atoms are magnesium and the small pink atoms are niobium.

### 3.6.3 Material and Methods

To obtain data on the material at atmospheric pressure conventional x-ray diffraction spectra were collected on a Rigaku Miniflex diffractometer (30 kV and 15 mW) with a variable slit, in  $\theta$ - $2\theta$  Bragg-Brentano geometry, using Cu  $K_{\alpha}$  radiation and a scintillation detector in the  $2\theta$  range between  $10^{\circ}$  and  $65^{\circ}$ . The powdered sample was placed upon a silicon zero background plate and scanned at a rate of 2 seconds per  $0.05^{\circ}$ .

High-pressure x-ray experiments were performed to 35.2 GPa for  $\text{MgNb}_2\text{O}_6$  as described previously for  $\text{Sm}_2\text{Mo}_4\text{O}_{15}$  and  $\text{La}_2\text{Mo}_4\text{O}_{15}$ .  $\text{MgNb}_2\text{O}_6$  was purchased from Alfa Aesar (stock # 39373, lot # F25S054). Atomic coordinates and temperature factors, Table 6, for use in refinement were obtained from Santos *et al.*<sup>135</sup>. R<sub>w</sub> factors, as reported by MAUD, were typically between ~1.1%.

Raman spectra were recorded in back-scattering geometry using a single monochromator (Spectrapro 500i) with a liquid nitrogen cooled CCD (Spec-10). The 514.5 nm line from an argon ion laser with an incident power of about 20 mW was used to excite the sample. The Rayleigh line was blocked using a holographic edge filter. The  $\text{MgNb}_2\text{O}_6$  was ground to a fine powder and loaded into a Mao–Bell type diamond anvil cell, with a culet size of 300  $\mu\text{m}$ . A spring steel gasket with a sample chamber diameter of ~100  $\mu\text{m}$  was used to contain the sample. Ruby powder was loaded along with the sample to measure the pressure using the ruby fluorescence technique. Methanol:ethanol:water (16:3:1) was used as a pressure transmitting medium.

Table 6: Atomic coordinates and temperature factors for  $\text{MgNb}_2\text{O}_6$  <sup>135</sup>.

Atom	x	y	z	B
$\text{Mg}^{2+}$	0	0.1671	0.25	0.408
$\text{Nb}^{5+}$	0.16	0.318	0.7547	0.408
$\text{O}^{2-}(1)$	0.091	0.394	0.439	0.408
$\text{O}^{2-}(2)$	0.0749	0.1124	0.904	0.408
$\text{O}^{2-}(3)$	0.254	0.1219	0.5833	0.408

#### 3.6.4 Results and Discussion

Figure 35 shows a comparison between a calculated XRD spectrum from PowderCell for  $\text{MgNb}_2\text{O}_6$  and the data collected on a Rigaku Miniflex bench-top XRD system. The reflections match well so the experiment was continued using high-pressure techniques.

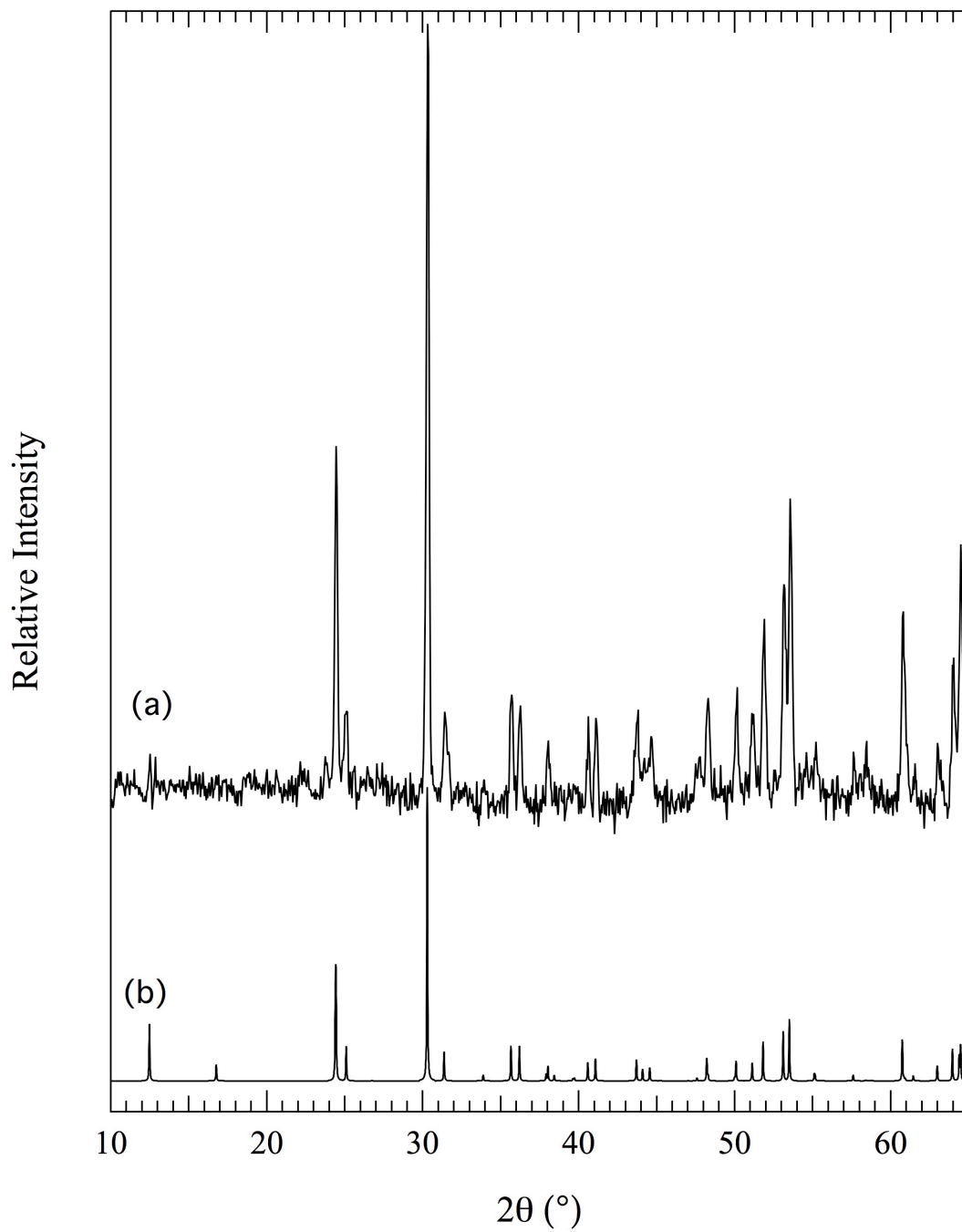


Figure 35. MgNb<sub>2</sub>O<sub>6</sub> bench top XRD. (a) X-ray diffraction, collected from a Rigaku Miniflex using a copper anode, of MgNb<sub>2</sub>O<sub>6</sub> at atmospheric pressure. (b) Calculated spectrum of MgNb<sub>2</sub>O<sub>6</sub> from PowderCell.

Representative integrated diffraction images, after background subtraction, for  $\text{MgNb}_2\text{O}_6$  are shown in Figure 36. The Miller indices of some of the identified peaks are presented in the plot for 0.07 GPa. Under compression the structure remains in the orthorhombic crystal system to  $\sim 10.3$  GPa where it begins to transform into an unidentified structure. By 10.9 GPa the phase transition is complete. The high-pressure phase remains through the remainder of the experiment to 35.2 GPa. Upon complete decompression the original structure returns. However, the new high-pressure phase is still present at 7.2 GPa.

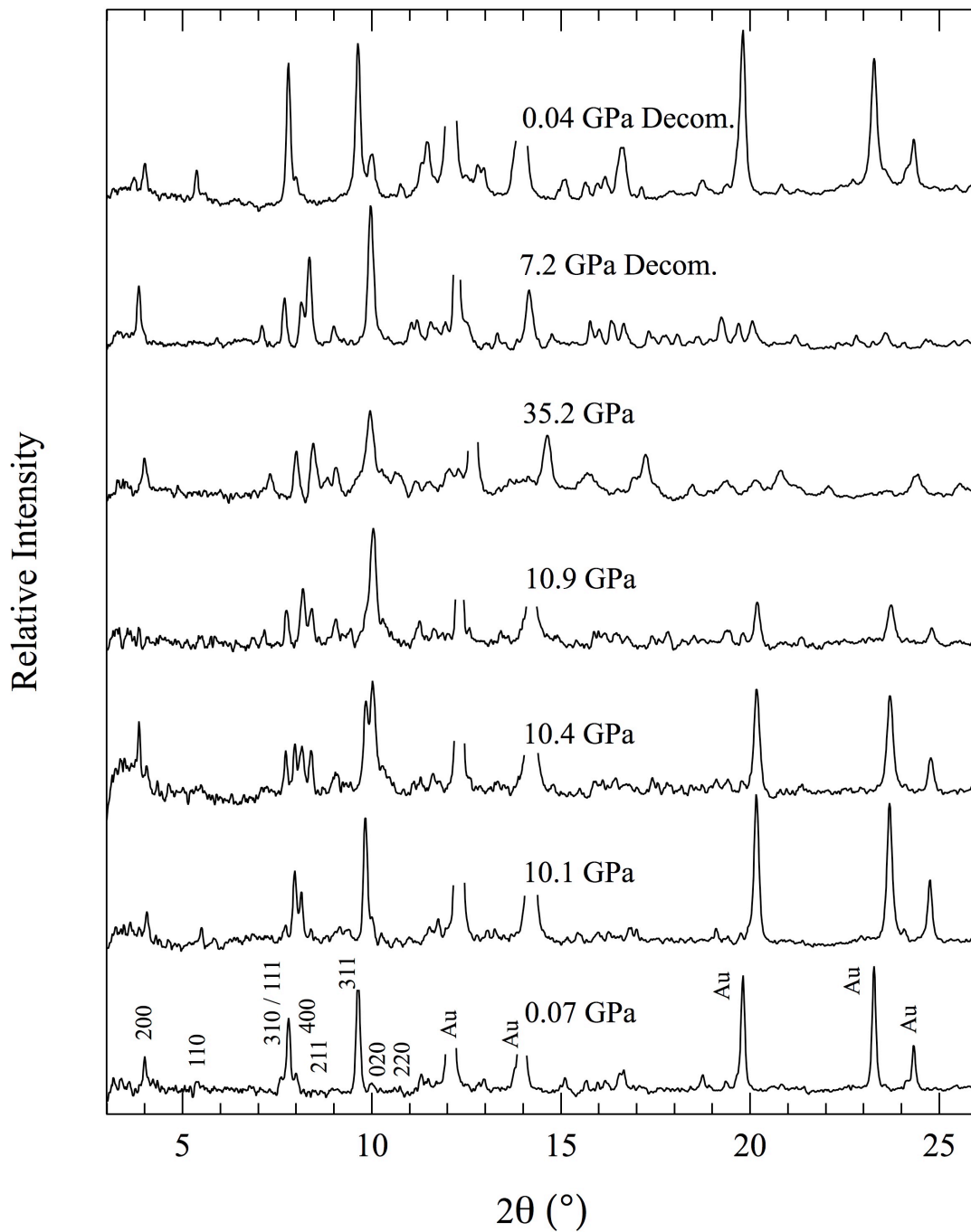


Figure 36. MgNb<sub>2</sub>O<sub>6</sub> XRD. Background subtracted x-ray diffraction data, collected at beamline 12.2.2 at ALS, at select pressures for MgNb<sub>2</sub>O<sub>6</sub>. Miller indices are identified for the orthorhombic, low pressure, phase at atmospheric pressure. Peaks of gold, truncated, are observed due to their use as pressure markers.

Figure 37 shows a plot of unit cell volume versus pressure. The unit cell volume at 0.07 GPa was calculated from the experimental data to be  $406.4 \pm 0.3 \text{ \AA}^3$ . This value is in good agreement with the atmospheric pressure value of  $407.03 \text{ \AA}^3$  obtained by neutron diffraction <sup>121</sup>. A first order Birch-Murnaghan equation of state <sup>82</sup> was fit to the unit cell volume low-pressure phase for pressures up to 10.3 GPa. The calculation yielded a bulk modulus of  $K = 155.9 \pm 1.2 \text{ GPa}$  with  $K'$  held at 4.

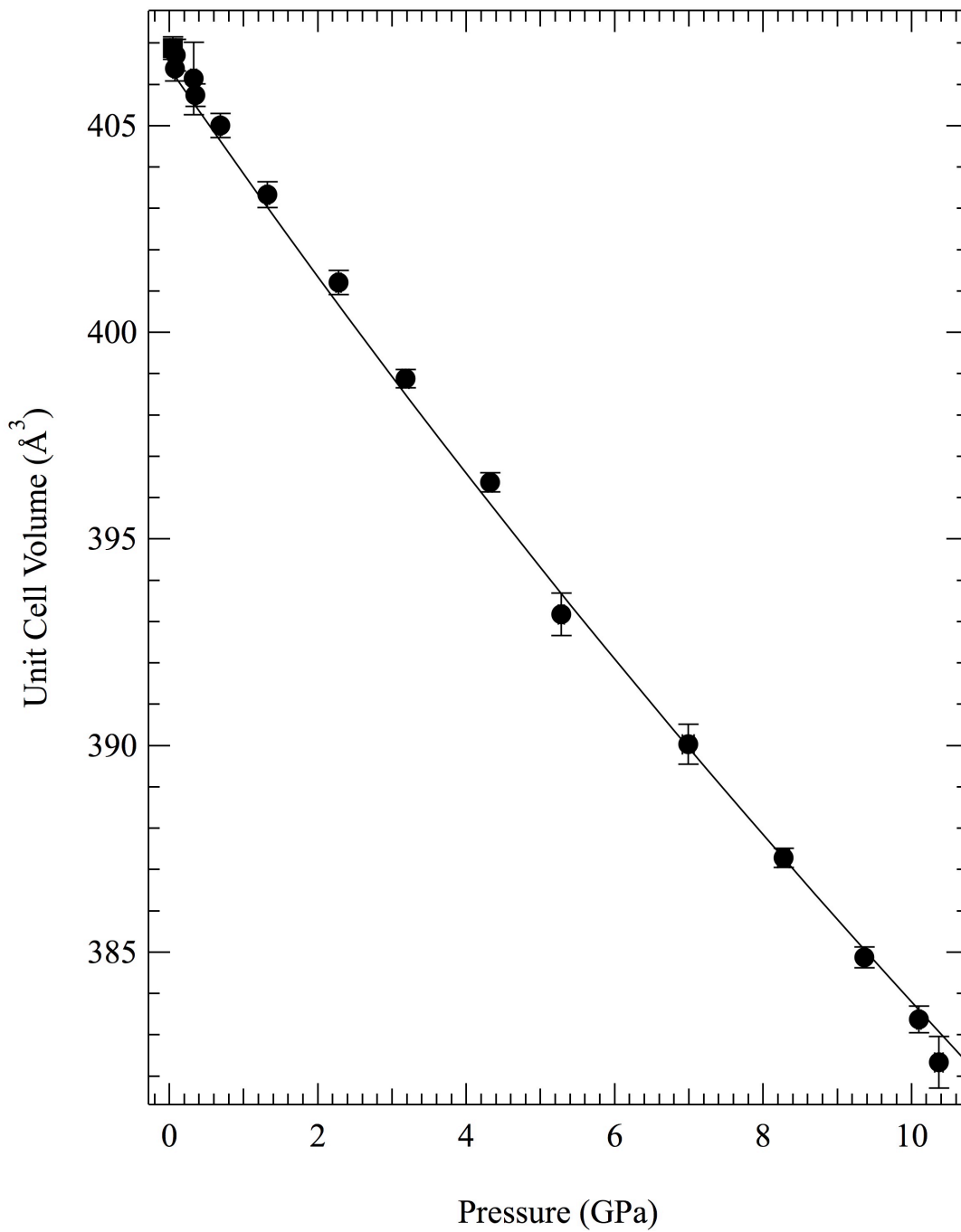


Figure 37. MgNb<sub>2</sub>O<sub>6</sub> V vs P. Plot of volume versus pressure for MgNb<sub>2</sub>O<sub>6</sub> (circles for compression, squares for decompression). A Birch-Murnaghan EOS fit for the low-pressure phase is shown with the solid line,  $K = 155.9 \pm 1.2$  GPa.

Raman spectra for select pressures can be seen in Figure 38. The Raman modes observed at atmospheric pressure match those reported by Santos *et al.*<sup>135</sup>. At 11 GPa it is observed that new Raman modes are present at 316, 504, 659, 706, and 729  $\text{cm}^{-1}$  as well as a loss of modes at 296, 528, 567, and 938  $\text{cm}^{-1}$ . These new modes are evidence that a phase change has occurred and correspond to the same change observed in the XRD data presented above. The new phase persists until the highest pressure achieved in the Raman portion of this study, ~24 GPa. Upon decompression the original, low-pressure, phase returns.

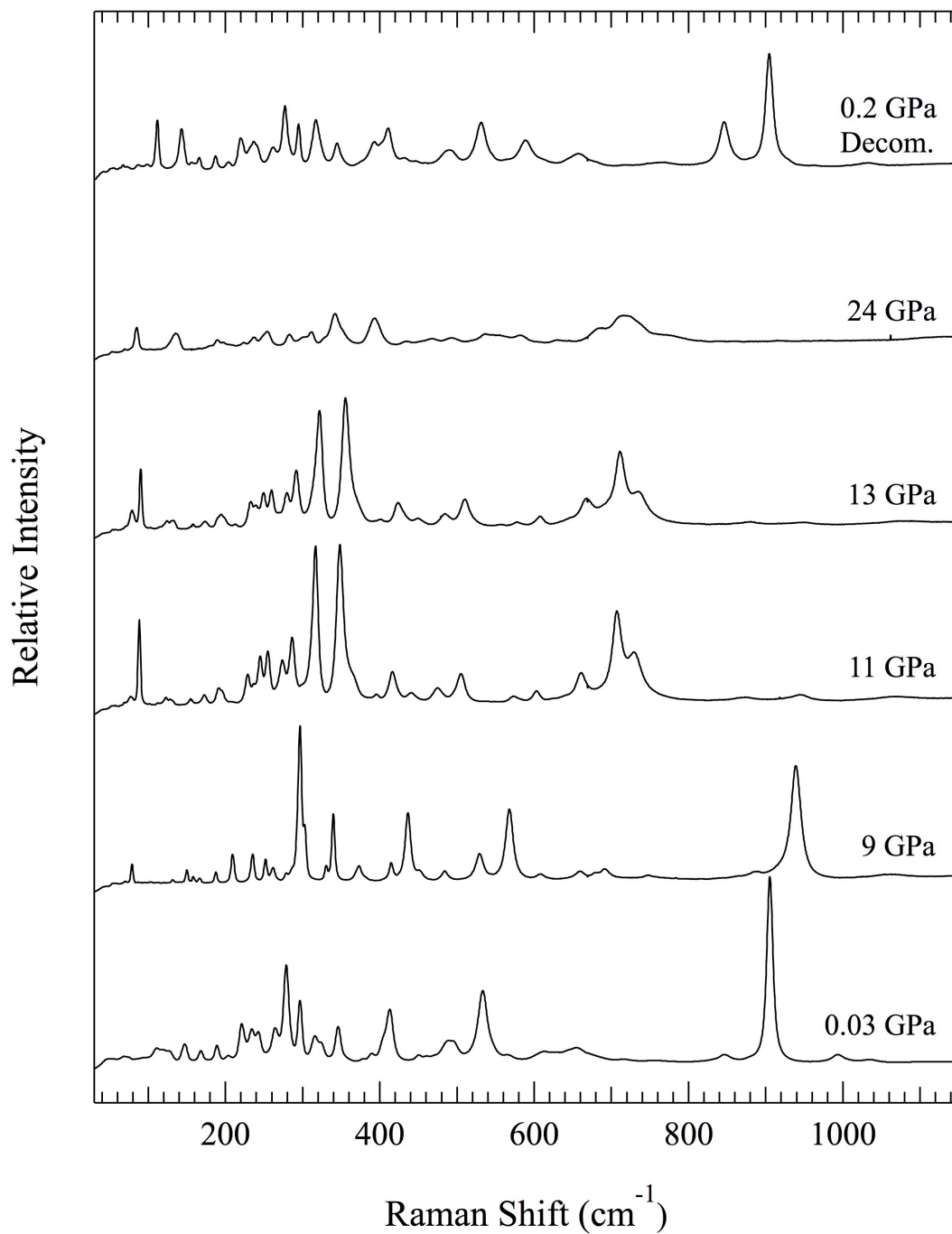


Figure 38. Raman shift of MgNb<sub>2</sub>O<sub>6</sub> at select pressures. A phase transition is evident by the change in the spectra between 9 GPa and 11 GPa.

### 3.6.5 Conclusions

Synchrotron based x-ray diffraction was used to determine the equation of state and phase transitions in  $\text{MgNb}_2\text{O}_6$ . Based upon the diffraction pattern, it was observed that  $\text{MgNb}_2\text{O}_6$  undergoes a phase transformation at  $\sim 10.3$  GPa to an unidentified structure. This new high-pressure phase is evident in both XRD and Raman data and continues to the highest pressure of 35.2 GPa. Under decompression the phase change is reversible but still evident at  $\sim 7.2$  GPa. The bulk modulus was calculated to be  $K = 155.9 \pm 1.2$  GPa with  $K'$  held at 4.

### 3.7 KNbW<sub>2</sub>O<sub>9</sub>

#### 3.7.1 Abstract

Synchrotron based x-ray diffraction was used to determine the equations of state and phase transitions in KNbW<sub>2</sub>O<sub>9</sub>. It was observed that KNbW<sub>2</sub>O<sub>9</sub> does not undergo a phase transformation up ~35 GPa. The bulk modulus was calculated to be,  $K = 62.9 \pm 0.3$  GPa with  $K'$  held at 4.

#### 3.7.2 Introduction

Tungsten bronzes are of interest due to their complex crystal chemistry and their interesting properties, such as ferroelectricity. KNbW<sub>2</sub>O<sub>9</sub> belongs to the novel class of valence-balanced compounds crystallizing in the structure of hexagonal tungsten bronze<sup>136</sup>.  $A_xB_yW_{1-y}O_3$  compounds (where A = alkali metal and B = Nb, Ta, Zr, Sc, Bi, etc.) are valence-balanced dielectrics whereas  $A_xWO_3$  bronzes exhibit metallic type conductivity<sup>137</sup>. The  $A_xWO_3$  non-stoichiometric compounds have been the most studied, where A is an electropositive element or group. These can be divided into four distinct structural types: the perovskite, tetragonal, hexagonal, and intergrowth types<sup>137</sup>. The same structural types are formed when tungsten atoms are substituted partially by atoms with lower valence. However, this partial substitution modifies significantly the physical properties of bronzes. In contrast to perovskites and tetragonal tungsten bronzes, which have been extensively studied, very few data have been published on the valence-balanced hexagonal tungsten bronzes. KNbW<sub>2</sub>O<sub>9</sub> crystallizes in the orthorhombic, space group *Cmm2* with  $a = 21.9554 \text{ \AA}$ ,  $b = 12.60725 \text{ \AA}$  and  $c = 3.87748(3) \text{ \AA}$ <sup>12</sup>. A 3D model

of the structure can be observed in Figure 39.  $\text{KNbW}_2\text{O}_9$  has been studied previously, under atmospheric pressure conditions, by means of dielectric, electron microscopy and x-ray diffraction <sup>138-143</sup>. These studies observed a number of phase transitions and may display ferroelectric or antiferroelectric properties as well as a new high-temperature phase that may be of space group  $P6322$ .

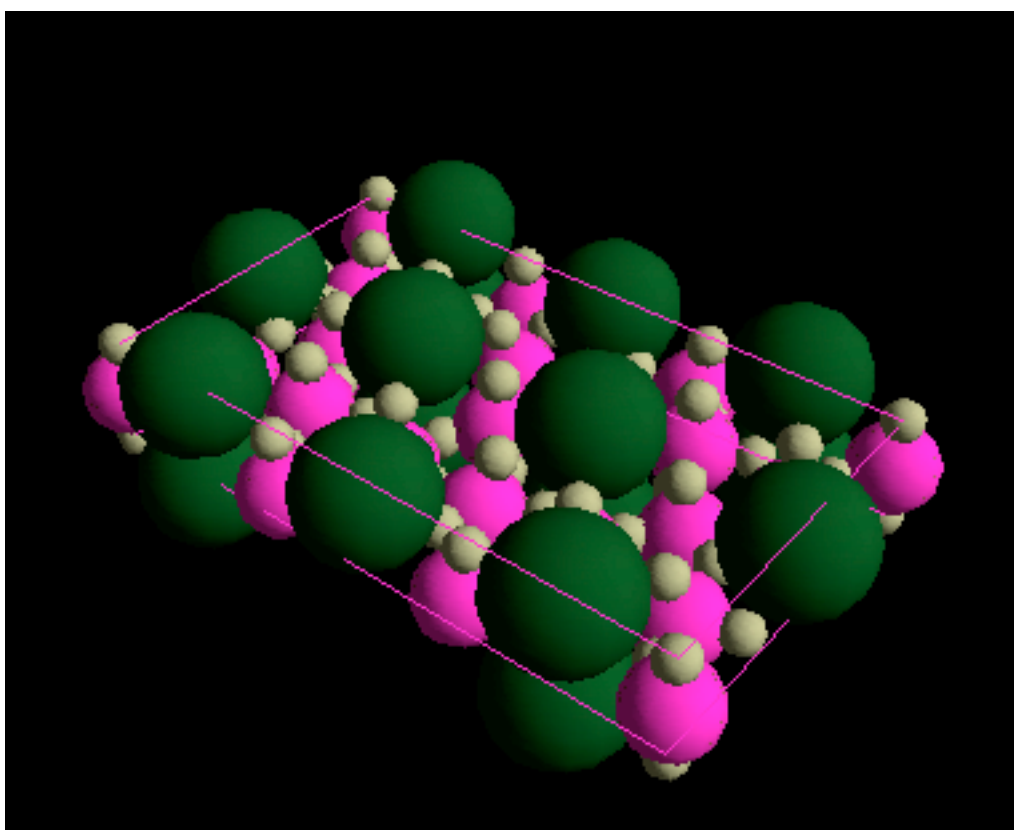


Figure 39. 3D model of  $\text{KNbW}_2\text{O}_9$ . The large green atoms are potassium, the medium purple atoms are niobium/tungsten and the small tan atoms are oxygen.

### 3.7.3 Material and Methods

High-pressure x-ray experiments were performed for X to a pressure of 35.7 GPa as described previously for  $\text{Sm}_2\text{Mo}_4\text{O}_{15}$ ,  $\text{La}_2\text{Mo}_4\text{O}_{15}$ , and  $\text{MgNb}_2\text{O}_6$  but with using monochromatic x-rays ( $\lambda = 0.6199 \text{ \AA}$ ).  $\text{KNbW}_2\text{O}_9$  was obtained from Mirek Mączka at the Institute of Low Temperature and Structure Research, Polish Academy of Sciences. Atomic coordinates and temperature factors, Table 7, for use in refinement were obtained from Chang *et al.*<sup>12</sup>. R<sub>w</sub> factors, as reported by MAUD, were typically between 1.9% and 5.1%.

Table 7: Atomic coordinates and temperature factors for  $\text{KNbW}_2\text{O}_9$ <sup>12</sup>.

Atom	x	y	z	B
K(1)	0.1666	0	0.02	2.1
K(2)	0	0.5	0.134	2.6
W(1)	0.3333	0	0.63	1.25
W(2)	0	0	0.5	1.8
W(3)	0.08303	0.2511	0.614	1.45
W(4)	0.25	0.25	0.502	1.14
Nb(1)	0.3333	0	0.63	1.25
Nb(2)	0	0	0.5	1.8
Nb(3)	0.08303	0.2511	0.614	1.45
Nb(4)	0.25	0.25	0.502	1.14
O(1)	0.4153	0.096	0.412	2
O(2)	0.323	0	0.11	2
O(3)	0.274	0.11	0.57	2
O(4)	0	0	0.01	2
O(5)	0.061	0.105	0.575	2
O(6)	0.0938	0.2099	0.106	2
O(7)	0	0.281	0.515	2
O(8)	0.168	0.1816	0.512	2
O(9)	0.25	0.25	0.016	2

#### 3.7.4 Results and Discussion

Representative integrated diffraction images, after background subtraction, for  $\text{KNbW}_2\text{O}_9$  are shown in Figure 40. The Miller indices of some of the identified peaks are presented in the plot for 0.0 GPa. Under compression the structure remains in the orthorhombic crystal system to  $\sim 35.7$  GPa. Upon decompression no new behavior is observed.

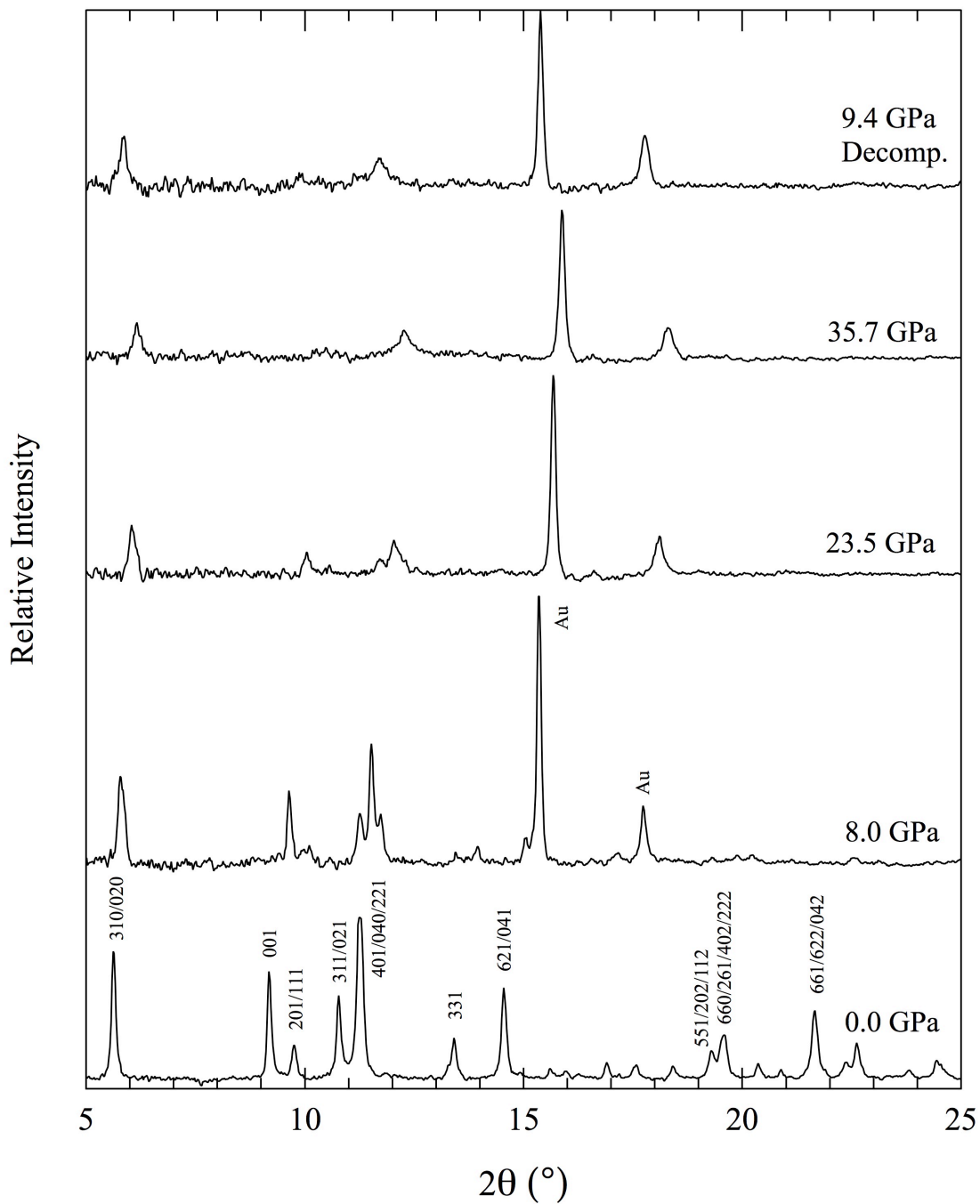


Figure 40. KNbW<sub>2</sub>O<sub>9</sub> XRD. Background subtracted x-ray diffraction data at select pressures for KNbW<sub>2</sub>O<sub>9</sub>. Miller indices are identified for a select few peaks for the orthorhombic phase at atmospheric pressure. Peaks of gold are observed due to their use as pressure markers.

Figure 41 shows, at the atmospheric conditions, the 2D plot of 100 slices of background-subtracted data as well as the calculated Rietveld fit for each data set.

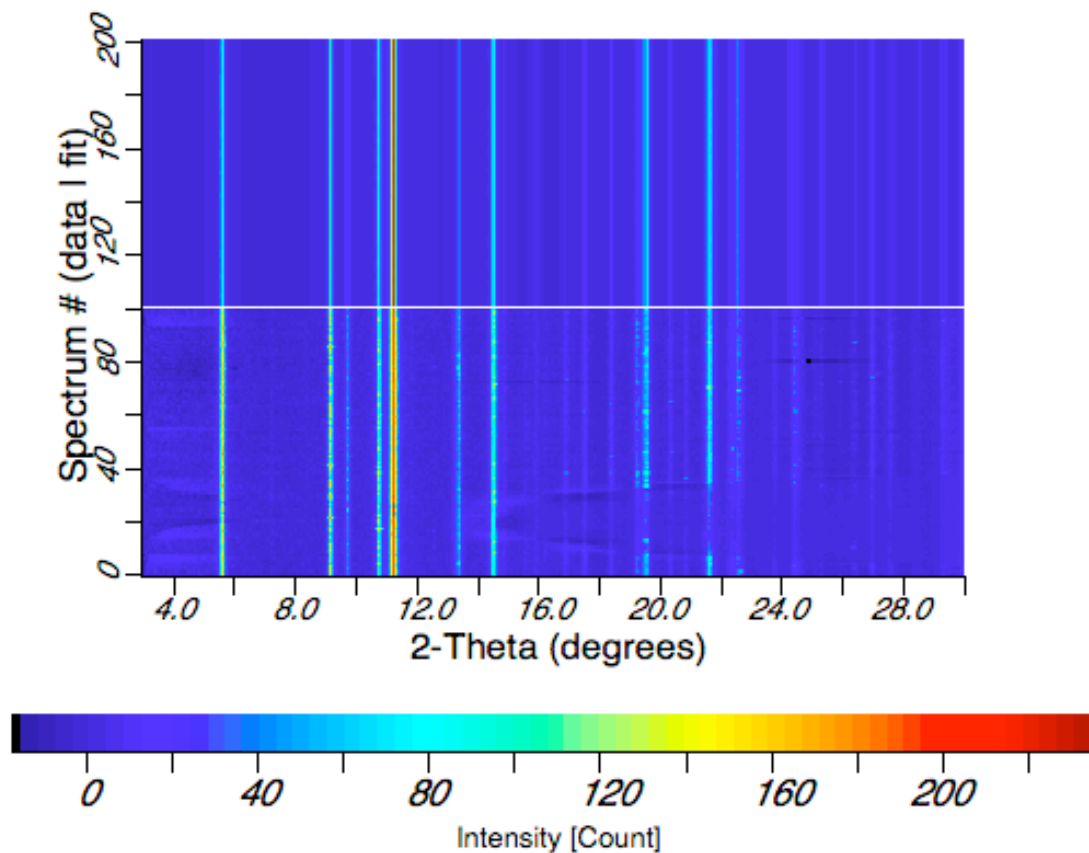


Figure 41. 2D plot of calculated and experimental data for KNbW<sub>2</sub>O<sub>9</sub>.

Figure 42 shows a plot of unit cell volume versus pressure. The unit cell volume at atmospheric pressure was calculated from the experimental data to be  $1070.9 \pm 0.1 \text{ \AA}^3$ . This value is in good agreement with the atmospheric pressure value of  $1073.28 \text{ \AA}^3$

obtained by x-ray powder diffraction <sup>12</sup>. A first order Birch-Murnaghan equation of state <sup>82</sup> was fit to the unit cell volume. The calculation yielded a bulk modulus of,  $K = 62.9 \pm 0.3$  GPa with  $K'$  held at 4.

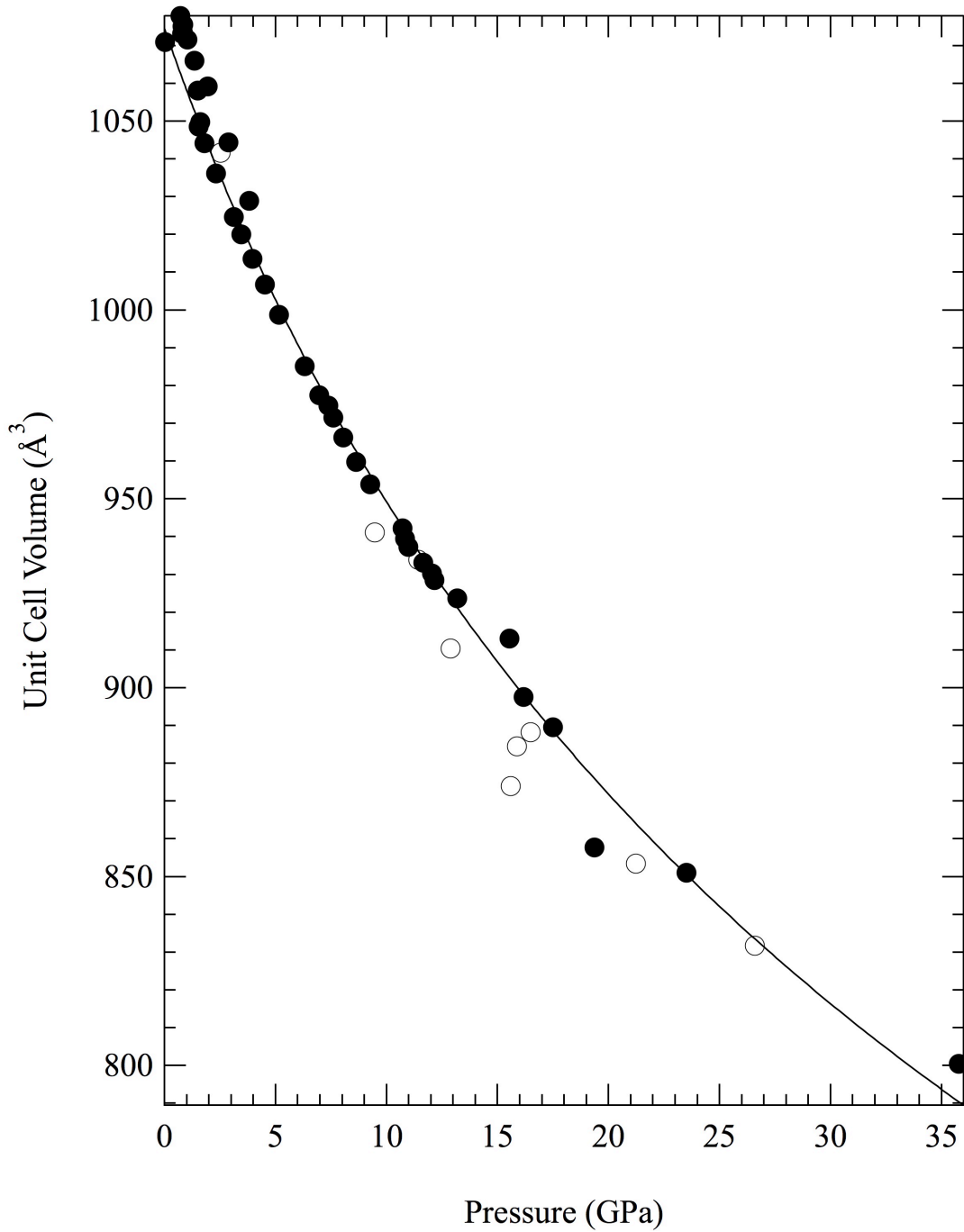


Figure 42.  $\text{KNbW}_2\text{O}_9$  V vs P. Plot of volume versus pressure for  $\text{KNbW}_2\text{O}_9$ . Closed circles are for compression and open circles are decompression. A Birch-Murnaghan EOS fit for the orthorhombic phase is shown with the solid line,  $K = 62.9 \pm 0.3$  GPa with  $K'$  held at 4.

### 3.7.5 Conclusions

Synchrotron based x-ray diffraction was used to determine the equation of state and phase transitions in  $\text{KNbW}_2\text{O}_9$ . Based upon the diffraction pattern, it was observed that  $\text{KNbW}_2\text{O}_9$  does undergo a phase transition up to  $\sim 35.7$  GPa. The bulk modulus was calculated to be  $K = 62.9 \pm 0.3$  GPa with  $K'$  held at 4.

## CHAPTER 4

### CONCLUSION

#### 4.1 Conclusion

Seven materials of the molybdate, tungstate, and niobate groups were studied under static high-pressure conditions using synchrotron-based x-ray diffraction.

$\text{Bi}_2\text{MoO}_6$  exhibited a phase transition at  $\sim 6.8$  GPa that was observed by a stiffening of its bulk modulus from 51 GPa, for the low-pressure phase, to 141.5 GPa for the high-pressure phase. This partially confirms previous work using Raman spectroscopy that observed transitions at 2.8 GPa and 7.0 GPa<sup>31</sup>. It continues to index well to its original orthorhombic  $Pca2_1$  structure and is reversible from  $\sim 47$  GPa. A theoretical atmospheric unit cell volume for the high-pressure phase was calculated to be  $463.8 \text{ \AA}^3$ , which is lower than the value of  $481.3 \text{ \AA}^3$  for the initial low-pressure phase. The work was performed in a Mao-Bell type diamond anvil cell at beamline X17C at the National Synchrotron Light Source (NSLS). This work has been published by Scott *et al.*

144

$\text{Bi}_2\text{W}_2\text{O}_9$  exhibited a phase transition at  $\sim 11$  GPa that was observed by a change in the x-ray diffraction pattern. This in contrast to previous work using Raman spectroscopy that observed transitions at 2.8 GPa and 4.8 GPa<sup>33</sup>. The new phase is yet to be identified and returns, upon decompression from 49.3 GPa, to the original orthorhombic  $Pna2_1$  structure. The bulk modulus of the low-pressure phase was

calculated to be 76.6 GPa. The work was performed in a Mao-Bell type diamond anvil cell at beamline X17C at the National Synchrotron Light Source (NSLS).

$\text{Bi}_2\text{WO}_6$  exhibited a phase transition between  $\sim 4.8$  GPa and 8.3 GPa that was observed by a stiffening of its bulk modulus from 52.2 GPa, for the low-pressure phase, to 121.8 GPa for the high-pressure phase. This partially confirms previous work using Raman spectroscopy that observed transitions at 3.4 GPa and 6.2 GPa <sup>32</sup>. It continues to index well to its original orthorhombic  $Pca2_1$  structure and is reversible from  $\sim 48.5$  GPa. A theoretical atmospheric unit cell volume for the high-pressure phase was calculated to be  $459 \text{ \AA}^3$ , which is lower than the value of  $487.6 \text{ \AA}^3$  for the initial low-pressure phase. The work was performed in a Mao-Bell type diamond anvil cell at beamline X17C at the National Synchrotron Light Source (NSLS).

$\text{La}_2\text{Mo}_4\text{O}_{15}$  exhibited two phase transitions one at 2 GPa and another at 17 GPa. The bulk modulus of the low-pressure, monoclinic  $P21/n$ , phase was calculated to be 65.7 GPa. The transition at 2 GPa was observed as a change in the x-ray diffraction pattern and the new intermediate phase has yet to be identified. The transition at 17 GPa was to a glassy, pressure-induced amorphization, state. In a recent high-pressure Raman experiment it was observed that  $\text{Dy}_2\text{Mo}_4\text{O}_{15}$  has similar phase changes at 2 GPa and 4.3 GPa <sup>119</sup>. Upon decompression from 21 GPa the glassy phase remains. The work was performed in a symmetric type diamond anvil cell at beamline 12.2.2 at the Advanced Light Source (ALS).

$\text{Sm}_2\text{Mo}_4\text{O}_{15}$  exhibited a phase transition at 5.4 GPa. The bulk modulus of the low-pressure, triclinic  $P-1$ , phase was calculated to be 53.4 GPa. This transition was observed

as a change in the x-ray diffraction pattern and has yet to be identified. The highest pressure achieved in the experiment was 28.6 GPa and no reversibility data is available due to a gasket failure. No previous high-pressure work is known on this or any analogue to the triclinic variation of this series of materials. The work was performed in a symmetric type diamond anvil cell at beamline 12.2.2 at the Advanced Light Source (ALS).

MgNb<sub>2</sub>O<sub>6</sub> exhibited a phase transition at 10.3 GPa. The bulk modulus of the low-pressure, orthorhombic *Pbcn*, phase was calculated to be 155.9 GPa. This transition was observed in both x-ray diffraction and Raman spectroscopy. The highest pressure achieved in the experiment was 35 GPa and the new, yet to be identified, phase is reversible upon decompression. The work was performed in a symmetric type diamond anvil cell at beamline 12.2.2 at the Advanced Light Source (ALS) and in a Mao-Bell type diamond anvil cell at the UMKC Raman spectroscopy laboratory. The atmospheric work was performed in the Geosciences laboratory at UMKC.

KNbW<sub>2</sub>O<sub>9</sub> exhibited no signs of a phase change up to a pressure of 35 GPa. This is in contrast to previous work that suggest a slight phase change at 1.4 GPa<sup>145</sup>. The bulk modulus of the orthorhombic, *Cmm2*, phase was calculated to be 62.9 GPa. The work was performed in a symmetric type diamond anvil cell at beamline 12.2.2 at the Advanced Light Source (ALS). A visual/plotted summary of all of the above data can be seen in Figures 43 through 45 and Table 8.

The materials that are easiest to directly compare are Bi<sub>2</sub>MoO<sub>6</sub> and Bi<sub>2</sub>WO<sub>6</sub>. The ionic radius of the Mo and W atoms are 83 pm and 80 pm respectively. A comparison of

atmospheric unit cell volumes from the initial phases and the high-pressure phases of these materials shows that the smaller ion has a greater impact. For  $\text{Bi}_2\text{MoO}_6$ , the larger ionic radius, the ratio of the high-pressure to low pressure unit cell volume is 96.4% whereas for  $\text{Bi}_2\text{WO}_6$  it is 94.1%.

A comparison of  $\text{La}_2\text{Mo}_4\text{O}_{15}$  and  $\text{Sm}_2\text{Mo}_4\text{O}_{15}$  yields some interesting information as well. The difference between the two materials is mainly the lanthanide group atom size that, for these two particular examples, produces two different stable structures at atmospheric conditions. These two structures then behave drastically different upon the application of pressure. The most extreme example of this difference in behavior is that  $\text{La}_2\text{Mo}_4\text{O}_{15}$  undergoes pressure-induced amorphization whereas  $\text{Sm}_2\text{Mo}_4\text{O}_{15}$  does not.

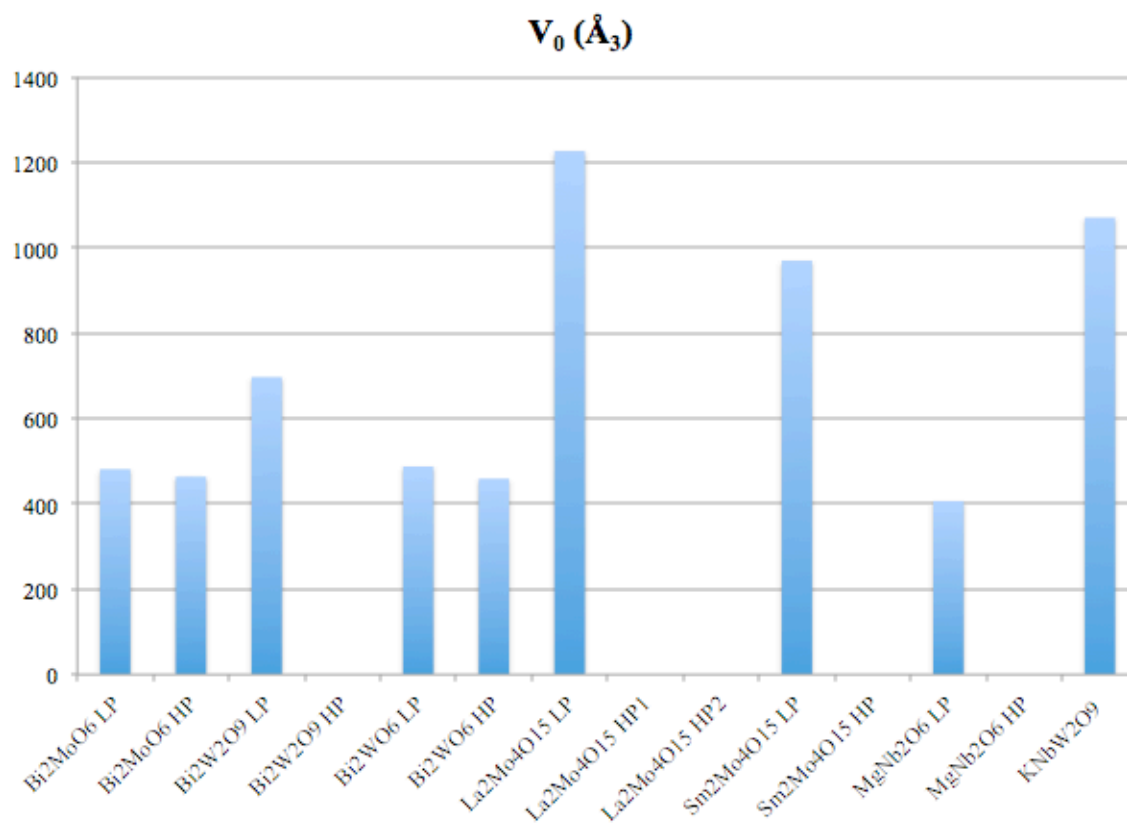


Figure 43. Material versus atmospheric unit cell volume. LP is for the low-pressure phases and HP is for the high-pressure phases. Not all material phases have calculable unit cell values at atmospheric pressure.

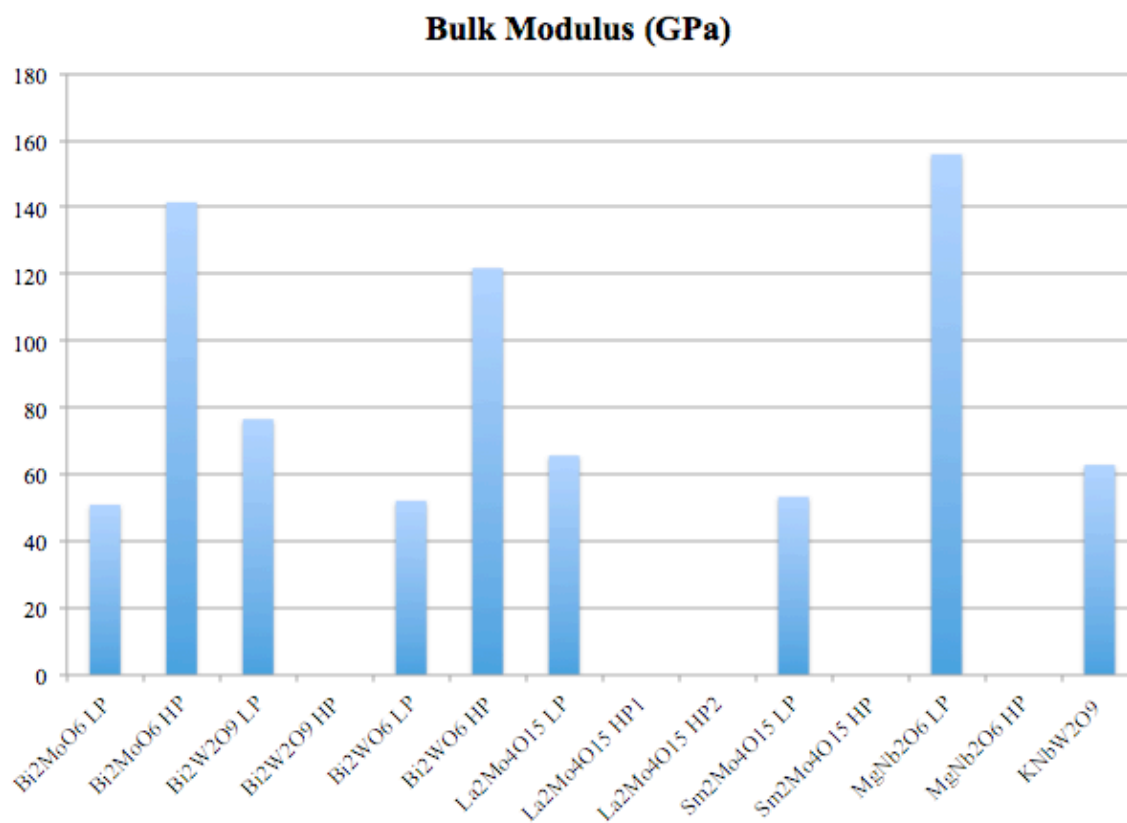


Figure 44. Material versus bulk modulus. LP is for the low-pressure phases and HP is for the high-pressure phases. Not all material phases have calculable bulk modulus.

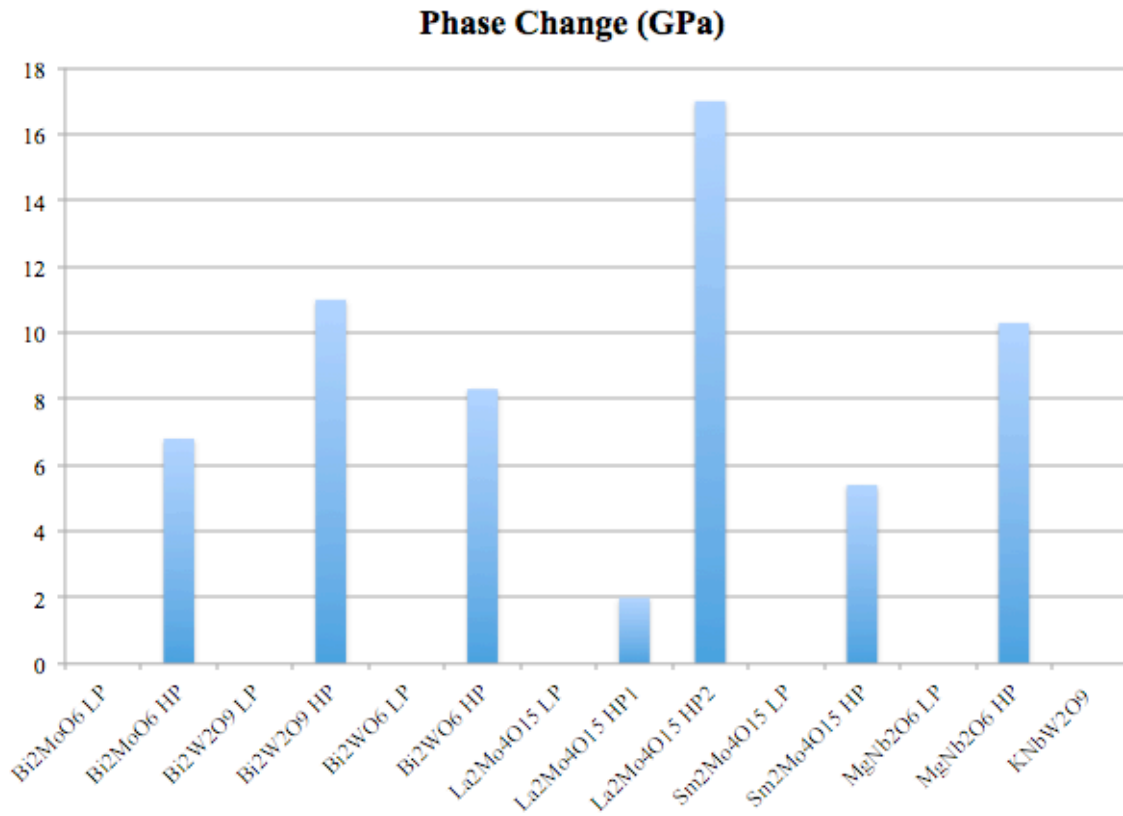


Figure 45. Material versus phase change pressure. The pressure is where the material is first observed.

Table 8: Summary of the data analysis.

Material	Phase Change (GPa)	Bulk Modulus (GPa)	$V_0$ ( $\text{\AA}^3$ )	Percent Volume Change	Ionic Radius (pm)
$\text{Bi}_2\text{MoO}_6$ LP	-	51	481.3	-	83
$\text{Bi}_2\text{MoO}_6$ HP	6.8	141.5	463.8	96.4%	83
$\text{Bi}_2\text{W}_2\text{O}_9$ LP	-	76.6	697.1	-	80
$\text{Bi}_2\text{W}_2\text{O}_9$ HP	11	TBD	TBD	TBD	80
$\text{Bi}_2\text{WO}_6$ LP	-	52.2	487.6	-	80
$\text{Bi}_2\text{WO}_6$ HP	Between 4.8 - 8.3	121.8	459	94.1%	80
$\text{La}_2\text{Mo}_4\text{O}_{15}$ LP	-	65.7	1226.8	-	103.2
$\text{La}_2\text{Mo}_4\text{O}_{15}$ HP1	2	TBD	TBD	TBD	103.2
$\text{La}_2\text{Mo}_4\text{O}_{15}$ HP2	17	Glass	Glass	-	103.2
$\text{Sm}_2\text{Mo}_4\text{O}_{15}$ LP	-	53.4	969.9	-	136
$\text{Sm}_2\text{Mo}_4\text{O}_{15}$ HP	5.4	TBD	TBD	TBD	136
$\text{MgNb}_2\text{O}_6$ LP	-	155.9	406.4	-	-
$\text{MgNb}_2\text{O}_6$ HP	10.3	TBD	TBD	TBD	-
$\text{KNbW}_2\text{O}_9$	-	62.9	1070.9	-	-

#### 4.2 Future Work

A lot of work remains to be performed on these groups of materials. The work presented here is essentially the tip of the iceberg for obtaining a better overall

understanding of the subtle phase changes that were observed. It is currently conceived that the following should be performed:

- A) The high-pressure structures for  $\text{Bi}_2\text{W}_2\text{O}_9$ ,  $\text{La}_2\text{Mo}_4\text{O}_{15}$  (intermediate phase),  $\text{Sm}_2\text{Mo}_4\text{O}_{15}$ , and  $\text{MgNb}_2\text{O}_6$  need to be defined. This can be completed by performing a more standard, non-Rietveld, analysis of the observed diffraction patterns and then subsequently indexing the Bragg peaks to several prototype structures.
- B) A broader range of similar materials needs to be analyzed in the same, or similar, fashion. Preliminary work has been started on  $\text{Ce}_2\text{Mo}_4\text{O}_{15}$ ,  $\text{Dy}_2\text{Mo}_4\text{O}_{15}$ , and  $\alpha\text{-BaTeMo}_2\text{O}_9$ . The inclusion of more data sets from analogue, or very similar, materials will allow for the direct comparison of attributes that contribute to the phase change pressure, pressure-induced amorphization, etc. During this analysis it may also be necessary to better pinpoint the exact phase change pressures of the materials reviewed above.
- C) To further understand the exact nature of atomic movement during the application of pressure it may be advantageous to perform neutron diffraction. Neutron diffraction can also provide information that could yield a better insight into the magnetic properties of the materials.
- D) Previous literature has reported negative thermal expansion properties in many of these materials. Performing high-pressure experiments while also varying the temperature could prove highly useful in developing a better understand of the phenomena of negative thermal expansion.

## APPENDIX

### IGOR USER PROCEDURES FOR DATA ANALYSIS

\*\*\*\*\*

#### Part I. F vs f Macro

\*\*\*\*\*

```
Macro FvsfVolume(WVol,WVolErr,WPress, WPressErr,Vnot,Wprefix,useErr)
  Variable Vnot = 493.039
  Variable DOCALCERR=1, DONTCALERR=2
  Variable useErr = DOCALCERR
  String WVol, WVolErr, WPress, WPressErr
  String Wprefix = "lf_bF_ Err_lf_ Err_bF_ wt_bf_"
  Prompt WVol,"Volume",popup,WaveList("*",";", "WIN:"+WinName(0,3))
  Prompt WVolErr,"Volume
Error",popup,WaveList("*",";", "WIN:"+WinName(0,3))
  Prompt WPress,"Pressure",popup,WaveList("*",";", "WIN:"+WinName(0,3))
  Prompt WPressErr,"Pressure
Error",popup,WaveList("*",";", "WIN:"+WinName(0,3))
  Prompt useErr, "Error:", popup, "Calculate Uncertainty;Do NOT Calculate
Uncertainty"
  Prompt Vnot, "Zero Pressure Volume in Å:"
  Prompt Wprefix, "Output prefixes:"
  String Wlitlef, WlitlefErr, WbigF, WbigFErr,WwtbigF
  Variable lenWave = 128

  if (CmpStr(Wprefix, "lf_bF_ Err_lf_ Err_bF_ wt_bf_") == 0) then
    Wlitlef = "lf_" + WVol
    WbigF = "bF_" + WVol
    if (useErr == DOCALCERR) then
      WlitlefErr = "Err_lf_" + WVol
      WbigFErr = "Err_bF_" + WVol
      WwtbigF = "wt_bF_" + WVol
    endif
  else
```

```

initIndex = 0
currentIndex = initIndex
WaveStats /Q $Wprefix
do
    if ((Wprefix[currentIndex] <> ",") and (currentIndex < V_npnts))
then
        currentIndex += 1
    endif
while ((Wprefix[currentIndex] <> ",") and (currentIndex < V_npnts))
if (currentIndex > initIndex) then
    Wlittlef = Wprefix[initIndex, currentIndex] + WVol
else
    Wlittlef = "lf_" + WVol
endif

initIndex = currentIndex + 2
currentIndex += initIndex
do
    if ((Wprefix[currentIndex] <> ",") and (currentIndex < V_npnts))
then
        currentIndex += 1
    endif
while ((Wprefix[currentIndex] <> ",") and (currentIndex < V_npnts))
if (currentIndex > initIndex) then
    WbigF = Wprefix[initIndex, currentIndex] + WVol
else
    WbigF = "bF_" + WVol
endif

if (useErr == DOCALCERR) then
    initIndex = currentIndex + 2
    currentIndex += initIndex
    do
        if ((Wprefix[currentIndex] <> ",") and (currentIndex <
V_npnts)) then
            currentIndex += 1
        endif
while ((Wprefix[currentIndex] <> ",") and (currentIndex <
V_npnts))
if (currentIndex > initIndex) then
    WlittlefErr = Wprefix[initIndex, currentIndex] + WVol
else
    WlittlefErr = "Err_lf_" + WVol

```

```

endif
|
initIndex = currentIndex + 2
currentIndex += initIndex
do
    if ((Wprefix[currentIndex] <> ",") and (currentIndex <
V_npnts)) then
        currentIndex += 1
    endif
    while ((Wprefix[currentIndex] <> ",") and (currentIndex <
V_npnts))
        if (currentIndex > initIndex) then
            WbigFErr = Wprefix[initIndex, currentIndex] + WVol
        else
            WbigFErr = "Err_bF_" + WVol
        endif
    endwhile
endif
endif
|
WaveStats /Q $WVol
    //|Make sure all waves are of the same length
lenWave = V_npnts
WaveStats /Q $WPress
if (lenWave != V_npnts) then
    Beep
    Abort "Pressure and Volume waves are of different lengths. NaN's are not
allowed"
endif
if (useErr == DOCALCERR) then
    WaveStats /Q $WVolErr
    if (lenWave != V_npnts) then
        Beep
        Abort "Pressure, Volume, and Volume Error waves are of different
lengths. NaN's are not allowed"
    endif
    WaveStats /Q $WPressErr
    if (lenWave != V_npnts) then
        Beep
        Abort "Pressure, Volume, and Error waves are of different lengths.
NaN's are not allowed"
    endif
endif
endif

```

```

Duplicate /O $WVol $Wlitlef
$Wlitlef = 0.5*((Vnot/$WVol)^(2/3)-1)
Duplicate /O $WVol $WbigF
$WbigF = $WPress/(3*$Wlitlef*(1+2*$Wlitlef)^2.5)
if (useErr == DOCALCERR) then
    Duplicate /O $WVol $WlitlefErr
    Duplicate /O $WVol $WbigFErr
    Duplicate /O $WVol $WwtbigF
    $WlitlefErr = (1/3)*(Vnot/$WVol)^(2/3)*($WVolErr/$WVol)
    $WbigFErr = $WbigF*sqrt(($WPressErr/$WPress)^2 +
(($WlitlefErr/$Wlitlef) + (5*$WlitlefErr/(1+2*$Wlitlef)))^2)
    $WwtbigF = 1/($WbigFErr)
endif

```

EndMacro

\*\*\*\*\*

## Part II. G vs g Macro

\*\*\*\*\*

```

Macro GvsgVolume(WVol,WVolErr,WPress, WPressErr,Vref,Wprefix,useErr)
    Variable Vref = 500
    Variable DOCALCERR=1, DONTCALERR=2
    Variable useErr = DOCALCERR
    String WVol, WVolErr, WPress, WPressErr
    String Wprefix = "lg_bG_Err_lg_Err_bG_wt_bG_"
    Prompt WVol,"Volume",popup,WaveList("*,",",", "WIN:"+WinName(0,3))
    Prompt WVolErr,"Volume
Error",popup,WaveList("*,",",", "WIN:"+WinName(0,3))
    Prompt WPress,"Pressure",popup,WaveList("*,",",", "WIN:"+WinName(0,3))
    Prompt WPressErr,"Pressure
Error",popup,WaveList("*,",",", "WIN:"+WinName(0,3))
    Prompt useErr, "Error:", popup, "Calculate Uncertainty;Do NOT Calculate
Uncertainty"
    Prompt Vref, "Arbitrary Reference Volume (Å cubed)"
    Prompt Wprefix, "Output prefixes:"
    String Wlitleg, WlitlegErr, WbigG, WbigGErr,WwtbigG
    Variable lenWave = 128

```

```

if (CmpStr(Wprefix, "lg_,bG_,Err_lg_,Err_bG_,wt_bG_") == 0) then
    Wlittleg = "lg_" + WVol
    WbigG = "bG_" + WVol
    if (useErr == DOCALCERR) then
        WlittlegErr = "Err_lg_" + WVol
        WbigGErr = "Err_bG_" + WVol
        WwtbigG = "wt_bG_" + WVol
    endif
else
    initIndex = 0
    currentIndex = initIndex
    WaveStats /Q $Wprefix
    do
        if ((Wprefix[currentIndex] <> ",") and (currentIndex < V_npnts))
then
            currentIndex += 1
        endif
        while ((Wprefix[currentIndex] <> ",") and (currentIndex < V_npnts))
        if (currentIndex > initIndex) then
            Wlittleg = Wprefix[initIndex, currentIndex] + WVol
        else
            Wlittleg = "lg_" + WVol
        endif
    |
        initIndex = currentIndex + 2
        currentIndex += initIndex
        do
            if ((Wprefix[currentIndex] <> ",") and (currentIndex < V_npnts))
then
                currentIndex += 1
            endif
            while ((Wprefix[currentIndex] <> ",") and (currentIndex < V_npnts))
            if (currentIndex > initIndex) then
                WbigG = Wprefix[initIndex, currentIndex] + WVol
            else
                WbigG = "bG_" + WVol
            endif
        |
            if (useErr == DOCALCERR) then
                initIndex = currentIndex + 2
                currentIndex += initIndex

```

```

do
    if ((Wprefix[currentIndex] <> ",") and (currentIndex <
V_npnts)) then
        currentIndex += 1
    endif
while ((Wprefix[currentIndex] <> ",") and (currentIndex <
V_npnts))
if (currentIndex > initIndex) then
    WlittlegErr = Wprefix[initIndex, currentIndex] + WVol
else
    WlittlegErr = "Err_lg_" + WVol
endif

|

initIndex = currentIndex + 2
currentIndex += initIndex
do
    if ((Wprefix[currentIndex] <> ",") and (currentIndex <
V_npnts)) then
        currentIndex += 1
    endif
while ((Wprefix[currentIndex] <> ",") and (currentIndex <
V_npnts))
if (currentIndex > initIndex) then
    WbigGErr = Wprefix[initIndex, currentIndex] + WVol
else
    WbigGErr = "Err_bG_" + WVol
endif
endif
endif

|

WaveStats /Q $WVol
//|Make sure all waves are of the same length
lenWave = V_npnts
WaveStats /Q $WPress
if (lenWave != V_npnts) then
    Beep
    Abort "Pressure and Volume waves are of different lengths. NaN's are not
allowed"
endif
if (useErr == DOCALCERR) then
    WaveStats /Q $WVolErr
    if (lenWave != V_npnts) then

```

```

        Beep
        Abort "Pressure, Volume, and Volume Error waves are of different
lengths. NaN's are not allowed"
    endif
    WaveStats /Q $WPressErr
    if (lenWave != V_npnts) then
        Beep
        Abort "Pressure, Volume, and Error waves are of different lengths.
NaN's are not allowed"
    endif
endif
|
Duplicate /O $WVol $Wlittleg
$Wlittleg = 0.5*((Vref/$WVol)^(2/3)-1)
Duplicate /O $WVol $WbigG
$WbigG = $WPress/(3*(1+2*$Wlittleg)^2.5)
if (useErr == DOCALCERR) then
    Duplicate /O $WVol $WlittlegErr
    Duplicate /O $WVol $WbigGErr
    Duplicate /O $WVol $WwtbigG
    $WlittlegErr = (1/3)*(Vref/$WVol)^(2/3)*($WVolErr/$WVol)
    $WbigGErr = $WbigG*sqrt(($WPressErr/$WPress)^2 +
(5*$WlittlegErr/(1+2*$Wlittleg))^2)
    $WwtbigG = 1/($WbigGErr)
endif

EndMacro

```

## REFERENCES

1. S. O. Alfrao and A. M.-d. I. Cruz, *Appl Cat A* **383**, 128 (2010).
2. A. M.-d. I. Cruz, S. O. Alfrao, L. M. Torres-Martinez and I. J. Ramirez, *J. Ceram. Proc. Res.* **9**, 490 (2008).
3. J. Tang and J. Ye, *J Mater Chem* **15**, 4246 (2005).
4. A. Feteira and D. C. Sinclair, *J. Am. Ceram. Soc.* **91**, 1338 (2008).
5. Y. Noguchi, K. Murata and M. Miyayama, *Applied Physics Letters* **89**, 242916 (2006).
6. H. Takeda, J. S. Han, M. Nishida, T. Shiosaki, T. Hoshina and T. Tsurumi, *Solid State Communications* **150**, 836 (2010).
7. B. Colon, S. M. Lopez, M. C. Hidalgo and J. A. Navio, *Chem Commun* **46**, 4809 (2010).
8. L. W. Zhang, Y. J. Wang, H. Y. Cheng, W. Q. Yao and Y. F. Zhu, *Adv Mater* **21**, 1286 (2009).
9. C. L. Li, K. Sun, L. Yu and Z. W. Fu, *Electrochim Acta* **55**, 6 (2009).
10. K. Zheng, Y. Zhou, L. Gu, X. Mo, G. R. Patzke and G. Chen, *Sens Actuat B* **148**, 240 (2010).
11. X. Zhao, T. Xu, W. Yao and Y. Zhu, *Thin Solid Films* **517**, 5813 (2009).
12. H. Y. Chang, T. Sivakumar, K. M. Ok and P. S. Halasyamani, *Inorg Chem* **47**, 8511 (2008).
13. L. Sebastian, S. Sumithra, J. Manjanna, A. M. Umarji and J. Gopalakrishnan, *Materials Science and Engineering B* **103**, 289-296 (2003).
14. T. Sugimoto, Y. Aoki, E. Niwa, T. Hashimoto and Y. Morito, *J. Ceram. Soc. Jpn.* **115**, 176 (2007).
15. B. I. Zadneprovski, V. A. Nefedov, E. V. Polyanski, E. G. Devistin, V. A. Kozlov and S. Y. Potashov, *Nuc. Inst. Meth. Phys. Res. A* **486**, 355 (2002).
16. A. A. Kaminski, S. N. Bagayev, K. Ueda, H. Nishioka, Y. Kubota and X. Chen, *Jpn J Appl Phys* **34**, L1461 (1995).

17. A. Mendez-Blas, M. Rico, V. Volkov, C. Cascales, C. Zaldo and C. Coya, J. Phys. Cond. Matt. **16**, 2139 (2004).
18. S. Neeraj, N. Kijima and A. K. Cheetham, Chem Phys Lett **387**, 2 (2004).
19. M. Rico, A. Mendez-Blas, V. Volkov, M. A. Monge, C. Cascales and C. Zaldo, J Opt Soc Am B **23**, 2066 (2006).
20. A. Mendez-Blas, M. Rico, V. Volkov, C. Zaldo and C. Cascales, Phys Rev B **75**, 174208 (2007).
21. A. I. Smirnov, L. E. Svistov, L. A. Prozorova, A. Zheludev, M. D. Lumsden and E. Ressouche, Phys Rev Lett **102**, 037202 (2009).
22. M. Kanzelmann, G. Lawes, A. B. Harris, G. Gasparovic, C. Broholm and A. P. Ramirez, Phys Rev Lett **98**, 267205 (2007).
23. J. Hanuza, M. Maczka, K. Hermanowicz, M. Andruszkiewicz, A. Pietraszko and W. Stek, J. Solid State Chem. **105**, 49 (1993).
24. L. H. Brixner, J. R. Barkley and J. Jeitschko, *Handbook on physics and chemistry of rare earth*. (North Holland, Amsterdam, 1979).
25. A. W. Sleight and L. H. Brixner, J. Solid State Chem. **7**, 172 (1973).
26. M. Cetinkol, A. P. Wilkinson and K. W. Chapman, Solid State Communications **148**, 511 (2008).
27. T. Varga, J. L. Moats, S. V. Ushakov and A. Navrotsky, J. Mater. Res. **22**, 2512 (2007).
28. T. Varga, A. P. Wilkinson, C. Lind, W. A. Bassett and C. S. Zha, J. Phys. Cond. Matt. **17**, 4271 (2005).
29. M. Naushad, Bull Mater Sci **31**, 957 (2008).
30. S. K. Sikka, J. Phys. Cond. Matt. **16**, S1033 (2004).
31. M. Maczka, P. T. C. Freire, C. Luz-Lima, W. Paraguassu, J. Hanuza and J. M. Filho, Journal of Physics: Condensed Matter **22**, 015901 (2010).
32. M. Maczka, W. Paraguassu, A. G. S. Filho, P. T. C. Freire, J. M. Filho and J. Hanuza, Phys Rev B **77**, 094137 (2008).

33. M. Maczka, W. Paraguassu, P. T. C. Freire, A. G. S. Filho, J. M. Filho and J. Hanuza, *Phys Rev B* **81**, 104301 (2010).
34. M. Maczka, W. Paraguassu, L. Macalik, P. T. C. Freire, J. Hanuza and J. M. Filho, *Journal of Physics: Condensed Matter* **23**, 045401 (2011).
35. M. Maczka, A. G. S. Filho, W. Paraguassu, P. T. C. Freire, J. M. Filho and J. Hanuza, *Progress in Materials Science* **51**, 1335 (2012).
36. C. E. Weir, E. R. Lippincott, A. V. Valkenburg and E. N. Bunting, *J. Res. Natl. Bur. Stand.* **63A**, 55 (1959).
37. R. A. Forman, G. J. Piermarini, J. D. Barnett and S. Block, *Science* **176**, 284-285 (1972).
38. J. E. Field, *The Properties of Diamond*. (Academic Press, New York, 1979).
39. M. Seal, *High-Temp High-Press* **16**, 573 (1984).
40. M. Seal, in *High-Pressure Research in Mineral Physics*, edited by M. Maghnani and Y. Syono (1987), pp. 35-40.
41. R. M. Hazen and R. T. Downs, in *Reviews in Mineralogy and Geochemistry*, edited by P. H. Ribbe (Mineralogical Society of America, 2001), Vol. 41.
42. G. J. Piermarini, S. Block and J. D. Barnett, *J. Appl. Phys.* **44**, 5377 (1973).
43. I. Fujishiro, G. J. Piermarini, S. Block and R. G. Munro, *High Pressure in Research and Industry: Proceedings of the 8th AIRAPT Conference* **2**, 608-611 (1981).
44. A. P. Jephcoat, H. K. Mao and P. M. Bell, *J. Geophys. Res.* **91**, 4677 (1986).
45. P. M. Bell and H. K. Mao, *Carnegie Inst Wash Yrbk* **78**, 665 (1979).
46. P. M. Bell and H. K. Mao, *Carnegie Inst Wash Yrbk* **80**, 404 (1981).
47. J. H. Eggert, K. A. Goettel and I. F. Silvera, *Phys Rev B* **40**, 5724 (1989).
48. J. H. Eggert, K. A. Goettel and I. F. Silvera, *Phys Rev B* **40**, 5733 (1989).
49. J. H. Eggert, F. Moshry, W. J. Evans, K. A. Goettel and I. F. Silvera, *Phys Rev B* **44**, 7202 (1991).
50. B. Chen, University of Missouri - Kansas City, 2001.
51. G. J. Piermarini and S. Block, *Rev. Sci. Inst.* **46**, 973 (1975).

52. J. D. Barnett, S. Block and G. J. Piermarini, *Rev. Sci. Inst.* **44**, 1 (1973).
53. H. K. Mao, P. M. Bell, J. W. Shaner and D. J. Steinberg, *J Appl Phys* **49**, 3276 (1978).
54. H. K. Mao and P. M. Bell, *J. Geophys. Res. B* **91**, 4673 (1986).
55. P. M. Bell, J. A. Xu and H. K. Mao, in *Shock Waves in Condensed Matter*, edited by Y. M. Gupta (Plenum Press, New York, 1986), pp. 125-130.
56. B. K. Godwal and R. Jeanloz, *Phys Rev B* **40**, 7501-7507 (1989).
57. L. C. Ming, M. H. Manghnani, J. Balogh, S. B. Qadri, E. F. Skelton and J. C. Jamieson, *Journal of Applied Physics* **54**, 4390-4397 (1983).
58. A. Jayaraman, *Reviews of Modern Physics* **55** (1), 65 (1983).
59. D. Shim, (Arizona State University, 2013).
60. B. D. Cullity, *Elements of X-ray Diffraction*, 2nd ed. (Addison-Wesley, Massachusetts, 1978).
61. H. M. Rietveld, *Journal of Applied Crystallography* **2** (2), 65 (1969).
62. H. M. Rietveld, *Acta Cryst.* **22**, 151 (1967).
63. L. Lutterotti, S. Matthies and H. R. Wenk, presented at the Proceeding of the Twelfth International Conference on Textures of Materials (ICOTOM-12), 1999 (unpublished).
64. C. V. Raman, *Nature* **121**, 501 (1928).
65. J. R. Ferraro, K. Nakamoto and C. W. Brown, *Introductory Raman Spectroscopy*, 2nd ed. (Academic Press, London, 2003).
66. M. S. Islam, S. Lazure, R. N. Vannier, G. Nowogrocki and G. Mairesse, *Journal of Materials Chemistry* **8**, 655-660 (1998).
67. X. Mao, W. Wang, X. Chen and Y. Lu, *Applied Physics Letters* **95**, 082901 (2009).
68. K. R. Kendall, C. Navas, J. K. Thomas and H.-C. z. Loye, *Chemistry of Materials* **8**, 642-649 (1996).
69. L. T. Sim, C. K. Lee and A. R. West, *Journal of Materials Chemistry* **12**, 17-19 (2002).

70. H. Li, C. Liu, K. Li and H. Wang, *Journal of Material Science* **43**, 7026-7034 (2008).
71. M. Long, W. Cai and H. Kisch, *Chemical Physics Letters* **461**, 102-105 (2008).
72. Y. Shimodaira, H. Kato, H. Kobayashi and A. Kudo, *Journal of Physical Chemistry B* **110**, 17790-17797 (2006).
73. P. Bégué, R. Enjalbert, J. Galy and A. Castro, *Solid State Sciences* **2**, 637-653 (2000).
74. D. J. Buttrey, T. Vogt and B. D. White, *Journal of Solid State Chemistry* **155**, 206-215 (2000).
75. A. F. V. D. Elzen and G. D. Rieck, *Acta Crystallographica* **B29**, 2436 (1973).
76. G. Sankar, M. A. Roberts, J. M. Thomas, G. U. Kulkarni, N. Rangavittal and C. N. R. Rao, *Journal of Solid State Chemistry* **119** (1), 210-215 (1995).
77. V. I. Voronkova, E. P. Kharitonova and O. G. Rudnitskaya, *Journal of Alloys and Compounds* **487**, 274-279 (2009).
78. G. A. Kourouklis, A. Jayaraman and L. G. V. Uitert, *Materials Letters* **5** (3), 116-119 (1987).
79. J. Liu, C. Gao, G. Zou and Y. Jin, *Physics Letters A* **218** (1-2), 94-98 (1996).
80. R. Delhez, T. H. D. Keijser, J. I. Langford, D. Louër, E. J. Mittemeijer and E. J. Sonneveld, *The Rietveld Method*. (Oxford University Press., New York, 1993).
81. R. G. Teller, J. F. Brazdil and R. K. Grasselli, *Acta Crystallographica* **C40**, 2001-2005 (1984).
82. F. Birch, *Journal of Geophysical Research* **83**, 1257 (1978).
83. R. Jeanloz, *Journal of Geophysical Research* **94** (B5), 5873-5886 (1989).
84. R. Jeanloz, *Geophysical Research Letters* **8** (12), 1219-1222 (1981).
85. J.-C. Champarnaud-Mesjard, B. Frit and A. Watanabe, *Journal of Materials Chemistry* **9**, 1319-1322 (1999).
86. Y. E. Kitaev, M. I. Aroyo and J. M. Perez-Mato, *Phys Rev B* **75**, 064110 (2007).
87. R. Machado, M. G. Stachiotti, R. L. Migoni and A. H. Tera, *Phys Rev B* **70**, 214112 (2004).

88. J. M. Perez-Mato, M. Aroyo, A. Garcia, P. Blaha, K. Schwarz, J. Schweifer and K. Parlinski, *Phys Rev B* **70**, 214111 (2004).
89. Y. Bando, A. Watanabe, Y. Sekikawa, M. Goto and S. Horiuchi, *Acta Cryst.* **A35**, 142-145 (1978).
90. A. M.-d. I. Cruz, S. O. Alfrao, L. M. Torres-Martinez and I. J. Ramirez, *J Ceram Proc Res* **9**, 490 (2008).
91. M. H. Hey and F. A. Bannister, *Mineralogical Magazine* **25**, 41 (1938).
92. H. W. Newkirk, P. Quadflieg, J. Liebertz and A. Kockel, *Ferroelectrics* **4**, 51 (1972).
93. S. Y. Stefanovich and Y. N. Venetsev, *Phys. Stat. Sol. (a)* **20**, K49 (1973).
94. I. G. Ismailzade and F. A. Mirishli, *Kristallografiya* **14**, 738 (1970).
95. V. K. Yanovskii, V. I. Voronkova, A. L. Alexandrovskii and V. A. D'yakov, *Dokl. Akad. Nauk SSSR* **222**, 94 (1975).
96. V. I. Utkin, Y. E. Roginskaya, V. I. Voronkova, V. K. Yanovskii, B. S. Galyamov and Y. N. Venetsev, *Phys. Stat. Sol. (a)* **59**, 75 (1980).
97. K. S. Knight, *Mineralogical Magazine* **56**, 399-409 (1992).
98. N. A. McDowell, K. S. Knight and P. Lightfoot, *Chem. Eur. J.* **12**, 1493-1499 (2006).
99. D. RAE, J. G. THOMPSON and R. L. WITHERS, *Acta Cryst.* **B47**, 870-881 (1991).
100. F. Dubois, F. Goutenoire, Y. Laligant, E. Suard and P. Lacorre, *Journal of Solid State Chemistry* **159**, 228 (2001).
101. W. Jeitschko, *Acta Crystallogr. B* **28**, 60 (1972).
102. J. S. O. Evans, T. A. Marry and A. W. Sleight, *Journal of Solid State Chemistry* **133**, 580 (1997).
103. J. S. Xue, M. R. Antonio and L. Soderholm, *Chem. Mater.* **7**, 333 (1995).
104. P. Lacorre, F. Goutenoire, O. Bohnke, R. Retoux and Y. Laligant, *Nature* **404**, 856 (2000).

105. F. Goutenoire, O. Isnard, R. Retoux and P. Lacorre, *Chem. Mater.* **12**, 2575 (2000).
106. F. Goutenoire, O. Isnard, E. Suard, O. Bohnke, Y. Laligant, R. Retoux and P. Lacorre, *J. Chem. Mater.* **11**, 119 (2001).
107. K. Aizu, A. Kumada, H. Yumoto and S. Ashida, *J. Phys. Soc. Japan* **27**, 511 (1969).
108. H. J. Borchardt and P. E. Bierstedt, *Appl. Phys. Lett.* **8**, 50 (1966).
109. G. Blasse and A. Bril, *J. Chem. Phys.* **45**, 2350 (1966).
110. J. Huang, J. Lories and P. Porcher, *Journal of Solid State Chemistry* **43**, 87 (1982).
111. M. Ouwerkerk, F. Kellendonk and G. Blasse, *J. Chem. Soc. Faraday Trans. 2* (78), 603 (1982).
112. H. Naruke and T. Yamase, *Acta Crystallogr. E* **57**, i106 (2001).
113. V. A. Efremov, N. N. Davydova, L. Z. Gokhman, A. A. Evdokimov and V. K. Trunov, *Russ. J. Inorg. Chem.* **33**, 1732 (1988).
114. G. D. Fallon and B. M. Gatehouse, *Journal of Solid State Chemistry* **44**, 156 (1982).
115. H. Naruke and T. Yamase, *Journal of Solid State Chemistry* **173**, 407 (2003).
116. A. P. Hammersley, S. O. Svensson, M. Hanfland, A. N. Fitch and D. Häuserman, *High Pressure Research* **14**, 235 (1996).
117. R. D. Shannon, *Acta Crystallogr. A* **32**, 751 (1976).
118. H. Naruke and T. Yamase, *Inorg. Chem.* **41**, 6514 (2002).
119. W. Paraguassu, M. Maczka, A. G. S. Filho, P. T. C. Freire, J. M. Filho and J. Hanuza, *Phys Rev B* **82**, 174110 (2010).
120. R. J. Speedy, *J. Phys.: Condens. Matter* **8**, 10907 (1996).
121. S. Pagola, R. E. Carbonio, J. A. Alonso and M. T. Fernandez-Diaz, *Journal of Solid State Chemistry* **134**, 76 (1997).
122. R. Norin, C. Arbin and B. Nölander, *Acta Chem. Scand.* **26**, 3389 (1972).

123. S. J. Butcher, University of Leeds, 1989.
124. S. L. Swartz and T. R. Shrout, *Mater. Res. Bull.* **17**, 1245 (1982).
125. K. Sreedhar and A. Mitra, *Mater. Res. Bull.* **32**, 1643 (1997).
126. D. Saha, A. Sen and H. S. Maiti, *J. Mater. Sci. Lett.* **13**, 723 (1994).
127. P. A. Joy and K. Sreedhar, *J. Amer. Ceram. Soc.* **80**, 770 (1997).
128. E. Goo, T. Yamamoto and K. Okazaki, *J. Amer. Ceram. Soc.* **69**, C-188 (1986).
129. C. Zaldo, M. J. Martin, C. Coya, K. Polgar, A. Peter and J. Paitz, *J. Phys. Condens. Matter* **7**, 2249 (1995).
130. H. C. Wang and W. A. Schulze, *J. Amer. Ceram. Soc.* **73**, 825 (1990).
131. M. J. Geselbracht, T. J. Richardson and A. M. Stacy, *Nature* **345**, 324 (1990).
132. K. N. Singh and P. K. Bajpai, *Physica B* **405**, 303 (2010).
133. T. S. Ercit, M. A. Wise and P. Cerny, *Amer. Mineralogist* **80**, 613 (1995).
134. M. Wegner, T. Armbruster and C. A. Geiger, *Amer. Mineralogist* **76**, 1897 (1991).
135. L. P. S. Santos, E. R. Camargo, M. T. Fabbro, E. Longo and E. R. Leite, *Ceramics International* **33**, 1205 (2007).
136. M. Maczka, J. Hanuza, S. Kojima, A. Majchrowski and J. H. v. d. Maas, *J. Raman Spec.* **32**, 287 (2001).
137. P. Labbe, *Key Eng. Mater.* **68**, 239 (1992).
138. V. K. Yanovskii, V. I. Voronkova and S. Y. Stefanovich, *Sov. Phys. Crystallogr.* **22**, 731 (1977).
139. G. N. Minaeva, V. I. Voronkova and V. K. Yanovskii, *Sov. Phys. Crystallogr.* **24**, 157 (1979).
140. I. P. Klimova, V. I. Voronkova, S. A. Okonenko, S. Y. Stefanovich and V. K. Yanovskii, *Sov. Phys. Crystallogr.* **25**, 67 (1980).
141. S. Y. Stefanovich, Z. G. Bazarova, I. S. Batueva and M. V. Mokhosoev, *Sov. Phys. Crystallogr.* **35**, 692 (1990).

142. Y. Tao, M. S. Hu and D. Feng, *Phys. Stat. Sol. A* **109**, 435 (1988).
143. I. P. Klimova, V. I. Voronkova and V. K. Yanovskii, *Izv. Akad. Nauk SSSR, Neorg. Mater.* **31**, 262 (1995).
144. P. R. Scott, J. A. Crow, M. Maczka and M. B. Kruger, *Journal of Solid State Chemistry* **194**, 15-18 (2012).
145. M. Maczka, A. G. S. Filho, P. T. C. Freire, J. M. Filho, S. Kojima and J. Hanuza, *J. Raman Spec.* **34**, 199 (2003).

## VITA

Paul Robert Scott Jr. was born on July 19, 1978, in St. Louis, Missouri. He was educated in public schools in the town of St. Clair, Missouri and graduated from St. Clair RXIII High School in 1996. He received several scholarships to the University of Missouri - Rolla, from which he graduated in 2001. His degree was a Bachelor of Science in Electrical Engineering.

After working his way to the level of senior engineer Mr. Scott began a master's program in Physics at the University of Missouri – Kansas City. He completed his master's work in 2007 and immediately began work toward a Ph.D. in Physics and Chemistry.

Mr. Scott is registered as an EIT in the state of Missouri and, as of 2013, holds the position of President at U2D Incorporated.